

**Effect of Lubricant Inertia on Textured Hydrodynamic
Journal Bearing using Mass Conserving Boundary
Conditions**

*A thesis
submitted in partial fulfilment of the
requirements for the degree of*

Doctor of Philosophy

by

Debajit Das



**Department of Mechanical Engineering
Indian Institute of Technology Guwahati**

June 2025



CERTIFICATE

This is to certify that the thesis entitled “**Effect of Lubricant Inertia on Textured Hydrodynamic Journal Bearing using Mass Conserving Boundary Conditions**”, submitted by **Debajit Das (196103106)**, a research scholar in the *Department of Mechanical Engineering, Indian Institute of Technology Guwahati*, for the award of the degree of **Doctor of Philosophy** is a record of an original work carried out by him under my supervision and guidance. The results embodied in this thesis has not been submitted to any other University or Institute for the award of any other degree or diploma.

(S K Kakoty)

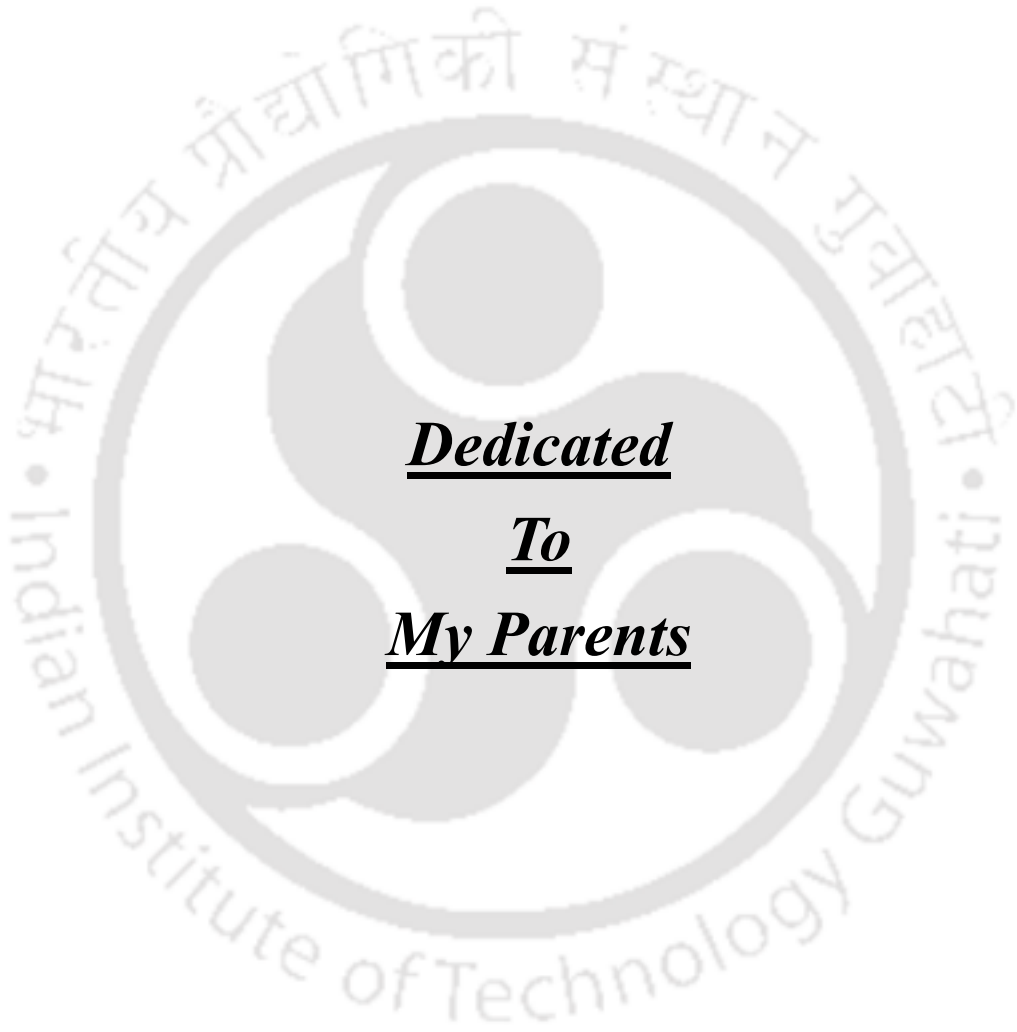
Professor

Department of Mechanical Engineering

Indian Institute of Technology Guwahati

June 2025





Dedicated
To
My Parents



Acknowledgement

Years of hard work and the countless help and support from the people around me has made it possible for me to complete the thesis work and it is my heartfelt desire to acknowledge their immense goodwill and valuable support.

First and foremost, I would like to express my heartfelt gratitude to my supervisor, Prof. Sashindra Kumar Kakoty, for his continuous support, guidance, and encouragement throughout the course of this research. His expert insights, patience, and constructive feedback played a pivotal role in shaping this work.

I also thank the current members of my doctoral committee, Prof. S. K. Dwivedy, Prof. K. Kalita, and Prof. D. Goswami, for their continuous guidance and valuable suggestions throughout the research work. I am equally grateful to the former committee members, Prof. S. Talukdar and Dr. Nelson Muthu, whose early insights and constructive feedback greatly contributed to shaping the direction of this thesis.

I am happy to acknowledge my debt to the present and past Heads of the Mechanical Engineering Department of IIT Guwahati for providing a conducive research environment and the necessary facilities that supported the completion of this thesis.

I would also like to extend my appreciation to my seniors, Dr. Syed N. Rasool, Dr. Pranay Kumar Sarkar, Dr. Kamal Basumatary and fellow research scholars, Shahrukh, Abhijit, Bipul, Kanak, Sumit, Nilkamal and Suranjit for the stimulating discussions, collaborative spirit, and shared experiences that enriched my academic journey. Your companionship and encouragement have been truly valuable.

Beyond the academic circle, I owe a special thanks to my dear friends Juan, Sasanka (Ph.D.), Faladrum (Ph.D.), Dhruva, Parthajit, Nitin, Pankaj, Pratim, Pranay (Ph.D.), Priti, Vandana, Moushumi (Ph.D.) and Nilakshi for their unwavering support, motivation, and understanding. Whether through kind words, light-hearted conversations, or simply being there, your presence helped me stay focused and resilient during challenging times.

Finally, I am deeply grateful to my family for their unconditional love, constant support, and belief in me. Without your strength and encouragement, this journey would not have been possible.

June 2025

Debajit Das



Abstract

Hydrodynamic journal bearings are widely used in engineering applications due to their self-acting nature and ability to support heavy loads. Enhancing the performance of such bearings, particularly in terms of load-carrying capacity, friction reduction, and flow efficiency, has been the focus of extensive research. Among various techniques, surface texturing has emerged as a promising method to improve tribological performance. However, the combined effects of surface texturing, lubricant inertia, and cavitation on journal bearing performance remain insufficiently explored.

This thesis presents a comprehensive study on the steady-state and stability behaviour of textured hydrodynamic journal bearings, incorporating both lubricant inertia effect and cavitation effects. A novel modified Reynolds equation is developed to incorporate these combined influences and is implemented under both Reynolds and Jakobsson – Floberg – Olsson (JFO) boundary conditions. Various texture geometries, *viz.*, spherical, cylindrical, and square (protrusions and dimples) are analyzed under different operating conditions, including variations in eccentricity ratio, dimple aspect ratio, texture area density and modified Reynolds number.

Results show that protrusion texturing significantly improves load-carrying capacity and frictional performance, particularly when lubricant inertia is included. Cylindrical and square protrusions provide the most favourable performance under Reynolds and JFO boundary conditions, respectively. In contrast, dimple texturing exhibits more complex behaviour, with performance trends highly sensitive to geometric parameters and operating conditions. The flow coefficient is enhanced by lubricant inertia with cylindrical protrusions offering the greatest improvements at high modified Reynolds numbers. However, when JFO boundary conditions are considered the flow coefficient generally reduces.

A nonlinear transient stability analysis reveals that protrusion-textured bearings demonstrate superior stability over dimpled and plain configurations. Stability is found to improve with increasing dimple aspect ratio and area density, while it deteriorates with larger non-dimensional clearance. Additionally, the presence of lubricant inertia contributes to improved stability under lightly loaded conditions.



Contents

Acknowledgement	i
Abstract	iii
Contents	v
List of Figures	ix
List of Tables	xiii
Nomenclature	xv
Abbreviations	xvii
Chapter 1	1
Introduction and Literature Review	1
1.1 Introduction	3
1.2 Literature Review	7
1.2.1 Hydrodynamic Journal Bearing	7
1.2.2 Inertia effects in Journal Bearings	12
1.2.3 Textured journal bearing	17
1.2.4 Cavitation in Hydrodynamic Bearings	25
1.3 Summary of Literature Review and Research Gap	27
1.4 Scope of the Present Work	29
1.4.1 Objectives	29
1.5 Organization of the Thesis	29
Chapter 2	31
Basic Equations, Boundary Conditions and Computational Methods	31
2.1 Introduction	33
2.2 Theory for Textured Journal Bearing with Lubricant Inertia Effect using Reynolds Boundary Conditions	33
2.2.1 Modified Reynolds Equation incorporating Fluid Inertia Effect	33

2.2.2 Modified Reynolds Equation for Textured Journal Bearing incorporating Fluid Inertia Effect	38
2.2.3 Numerical Solution	40
2.2.4 Performance Characteristics	42
2.2.5 Reynolds Boundary Conditions	46
2.2.6 Stability Analysis of Textured Journal Bearing	46
2.3 Theory for Textured Journal Bearing with Lubricant Inertia Effect using Mass-Conserving (JFO) Boundary Conditions	49
2.3.1 Governing Equation	49
2.3.2 Numerical Solution	51
2.3.3 Performance Characteristics	55
2.4 Fluid Film Thickness	55
2.5 Progressive Mesh Densification	56
2.6 Summary	57
Chapter 3	59
Steady State Analysis of Textured Journal Bearing considering Lubricant Inertia Effect and using Reynolds Boundary Conditions	59
3.1 Introduction	61
3.2 Methodology	61
3.3 Validation	61
3.4 Steady State Analysis of Textured Journal Bearing Considering Lubricant Inertia Effect	65
3.4.1 Load-carrying Capacity	66
3.4.2 Flow coefficient	70
3.4.3 Friction variable	73
3.5 Summary	77

Chapter 4	79
Steady State Analysis of Textured Journal Bearing Considering Lubricant Inertia Effect using Mass-Conserving (JFO) Boundary Conditions	79
4.1 Introduction	81
4.2 Methodology	81
4.3 Validation	82
4.4 Steady State Analysis of Textured Journal Bearing Considering Lubricant Inertia effect and cavitation	83
4.4.1 Load-carrying Capacity	84
4.4.2 Flow coefficient	90
4.4.3 Friction variable	95
4.5 Summary	101
Chapter 5	103
Stability Analysis of Textured Journal Bearing Considering Lubricant Inertia Effect	103
5.1 Introduction	105
5.2 Methodology	105
5.3 Stability Analysis of Textured Journal Bearing Considering Lubricant Inertia Effect	106
5.3.1 Effects of non-dimensional clearance (δ) on bearing stability	109
5.3.2 Effects of dimple aspect ratio (ψ) on bearing stability	111
5.3.3 Effects of dimple area density (S_p) on bearing stability	114
5.4 Summary	118
Chapter 6	119
Concluding Remarks	119
6.1 Introduction	121
6.2 Inferences	122
6.3 Conclusions	125

6.4 Scope for Future Works	127
References	129
List of Publications	143



List of Figures

Fig. 1.1. Schematic diagrams for (a) Axial, (b) Radial and (c) Conical Bearings	3
Fig. 1.2. Schematic diagrams for (a) Rolling, and (b) Sliding Contact Bearings	4
Fig. 2.1. Configuration of a journal bearing	33
Fig. 2.2. The fluid film	35
Fig. 2.3. Textured journal bearing with (a) protrusion; (b) dimple texture; (c) developed view of a hydrodynamic journal bearing with texturing; (d) micro texture inside an imaginary unit cell	38
Fig. 2.4. Flowchart of solution procedure using Reynolds boundary conditions	45
Fig. 2.5. Flowchart for Stability Analysis of Textured Journal Bearing	46
Fig. 2.6. Flowchart of the solution procedure using JFO boundary conditions	54
Fig. 3.1. Validation of present results for (a) textured and untextured bearing with Brizmer and Kligerman [67]; (b) inertia and without inertia case with Xu <i>et al.</i> [51] (c) textured journal bearing with experimental results of Yamada <i>et al.</i> [114]	63
Fig. 3.2. (a) Non-dimensional Load carrying capacity against eccentricity ratio for spherical texture; (b) Percentage change in non-dimensional load carrying capacity with inertia for spherical dimple texturing; (c) Percentage change in non-dimensional load carrying capacity with inertia for spherical protrusion texturing	66
Fig. 3.3. (a) Non-dimensional Load carrying capacity against eccentricity ratio for cylindrical texture; (b) Percentage change in non-dimensional load carrying capacity with inertia for cylindrical dimple texturing; (c) Percentage change in non-dimensional load carrying capacity with inertia for cylindrical protrusion texturing	67
Fig. 3.4. (a) Non-dimensional Load carrying capacity against eccentricity ratio for square texture; (b) Percentage change in non-dimensional load carrying capacity with inertia for square dimple texturing; (c) Percentage change in non-dimensional load carrying capacity with inertia for square protrusion texturing	68
Fig. 3.5. (a) Non-dimensional flow coefficient against eccentricity ratio for spherical texture; (b) Percentage change in non-dimensional flow coefficient with inertia for spherical dimple texturing; (c) Percentage change in non-dimensional flow coefficient with inertia for spherical protrusion texturing	70
Fig. 3.6. (a) Non-dimensional flow coefficient against eccentricity ratio for cylindrical texture; (b) Percentage change in non-dimensional flow coefficient with inertia for	

cylindrical dimple texturing; (c) Percentage change in non-dimensional flow coefficient with inertia for cylindrical protrusion texturing	71
Fig. 3.7. (a) Non-dimensional flow coefficient against eccentricity ratio for square texture; (b) Percentage change in non-dimensional flow coefficient with inertia for square dimple texturing; (c) Percentage change in non-dimensional flow coefficient with inertia for square protrusion texturing	73
Fig. 3.8. (a) Friction variable against eccentricity ratio for spherical texture; (b) Percentage change in friction variable with inertia for spherical dimple texturing; (c) Percentage change in friction variable with inertia for spherical protrusion texturing	74
Fig. 3.9. (a) Friction variable against eccentricity ratio for cylindrical texture; (b) Percentage change in friction variable with inertia for cylindrical dimple texturing; (c) Percentage change in friction variable with inertia for cylindrical protrusion texturing	75
Fig. 3.10. (a) Friction variable against eccentricity ratio for square texture; (b) Percentage change in friction variable with inertia for square dimple texturing; (c) Percentage change in friction variable with inertia for square protrusion texturing	76
Fig. 4.1. Comparison of current results with Elrod [5]	82
Fig. 4.2. Comparison of non-dimensional load capacity for Reynolds and JFO boundary conditions for (a) plain, (b) dimple and (c) protrusion textured bearing	84
Fig. 4.3. Variation of non-dimensional load-carrying capacity with eccentricity ratio for spherical, cylindrical and square texture with increasing inertia using JFO boundary conditions for (a) protrusion and (b) dimple texturing	86
Fig. 4.4. Non-dimensional load-carrying capacity Vs Dimple aspect ratio for spherical, cylindrical and square texture with increasing inertia and JFO boundary conditions for (a) protrusion and (b) dimple texturing for $\varepsilon = 0.5$	88
Fig. 4.5. Non-dimensional load-carrying capacity Vs Dimple area density for spherical, cylindrical and square texture with increasing inertia and JFO boundary conditions for (a) protrusion and (b) dimple texturing for $\varepsilon = 0.5$	89
Fig. 4.6. Comparison of non-dimensional flow coefficient for Reynolds and JFO boundary conditions for (a) plain, (b) spherical dimple and (c) spherical protrusion textured bearing	91
Fig. 4.7. Variation of non-dimensional flow coefficient with eccentricity ratio for spherical, cylindrical and square texture with increasing inertia and JFO boundary conditions for (a) protrusion and (b) dimple texturing	92

Fig. 4.8. Non-dimensional flow coefficient Vs Dimple aspect ratio for spherical, cylindrical and square texture with increasing inertia and JFO boundary conditions for (a) protrusion and (b) dimple texturing for $\varepsilon = 0.5$	93
Fig. 4.9. Non-dimensional flow coefficient Vs Dimple area density for spherical, cylindrical and square texture with increasing inertia and JFO boundary conditions for (a) protrusion and (b) dimple texturing for $\varepsilon = 0.5$	94
Fig. 4.10. Comparison of non-dimensional flow coefficient for Reynolds and JFO boundary conditions for (a) plain, (b) dimple and (c) protrusion textured bearing	96
Fig. 4.11. Variation of friction variable for spherical, cylindrical and square texture with increasing inertia and JFO boundary conditions for (a) protrusion and (b) dimple texturing	97
Fig. 4.12. Friction variable Vs Dimple aspect ratio for spherical, cylindrical and square texture with increasing inertia and JFO boundary conditions for (a) protrusion and (b) dimple texturing for $\varepsilon = 0.5$	99
Fig. 4.13. Friction variable Vs Dimple area density for spherical, cylindrical and square texture with increasing inertia and JFO boundary conditions for (a) protrusion and (b) dimple texturing for $\varepsilon = 0.5$	100
Fig. 5.1. Stable trajectory of journal centre for protrusion texturing for $\delta = 0.15, \psi = 0.06, s_p = 0.15, \bar{M} = 6.5$	107
Fig. 5.2. Horizontal and Vertical displacement of journal centre Vs. time for $\delta = 0.15, \psi = 0.06, s_p = 0.15, \bar{M} = 6.5$	107
Fig. 5.3. Critically stable trajectory of journal centre for protrusion texturing for $\delta = 0.15, \psi = 0.06, s_p = 0.15, \bar{M} = 7.9$	107
Fig. 5.4. Horizontal and Vertical displacement of journal centre Vs. time for $\delta = 0.15, \psi = 0.06, s_p = 0.15, \bar{M} = 7.9$	107
Fig. 5.5. Unstable trajectory of journal centre for protrusion texturing for $\delta = 0.15, \psi = 0.06, s_p = 0.15, \bar{M} = 12$	108
Fig. 5.6. Horizontal and Vertical displacement of journal centre Vs. time for $\delta = 0.15, \psi = 0.06, s_p = 0.15, \bar{M} = 12$	108
Fig. 5.7. FFT-spectrum of critical horizontal displacement for $\delta = 0.15, \psi = 0.06, s_p = 0.15, \bar{M} = 12$	108

Fig. 5.8. FFT-spectrum of critical vertical displacement for $\delta = 0.15, \psi = 0.06, s_p = 0.15, \bar{M} = 12$	108
Fig. 5.9. Stability Map for $L/D = 1.0, \delta = 0.10, \psi = 0.06, S_p = 0.15$	109
Fig. 5.10. Stability Map for $L/D = 1.0, \delta = 0.15, \psi = 0.06, S_p = 0.15$	110
Fig. 5.11. Stability Map for $L/D = 1.0, \delta = 0.25, \psi = 0.06, S_p = 0.15$	110
Fig. 5.12. Stability Map for $L/D = 1.0, \delta = 0.55, \psi = 0.06, S_p = 0.15$	111
Fig. 5.13. Stability Map for $L/D = 1.0, \psi = 0.02, \delta = 0.15, S_p = 0.15$	112
Fig. 5.14. Stability Map for $L/D = 1.0, \psi = 0.04, \delta = 0.15, S_p = 0.15$	112
Fig. 5.15. Stability Map for $L/D = 1.0, \psi = 0.06, \delta = 0.15, S_p = 0.15$	113
Fig. 5.16. Stability Map for $L/D = 1.0, \psi = 0.08, \delta = 0.15, S_p = 0.15$	114
Fig. 5.17. Stability Map for $L/D = 1.0, S_p = 0.10, \delta = 0.15, \psi = 0.06$	115
Fig. 5.18. Stability Map for $L/D = 1.0, S_p = 0.15, \delta = 0.15, \psi = 0.06$	116
Fig. 5.19. Stability Map for $L/D = 1.0, S_p = 0.25, \delta = 0.15, \psi = 0.06$	116
Fig. 5.20. Stability Map for $L/D = 1.0, S_p = 0.35, \delta = 0.15, \psi = 0.06$	117
Fig. 5.21. Stability Map for $L/D = 1.0, S_p = 0.50, \delta = 0.15, \psi = 0.06$	117

List of Tables

Table 1.1. Journal speed for different Re^* for lubricant A	5
Table 1.2. Journal speed for different Re^* for water	5
Table 3.1. Comparison of Sommerfeld number and Attitude angle for Plain Journal Bearings	62
Table 3.2. Comparison of results obtained by the PMD method and the FM method for Textured Journal bearing	62
Table 4.1. Operating and texturing parameters	83





Nomenclature

C	clearance, m
e	eccentricity, m
F_ε, F_ϕ	hydrodynamic forces, N
$\bar{F}_\varepsilon, \bar{F}_\phi$	non-dimensional hydrodynamic forces
\bar{g}	switch function
h	film thickness, m
\bar{h}	non-dimensional film thickness, h/C
h_0	film thickness for plain bearing, m
\bar{h}_0	Non-dimensional film thickness for plain bearing, h_0/C
h_p	local dimple depth, m
\bar{h}_p	non-dimensional local dimple depth, h_p/C
L	bearing length, m
M	mass of rotor, kg
\bar{M}	mass parameter, $MC\omega^2/W_0$
p	fluid film pressure, Pa
\bar{p}	non-dimensional pressure, $pC^2/\eta UR$
\bar{q}_z	non-dimensional flow coefficient
$Q_{\bar{z}}$	non-dimensional flow parameter in \bar{z} direction
Q_θ	non-dimensional flow parameter in θ direction

r_p	dimple base circle radius, m
$2r_1$	length of imaginary square cell, m
Re^*	modified Reynolds number, $(C/R)Re$
Re	Reynolds number
S_p	dimple aspect ratio, $\pi r_p^2/4r_1^2$
t	time, s
τ	Non-dimensional time, $\tau = \omega t$
u, v, w	velocity components in x, y and z direction
$\bar{u}, \bar{v}, \bar{w}$	non-dimensional velocity components: $\bar{u} = u/(R\omega)$, $\bar{v} = v/(C\omega)$, $\bar{w} = w/(R\omega)$
\bar{V}	velocity across film, $\partial\bar{h}/\partial\theta + (\partial\varepsilon/\partial\tau)\cos\theta + \varepsilon(\partial\phi/\partial\tau)\sin\theta$
\bar{W}	non-dimensional load-carrying capacity, $WC^2/\eta UR^2L$
x, y, z	Cartesian coordinates
x_1, z_1	local Cartesian coordinates
\bar{x}_1, \bar{z}_1	non-dimensional local Cartesian coordinates: $\bar{x}_1 = x_1/r_p$, $\bar{z}_1 = z_1/r_p$
θ, \bar{y}, \bar{z}	non-dimensional Cartesian coordinates: $x = R\theta$, $\bar{y} = y/C$, $\bar{z} = z/(L/2)$
α	texturing portion
β	bulk modulus, Pa
$\bar{\beta}$	non-dimensional bulk modulus, $\beta C^2/\eta UR$
ε	eccentricity ratio, e/C
δ	non-dimensional clearance, $C/2r_p$

ψ	non-dimensional dimple aspect ratio, $h_p/2r_p$
μ	friction variable
η	dynamic viscosity, Pa. s
θ_D	fractional film content, ρ/ρ_c
ρ	density, kg/m^3
ρ_c	density at cavitation pressure, kg/m^3
ω	angular velocity of the journal, rad/s
$\bar{\omega}$	whirl ratio
Ω	whirling speed of journal, rad/s

Abbreviations

<i>DXT</i>	dimple textured journal bearing
<i>FM</i>	fixed mesh
<i>JFO</i>	Jakobsson-Floberg-Olsson
<i>LCC</i>	load carrying capacity
<i>orf</i>	over-relaxation factor
<i>PLN</i>	plain journal bearing
<i>PMD</i>	progressive mesh densification
<i>PXT</i>	protrusion textured journal bearing
<i>TXT</i>	textured bearing



Chapter 1

Introduction and Literature Review

Contents

Introduction and Literature Review	1
1.1 Introduction	3
1.2 Literature Review	7
1.2.1 Hydrodynamic Journal Bearing	7
1.2.2 Inertia effects in Journal Bearings	12
1.2.3 Textured journal bearing	17
1.2.4 Cavitation in Hydrodynamic Bearings	25
1.3 Summary of Literature Review and Research Gap	27
1.4 Scope of the Present Work	29
1.4.1 Objectives	29
1.5 Organization of the Thesis	29



1.1 Introduction

Bearings are critical mechanical components used in various applications to facilitate smooth and efficient motion while supporting an applied load. Bearings enhance the performance, durability and energy efficiency of machinery by minimizing the frictional resistance. These functionalities make bearings indispensable in industries ranging from automotive and aerospace to manufacturing and robotics.

Bearings are classified into different types based on the applied load and the frictional characteristics. Based on the applied load, bearings are classified as (a) Axial bearings [Fig. 1.1(a)], (b) Radial bearings [Fig. 1.1(b)] and (c) Conical bearings [Fig. 1.1(c)].

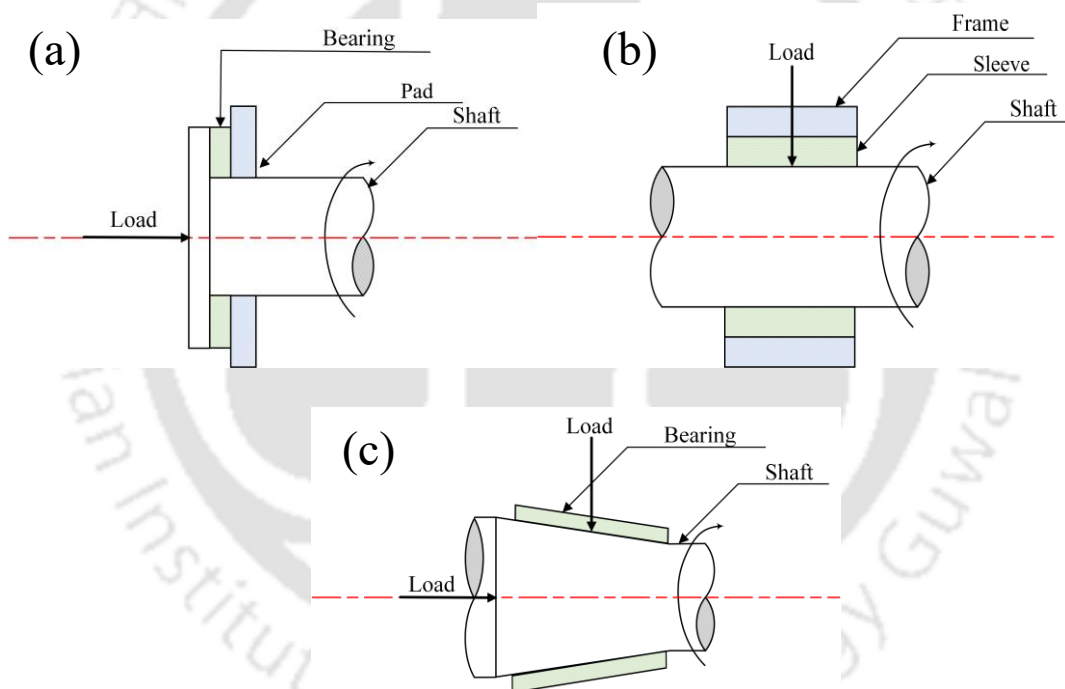


Fig. 1.1. Schematic diagrams for (a) Axial, (b) Radial and (c) Conical Bearings

Whereas, based on the type of friction between the shaft and the bearing, bearings are classified as (a) Rolling contact bearings [Fig. 1.2(a)] and (b) Sliding contact bearings [Fig. 1.2(b)]. Each type of bearing is designed to meet specific operational requirements, such as load capacity, speed, precision, and environmental conditions, ensuring optimal performance in diverse industrial applications.

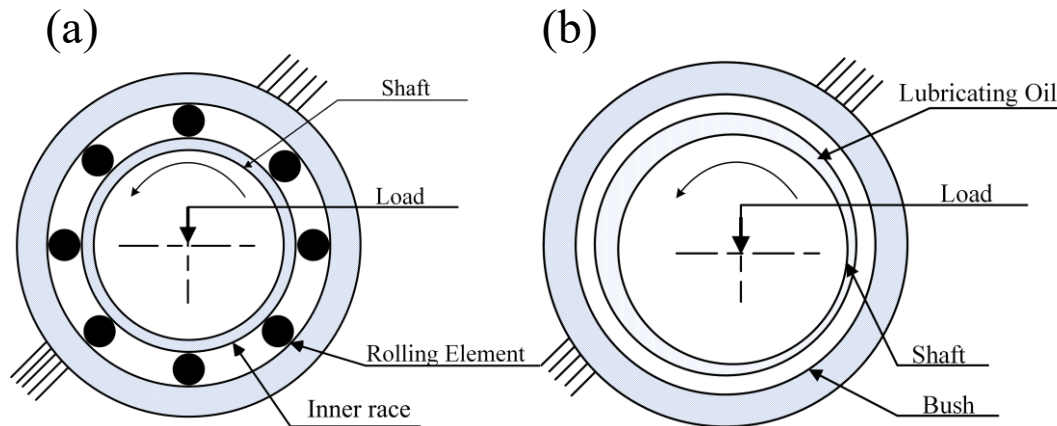


Fig. 1.2. Schematic diagrams for (a) Rolling, and (b) Sliding Contact Bearings

One of the most widely used bearings in industrial applications is the journal bearing. A journal bearing is a type of sliding contact bearing which takes load in the radial direction. One of the primary uses of journal bearings is in heavy machinery, such as turbines, compressors, pumps, and automotive engines where they support shafts under substantial radial loads. Additionally, journal bearings are used in industrial equipment like rolling mills, electric motors and generators, where they ensure stable operation and reduce vibrations. In marine and aerospace applications, journal bearings are favoured for their reliability and ability to function under extreme conditions.

Journal bearings work mainly on two principles – (a) Hydrodynamic or self-acting and (b) Hydrostatic or externally pressurized. In hydrodynamic journal bearings, the lubrication film is generated by the relative motion between the journal and the bearing. When the shaft starts to rotate, the lubricant enters the converging gap, creating a pressure build-up due to the wedge-shaped geometry. This pressure supports the applied load and separates the journal from the bearing surface, reducing friction and wear. Hydrodynamic bearings are commonly used in applications with high-speed shafts and consistent loads, such as turbines, compressors, and engines. In hydrostatic journal bearings, an external pump is used to supply pressurized lubricant into the bearing clearance, creating a lubricant film even when the shaft is stationary or operating at low speeds. The pressurized fluid supports the load and eliminates direct contact between the journal and the bearing surface. Hydrostatic bearings are often used in precision applications, such as

machine tools and high-load industrial equipment, where low friction, high accuracy, and reduced wear are critical.

Conventionally, the high viscosity fluids are used as lubricants for journal bearings. The inertia of the lubricant is, therefore, considered negligible in basic lubrication theory. In recent times, due to the use of low-viscosity lubricants and the high operating speed of machines, it has become essential to consider the effect of lubricant inertia while analyzing the performance characteristics of bearings. To better understand the impact of lubricant inertia, consider the following example [1]: a journal bearing with a diameter $D = 50$ mm and clearance to radius ratio $C/R = 0.001$. The modified Reynolds number (Re^*) of a bearing is given by, $Re^* = \left(\frac{C}{R}\right) \rho CR \omega / \eta$.

For a conventional lubricant having viscosity (η) = 0.02 Pa-S and density (ρ) = 850 kg/m³, the journal speeds for different Re^* are shown below

Table 1.1: Journal speed for different Re^* for lubricant A

Re^*	ω (rad/s)	N (RPM)
0.042	1570	15000
0.1	3765	35951
1.0	37648	359512
1.5	56470	548252

Now, considering water as a lubricant, we have the viscosity of water $\eta = 0.001$ Pa-S and density $\rho = 1000$ kg/m³; the journal speeds for different Re^* are shown below.

Table 1.2: Journal speed for different Re^* for water

Re^*	ω (rad/s)	N (RPM)
0.042	67.2	642
0.1	160	1528
1.0	1600	15278
1.5	2400	22611

From the above comparison, it is observed that for low-viscosity lubricants, the inertia effect is prominent at a speed of around 15000 RPM as the value of the modified Reynolds number is in the order of 1. However, for a lubricant with a viscosity of the order of 0.02 Pa-S, the lubricant inertia can be neglected at a speed of around 15000 RPM. Thus, it is observed that the lubricant inertia cannot be ignored, particularly for low-viscosity oil.

Over the last two decades, research on textured bearing surfaces has gained massive attention from the scientific community. Surface texturing in journal bearings refers to the deliberate introduction of micro- or nano-scale patterns, such as dimples, grooves, or protrusions, on the bearing surface.

Various microfabrication techniques [2] are employed to create textured patterns on bearing surfaces to enhance their performance. Techniques like laser surface texturing and chemical etching enable precise and controlled pattern formation, while abrasive jet machining/shot blasting provides high accuracy for intricate designs. Novel dressing methods, such as grinding and polishing, offer practical solutions for modifying surfaces, and mechanical imprinting is a cost-effective choice for mass production. Emerging technologies like additive manufacturing allow for complex geometries with minimal waste. The choice of technique depends on factors like material, pattern complexity, and application requirements, ensuring improved efficiency and durability in bearing operations [2]. Surface texturing in bearings aims to enhance the performance characteristics and mitigate issues such as Cavitation in journal bearings.

Cavitation in journal bearings occurs when the pressure of the lubricating oil drops below the vapour or cavitation pressure, forming vapour bubbles [3,4]. These bubbles can disrupt the oil film and cause damage to the bearing surfaces, resulting in increased friction, wear, and potential failure. Using the Reynolds boundary conditions and the Jakobsson-Floberg-Olsson (JFO) boundary conditions are two of the most commonly used techniques for treating the cavitation phenomenon in lubrication problems. The Reynolds boundary conditions can accurately predict where the film cavitates but do not account for the film reformation location [4]. This difficulty is overcome by employing the JFO boundary conditions, which ensure mass continuity. According to JFO cavitation theory there are two distinct regions of lubrication, one is the full film region and other is

the cavitated region [5]. In the full film region, the gap between the moving and the stationary surfaces is completely filled by the lubricating liquid and here the original Reynolds equation applies. Pressure variation occurs in this region with cavitation pressure being the minimum possible pressure. In the cavitated region, the bearing gap is filled partly by liquid and partly by gas presumably in the form of multiple liquid striations. Because of the presence of gas, the pressure is considered to be constant in the entire cavitation zone.

One particular issue with hydrodynamic journal bearings is the problem of instability due to oil whirl and oil whip. Oil whirl is characterized by an unusual vibration frequency, typically 40-48% of the shaft's rotational speed [6]. On the other hand, when the shaft rotates at roughly twice the speed corresponding to the first critical speed of the system, oil whirl occurs at approximately half the rotational speed, bringing it near the system's natural frequency. This resonance-like condition is referred to as oil whip (or resonant whip), where the sub-synchronous vibration becomes self-sustained and does not subside with time. If left unchecked, this can lead to severe vibrations and potential system failure. The onset of oil whirl depends on various factors such as bearing clearance, journal speed and lubricant properties. It is crucial to determine the critical speed at which the bearing becomes unstable to avoid running the system beyond this point. Thus, the instability phenomenon can be avoided and the lifespan of the bearing is extended, ensuring more reliable and stable operation in high-speed systems. There are primarily two approaches to investigate the stability characteristics of rotor-bearing systems: Linear perturbation method and Non-linear time transient analysis.

1.2 Literature Review

1.2.1 Hydrodynamic Journal Bearing

The study of lubrication has been a focus of research and innovation for several centuries. One of the most significant works in the field of hydrodynamic lubrication was Tower's [7] experiment in 1883. In the Tower's experiment, the variation in performance parameters were demonstrated whilst the bearing was subjected to a lubricated and immersed conditions. He found that bearings under loaded condition developed peak pressure which was several times higher than the mean pressure calculated based on projected area.

Reynolds [8], in 1886, made a review of the detailed experimental results of Tower and deduced that the lubrication of bearing was dependent on the hydrodynamic action. He was also able to model the phenomenon mathematically, giving the generalised differential equation for bearing studies. Later, the differential equations, governing the operation, became a broad topic of research as tribological aspects were studied in depth by several researchers.

Kingsbury [9] described an electrical analogy method for the solution of Reynolds equation. His experimental analysis was based on the similarity of the Reynolds equation with the equation for the flow of electric current through an electrolyte bath. From his analysis, he proposed some leakage factors, with the help of which it was possible to estimate the load-carrying capacity and coefficient of friction for finite journal bearings.

Muskat et al. [10] studied the lubrication of plane slider bearings considering finite width. They numerically applied the Reynolds theory for a wide range of operating conditions. From their analysis, they were able to publish complete curves for a wide range of operating conditions of plane sliders.

Christopherson [11] proposed a new method known as the ‘relaxation’ method for the solution of Reynolds equation. The method was validated for variety of practical situations faced by fluid film lubrication system. Christopherson also suggested that, when a numerical method is used to solve the Reynolds equation, the negative pressures at any grid points may be considered as zero and then further iterations can be carried out. This way the Swift-Stieber [12,13] boundary conditions for journal bearings are satisfied.

Dubois and Ocvirk [14] and Ocvirk [15] presented analytical solutions for short bearing approximation. Short bearing approximation may be applied to when the length to diameter ratio is less than 1. They were able to validate their analytical results with the experimental results and hence the short bearing approximation was found to be in reasonable agreement with natural phenomena.

Raimondi and Boyd [16–18] used the method proposed by Christopherson and performed extensive analysis on journal bearings, providing numerical solutions that considered a wide range of bearing geometries, published as a comprehensive three-part article series. Their findings remain a benchmark for plain journal bearings and are widely regarded as standard reference results in the field.

Pinkus and Bupara [19] published a comprehensive analysis for misaligned journal bearing with grooves and presented results for the case of $L/D=1$. They concluded that the misalignment effect can produce finite load carrying, oil flow and friction even when the minimum fluid film thickness approaches zero. Further, for a single axial groove bearing, an orientation of journal misalignment normal to the groove was found to be more advantageous.

El-Gamal [20] analysed the steady-state performance of a wedge-shaped hydrodynamic journal bearing. Here a Wedge-shaped hydrodynamic bearing is proposed. The flow of Lubricant in the bearing is considered laminar and incompressible and the lubricant to be Iso-Viscous. The pressure inside the bearing is governed by the Reynolds like equation for which an oblique system of coordinates is used. An exact solution for the pressure is presented and for small values of the bearing wedge angle a valid perturbed solution is also given. From the results it is concluded that the wedge-shaped bearing of small wedge angle is better to cylindrical bearing having the same side length. It is also concluded that a wedge-shaped bearing configuration is best recommended for long bearings rather than for short bearings.

Chatterton et al. [21] conducted the experimental investigation on the influence of the applied static load and rotational speed on the behaviour of a 160 mm diameter cylindrical journal bearing with two axial grooves. In the experiment the rotational speed ranged from 66 rpm to 1440 rpm, and the static load varied from 0 kN to 350 kN in the vertical direction. They measured the profiles of the pressure and the oil-film thickness during the shaft rotation by one proximity probe and one pressure probe installed in the rotating shaft. And they have presented and discussed the measurements of shaft centre position, dynamic coefficients, hydrodynamic pressure and temperature distributions on the bearing, film thickness, and bearing deformation under several operating conditions.

Zhang et al. [22] provided an efficient method for determining the stiffness coefficients of hydrodynamic plain journal bearings lubricated by water. The relationships between the stiffness coefficients and the load for bearings with different relative clearances, different length to diameter ratios and different rotational speeds were obtained. The authors also studied bearings with different diameters to find how

load carrying capacity and stiffness coefficients change with diameter. Finally, a method is provided for determining the stiffness coefficients of such bearings.

Cui et al. [23] attempted to optimize the performance of plain journal bearings with partial wall slip. Their analysis showed that the slip zone should be located at the convergent region of the film for optimum performance and the optimal range of slip zone in the case of high eccentricity ratio is quite restricted.

Chowdhury et al. [24] determined the friction coefficient of plain journal bearings using SAE 5W-30 as lubricant. They observed reduced friction coefficient under SAE 5W-30 lubrication.

Milčić et al. [25] used artificial neural network to predict the friction coefficient and bearing temperature with respect to speed and radial load of hydrodynamic journal bearings. Using experimental data to train their network, they concluded that a well-trained network can be effectively used to predict friction coefficients depending on the radial load and speed. A multi-objective design optimization of hydrodynamic journal bearings using genetic algorithm and sequential quadratic programming was conducted by Shaltout and Hegazi [26]. They suggested several optimum designs providing a general framework for designers to optimally design hydrodynamic journal bearings without prior knowledge of the relative importance of objective functions.

Li et al. [27] performed numerical analysis to determine the stability boundary for orifice compensated hole-entry hybrid journal bearings of finite length considering the nonlinear forces and the initial position of the shaft. From the analysis they found that the nonlinear stability of the hybrid journal bearings is not only affected by the rotating speed but also by the initial position of shaft centre. Under the linear assumption, the system can always recover to the stable state if the rotating speed is smaller than the critical speed. However, under the nonlinear conditions, there exists the stability boundary and the transitional region of the rotating speed. The shaft with the initial point located in the boundary can lead to a stable system. During the transitional region, when the shaft rotating speed increases to the threshold speed, the stability boundary shrinks gradually to the equilibrium point. To maximize the stability capacity of the hybrid journal bearings, the maximum rotating speed should be smaller than the transitional speed instead of the critical speed to gain a relatively larger stability boundary.

Navthar and Halegowda [28] conducted experimental analysis of journal bearing to check the stability by operating at a certain speed and load condition. They observed that bearing operating at a speed of 800 rpm and 150N load remains stable up to a speed of 1666rpm.

Raghunandana and Majumdar [29] carried out a non-linear time transient analysis for hydrodynamic journal bearings considering the Non-Newtonian behaviour of lubricants. They concluded that Non-Newtonian lubricants with higher power law index ($n < 1$) improve the stability in general. However, bearing with a Newtonian lubricant ($n = 1$) has the best stability. Further, heavily loaded bearings (eccentricity ratio > 0.6) and short bearings ($L/D < 1.0$) gave higher stability, while using Newtonian lubricant.

Das et al. [30] studied the dynamic characteristics of hydrodynamic journal bearings lubricated with micropolar fluids. Using first order perturbation method, the authors calculated the critical mass parameter and the whirl ratio for the bearing. The results showed that micropolar fluid exhibits better stability in comparison with Newtonian fluid. The whirl ratio for micropolar regime was found to be lying between 0.49 and 0.58.

Papadopoulos et al. [31] analysed the stability of rotor-journal bearing system by identifying and providing new clearance to the bearing system. They modelled a rotor with 4 DOF using finite element method and the dynamic coefficients of the bearings were obtained by solving the Reynolds equation. From their results, they concluded that the method described in the paper was a non-destructive method and only the measurement of eccentricities were required in a real machine system to apply the aforementioned method to identification of a new operational clearance which has appeared due to wear effects, thus avoiding the costly disassembly and assembly of the machine in order to measure the wear.

Jang and Yoon [32] presented an analytical method to investigate the stability of a hydrodynamic journal bearing with rotating herringbone grooves. The dynamic coefficients of the hydrodynamic journal bearing were calculated using the perturbation method. The research showed that the instability of a hydrodynamic journal bearing with rotating herringbone grooves increases with increasing eccentricity and with decreasing groove number which play the major roles in increasing the average and variation of

stiffness coefficients. They also found that a high rotational speed is another source of instability by increasing the stiffness coefficients without changing the damping coefficients.

Dinakaran and Ramesh [33] investigated the dynamic characteristics and stability behaviour of journal bearings lubricated with couple stress fluids. Their analysis focused on how variations in the eccentricity ratio and length-to-diameter ratio (L/D) affect the stiffness and damping coefficients of the bearing. Using a modified Reynolds equation and finite difference method, they computed the dynamic coefficients for a range of operating conditions. A notable finding from their study was that beyond an eccentricity ratio of 0.7, the dynamic response of the system changes significantly, with increased load-carrying capacity, potentially leading to instability. Their work demonstrated that small disturbances at higher eccentricity ratios could trigger amplified oscillatory behaviour, underlining the importance of dynamic coefficient evaluation for predicting stability margins.

1.2.2 Inertia effects in Journal Bearings

Historically, most researchers studying bearings have concluded that inertia forces have a minimal effect on typical bearings operating in the laminar regime at small to moderately large Reynolds numbers. This assumption was also fundamental in deriving the Reynolds equation from the Navier-Stokes and continuity equations. However, with the increasing speeds of modern machinery and the use of unconventional lubricants such as water and liquid metals, the study of fluid inertia effects has gained significant importance.

Constantinescu [34], in 1970, developed a method to determine the motion in a fluid film including inertia forces. The method which was developed for infinitely long bearings can be used for both laminar and turbulent flows, as well as for incompressible and compressible lubricants. From the obtained results the author concluded that for the steady films, convective inertia forces lead basically to Bernoulli effects, while for unsteady films inertia forces may influence both damping and stiffness characteristics of the bearing. Further, he mentioned that when Bernoulli effects are important, similar effects may occur in the inlet region of the film.

Reinhardt and Lund [35] presented a study on the effect of fluid film inertia on the dynamic properties of a journal bearing. They used first order linear perturbation method in their analysis. From their analysis and results, they were able to confirm that the contribution from the inertial film forces to the load carrying capacity and the dynamic reaction forces of journal bearing was quite limited. The corrections to the regular amplitude and velocity coefficients amount at most to a few per cent, which was less than the tolerance error and thus could be neglected. However, the correction to the acceleration coefficients, may act as a virtual mass and for certain bearings, the effect may be equivalent to the increase of the bearing mass by a factor of 5 to 10. Further, the authors predicted that for sufficiently high-speed motion of the journal, the inertia effect may become more prominent.

Constantinescu and Galetuse [36] proposed a numerical method along with appropriate boundary conditions for solving lubrication equation when inertial effects are considered. The authors proposed an iterative method which could be adapted to any existing program for calculating the operating characteristics of any type of bearings. Further, it was found that a first iteration is usually sufficient to provide satisfactory results in terms of main operating characteristics, so that it can be used even for large clearance ratios and Reynolds numbers.

Malvano and Vatta [37] studied the influence of fluid inertia in the case of a slider bearing considering laminar flow of lubricant. The authors proposed a new method by simplifying the assumptions. From their analysis, it was observed that the inertial terms became significant with the increase in the modified Reynolds number. Further, the presence of inertial terms increased the load-carrying capacity and frictional force.

Chen and Chen [38] studied the influence of lubricant inertia on the performance characteristics of finite journal bearings. Their study revealed that the influence of inertia forces was small in the case of load-carrying capacity however, inertia forces in the bearing resulted in significant increase in the side flow rate.

Nataraj et al. [39] presented a derivation of the correction term to be added to account for the effect of inertia in the case of a short journal bearing. They used first order perturbation method in their analysis to obtain the governing equation for pressure

correction. The first order terms of corrected stiffness, damping, and inertia coefficients were also reported as function of the equilibrium position of the journal.

Kakoty and Majumdar [40,41] conducted two analyses to study the effect of fluid inertia on stability of flexibly supported oil journal bearings; firstly, by using linear perturbation method and secondly using transient analysis method. A modified Reynolds equation was obtained in order to accommodate the inertia effect of the fluid, which is neglected in the generalised Reynolds equation and Reynolds boundary condition was applied during the solution of the equation. They concluded that although the steady state characteristics of the bearing aren't much affected due to inertia, however its effects cannot be ignored in the case of flexibly supported journal bearings. Thus, considering fluid inertia in the study of journal bearings ensures accurate prediction in estimating the optimum support parameters. The same research group [42,43] analysed the effects of fluid inertia in case of rigidly supported bearings as well, using linear perturbation method and transient analysis method, and they were able to verify the importance of considering the effect of the fluid inertia in stability analysis of bearings.

Nassab [44] studied the effect of inertia of the lubricant on the thermohydrodynamic characteristics of journal bearings. They used Computational Fluid Dynamics method to solve the governing equation for a finite journal bearing operating under incompressible laminar flow and steady conditions. They also considered the cavitation effects using an appropriate three-dimensional cavitation model. From their investigation, they found that the inertia effect increases the load capacity and the attitude angle of the bearing. Further, they noticed that at moderate value of Reynolds number (in the order of 10), the fluid inertia is found to have substantial effect on thermohydrodynamic characteristics of journal bearing if the bearing runs under low load, high speed and large clearance conditions.

Javorova et al. [45] studied the effects of fluid inertia on the stability of finite journal bearings and for bearings with elastic layer on the shaft for a flow in the laminar regime. The generalized Reynolds equation is obtained by averaged acceleration method. Stability of the bearing was analysed by using modified stability criteria by Hurwitz and Ljapunov. It was found that consideration of the bearing surface deformation and lubricant's inertia forces are conducive to the stability state of the system. This

phenomenon can be explained by the changes in the hydrodynamic pressure distribution and the corresponding changes in the Sommerfeld number, resulting from the combined influence of surface deformation and fluid inertia.

Lin et al. [46] studied the combined effects of convective fluid inertial forces and non-Newtonian couple stresses on the squeeze film characteristics for a long partial journal bearing. For this purpose, they derived a closed form solution for the behaviour of the squeeze film for long partial journal-bearing system. From their study, they found that the combined effects of convective inertial forces and non-Newtonian couple stresses provide an increase in the film pressure, the load-carrying capacity, and the approaching time of the squeeze film bearing.

Dousti et al. [47] developed an extended Reynolds equation to include both turbulent and inertia effect for journal bearings. The newly developed Reynolds equation is applicable to bearings with high reduced Reynolds number, which occurs when rotors run at high rotational speed or low viscosity lubricant is used. In their study, the authors identified two types of temporal inertia terms for the first time: primary and secondary, in both laminar and turbulent regimes. It is shown that, as prognosticated analytically, the secondary inertia effects contribute largely (up to 30%) to the magnitude of the directly added mass coefficient in the direction of the applied load. Further, they concluded that the turbulence effect is in general more pronounced on static characteristics, by increasing the load capacity similar to the convective inertia effect.

Javorova and Alexandrov [48] studied the effects of lubricant inertia and deformability of the bearing elastic layer on the performance of a plane journal bearing. To take into account the inertia effects, the modified Reynolds equation for dynamic loading governing the film pressure is derived by averaged acceleration method using the Navier-Stokes equations. The authors concluded that there isn't much significant effect of fluid inertia, however the maximum value of pressure developed increases due to inertia and so is the Sommerfeld number, whereas the values of friction factor decrease with inertia. The load carrying capacity and pressure developed inside the bearing increase with the decrease in deformability of bearing surface. Javorova [49] also published a review article on the influence of lubricant inertia on hydrodynamic lubrication.

Ghosh et al. [50] did steady state analysis on performance characteristic of journal bearings considering the combined effect of bearing liner surface deformation and fluid inertia. The modified averaged Reynolds equation was solved by using finite different scheme and Gauss-Siedel method with successive over relaxation scheme for calculation of pressure and Simpson's 1/3rd rule for numerical integration to calculate the load carrying capacity. The study revealed that for eccentricity ratios greater than 0.7, the flexibility of the bearing liner leads to a significant reduction in load-carrying capacity, whereas this effect is negligible for lower eccentricity values. The distortion effects become more prominent with the increase in L/D ratio resulting in decreased load carrying capacity. With the increase in Reynolds number, the load carrying capacity increases but drops when the bearing liner is made flexible.

Xu et al. [51] investigated the effects of turbulence, fluid inertia, and misalignment on the static and dynamic performance, as well as the stability, of high-speed water-lubricated hydrodynamic journal bearings. Their results indicate that turbulence significantly enhances load-carrying capacity, power consumption, stiffness and damping coefficients, and overall bearing stability. In contrast, fluid inertia primarily contributes to an increase in the volumetric flow rate. Misalignment was also found to improve load capacity, stiffness and damping characteristics, and system stability. Notably, under conditions of high rotational speed and moderate eccentricity ratios, the influence of inertia on load capacity, stiffness, and stability becomes substantial and should not be neglected.

Ozen and Azeloglu [52] proposed a new inertia correction method for one-dimensional lubrication problems using a non-uniform finite difference method based on the Reynolds equation. They suggested that their proposed method yielded identical results to full Navier-Stokes model with extremely fast calculation.

Chen et al. [53] studied the influence of oil-film inertia, journal static eccentricity, and base motions on transient responses and bifurcation behaviour of a rotor - squeeze film damper (SFD) support system. The results suggested that at a high eccentricity ratio, the oil-film inertia enhances the reaction forces.

Kushare and Sharma [54] carried out a non-linear transient analysis for a worn hybrid journal bearing with two-lobe symmetric hole. They concluded that the stability

of the bearing system may be improved by the proper selection of bearing geometrical parameters. An analytical method was developed by Fan et al. [55] to estimate the stability of synchronous non-linear vibration in a vertical rotating shaft system with a journal bearing.

1.2.3 Textured journal bearing

Now-a-days textured surfaces play a vital role in improving the tribological performance between two mating pairs in hydrodynamic lubrication. In 1960s, Hamilton et al. [56] indicated that micro-irregularities are able to generate additional hydrodynamic pressure which increases the overall load carrying capacity of the surfaces. This theory has been well accepted, and micro-hydrodynamic effect is regarded as the most dominant effect of surface texture for high-speed and low-load applications [57].

Jeng [58] did an experimental verification of the effect of surface roughness on lubrication theories. To study the effects of roughness height and orientation on friction, machined samples mounted longitudinally and transversely were tested. From their experimental results, they concluded that lower surface height yielded lower friction and transverse roughness had lower friction than longitudinal roughness. Also, the surface roughness effect became more significant as the film thickness decreased i.e. surface roughness effects were more profound in the thin film lubrication regime.

Hargreaves [59] presented a theoretical and experimental study to analyse the effect of surface waviness on the load carrying capacity of rectangular slider bearing. The surface waviness produced was sinusoidal in nature. It was observed that a predetermined surface waviness on the stationary pad of a rectangular slider bearing enhanced the load-carrying capacity of the bearing. The degree of enhancement, however, depended on the amplitude and frequency of the waviness pattern as well as the angle of tilt of the bearing pad. For larger angles of tilt, the increase in load-carrying capacity diminished. As the amplitude increased so did the change in pressure profile and hence the load-carrying capacity.

Wakuda et al. [60] experimentally verified the effect of surface texturing on the frictional properties in case of sliding contact bearings made of silicon nitride ceramic mated with hardened steel. From their experiment, the authors were able to verify that

surface texturing is an effective key to reducing friction. The effect of textured micro-dimples was retained even under severe friction conditions. They suggested that a well-lubricated sample with appropriate surface morphology succeeds in reducing the friction coefficient without forming undesirable tribochemical films. Further it was found that the dimple geometry had little influence on the frictional properties.

Tala-Ighil et al. [61] investigated the impact of surface texturing on key performance parameters of journal bearings, specifically focusing on spherical dimples. The study examined variations in maximum pressure, minimum film thickness, axial film flow, and friction torque. The results showed that increasing the dimple size led to higher maximum pressure and friction torque, while reducing the minimum film thickness and axial film flow. Additionally, increasing the dimple depth resulted in increased maximum pressure, friction torque, and axial film flow, accompanied by a further reduction in minimum film thickness.

Siripuram and Stephens [62] studied the effects of different shapes of deterministic micro asperities in case of sliding bearings for hydrodynamic lubrication. The different geometries of asperities considered were circular, square, diamond, hexagonal and triangular. By considering positive and negative asperities of constant height, the effects of asperity cross-sectional geometry were studied on friction and leakage. The authors found that the coefficient of friction was insensitive to the asperity shape but very much sensitive to the size of the cross section, whereas the leakage rates were found to be sensitive to both asperity shape and area of cross section. The smallest leakage rate was found in case of triangular asperities whereas square asperities gave the largest leakage. It was found that the minimum coefficient of friction for all asperity shapes occurred at an asperity area fraction of 0.2 for positive texture and 0.7 for negative texture. The study also indicated the existence of critical asperity area fraction where performance curves for positive and negative asperities crossed over.

Rahmani et al. [63] attempted to obtain the optimum geometrical parameter for square-shaped dimples in parallel thrust bearing in order to get the best tribological performance of the bearing, including load-carrying capacity and the friction parameter. From their analysis, they concluded that, increasing the number of dimples would not improve the performance of the bearing for partially textured surface with square-shaped

dimples. In case of the length ratio, the best performance was observed when dimples with length equal to their distance from each other were used. On the other hand, in case of height ratio, a ratio of about 1.50 to 1.57 would give the best performance.

Rajoub et al. [64] studied the steady state characteristics of a textured journal bearing. It was observed that the load carrying capacity of the textured bearing increased with the increase in eccentricity ratio whereas the Sommerfeld number and the friction variable decreased. Increasing the height of protrusion in textured journal bearing improved the dimensionless load-carrying capacity.

Tala-Ighil et al. [65] in 2011 studied the influence of texture location on performance of hydrodynamic journal bearings. The bearing surface was textured with cylindrical dimples. They found full texturing to be ineffective to generate hydrodynamic load capacity, whereas partial texturing could generate hydrodynamic lift when the texture was located in the declining part of the contact pressure field. In case of deep texture ($S < 1$), at eccentricity ratio 0.6, most improvement in bearing performances were observed when the second part of the bearing i.e. beyond 180° , was textured at the declining part of the pressure field.

Sharma et al. [66] investigated the steady-state performance of a journal bearing with triangular-shaped textures to enhance its overall efficiency. They observed that surface texturing was most effective in improving bearing performance when operating at lower eccentricity ratios and texture depths. The performance enhancement ratio, defined as the ratio of load-carrying capacity to the friction coefficient, reached a maximum value of 2.198 at a texture depth of 1.5 and an eccentricity ratio of 0.2, when the textured region was positioned in the increasing pressure zone.

Brizmer and Kligerman [67] presented a theoretical study on the application of Laser Surface Texturing (LST) in journal bearings. They analyzed the effects of both full-LST and partial-LST on the load-carrying capacity and attitude angle of the bearing. Their findings identified the most favourable LST mode and the optimal dimple texture parameters for maximizing load-carrying capacity.

Rao et al. [68] investigated the impact of texture/slip configurations on journal bearing performance concerning load-carrying capacity and the coefficient of friction. They presented a one-dimensional analysis of a partially textured slip journal bearing and

concluded that this configuration enhances load-carrying capacity while reducing the coefficient of friction. Among the various cases analyzed for concentric journal bearings, the groove region followed by the partially textured slip region exhibited the most significant improvement in non-dimensional load-carrying capacity and a reduction in friction.

Gupta et al. [69] studied the effect of surface texture on the performance of hydrodynamic journal bearing. In this experimental study, the authors used mechanical indentation texturing technique to incorporate the micro dimples on the bearing surface. Later they experimented on smooth and textured journal bearings with two oil holes located at $\pm 90^\circ$ to the load line. The experimental results showed that the pressure developed in the bearing increases when texture is present on the bearing surface. It was observed that with the increase in load (200N to 800N) at constant speed and constant oil supply pressure, the percentage increase of maximum pressure was more in case of textured bearing than in smooth bearing. Similar trend was seen when the speed was increased (1000rpm to 3000rpm) at constant load and constant oil supply pressure.

Li and Wang [70] performed a numerical analysis to examine the effect of surface texturing in the form of a bulge around a dimple on the tribological properties of a journal bearing. Their findings indicated that surface texturing can improve the tribological properties, such as the friction coefficient and eccentricity ratio. However, they also observed that it may have a negative impact on the load-carrying capacity.

Filho et al. [71] carried out an experimental study to evaluate the static performance parameters of a journal bearing with various texture geometries on its journal surface. Their findings indicated that surface texturing significantly influences the bearing's performance parameters.

Syed and Kakoty [72,73] attempted to improve the computational efficiency of dimple textured hydrodynamic journal bearing using progressive mesh densification (PMD) method. They used spherical dimples in their analysis and compared the results of PMD with the results of fixed mesh method and multigrid method. From their analysis they found that PMD method considerably decreases the computational time for textured bearing when compared to fixed mesh method and multigrid method.

Syed and Sarangi [74] studied the lubricating performance of textured parallel sliding contact bearings considering inertia effects. They considered different textures viz. Square, Circular, Hexagonal, Ellipsoidal, Elliptical and Triangular. A modified Reynolds equation was used to incorporate the inertia terms and finite different scheme was used in order to solve it. Results showed that the inertia effect was influential in altering the performance parameters of the bearing. They further found that, in case of positive texture, triangular shaped texture gave better load support and friction parameter for low modified Reynolds number, whereas with increasing modified Reynolds number beyond 0.4, hexagonal shaped textures showed better performance. Beyond 0.9, circular shaped performed the best. When the aspect ratio (area of surface textured/area of unit cell) was varied; for both positive and negative texture, in case of all shapes, the load carrying capacity and the end flow increased up to a certain value with increasing aspect ratio, and then decreased with further increase in aspect ratio. Triangular texture showed higher load support without considering inertia. However, when inertia was considered, the percentage changes in performance characters are negligible in case of triangular texture. Circular, hexagonal and square shapes showed higher percentage change in results. Improved performance parameters were observed with increased texture heights when the texture height was varied. The improvement was less in case of negative texture than in positive texture. Circular followed by hexagonal texture showed higher percentage changes in performance parameters among all shapes when inertia was considered. Further, for both positive and negative textures, the performance parameters decreased with the increase in the number of texture and then became constant expect for elliptical texture, where the results improved with the increase in number of textures.

Syed and Sarangi [75], in 2020, investigated the effects of positive and negative textures in terms of shape, size, height, orientation and number of textures in transverse direction, on the hydrodynamic performance of parallel sliding contact bearings in the turbulent regime. The authors used Ng and Pan model to incorporate the turbulent flow condition in the governing equation. It was observed that the load capacity and the end flow of the bearing improved in the turbulent regime as compared to the laminar regime; however the friction parameter showed higher values in turbulent regime, which was undesirable. Lower values of texture height ratio and the aspect ratio could be used in order to improve the performance in turbulent regime for positive texture, whereas lower

values of aspect ratio and higher values of texture height ratio could be preferred in case of negative texture.

Singh and Awasthi [76] theoretically studied the static, dynamic, and stability characteristics for various textured configurations of journal-bearing systems. They found that spherically/cylindrically textured bearings performed better than the other texture shapes.

Panigrahi and Sarangi [77] presented an experimental analysis to study the effects of texture size and texture height on the performance of hydrodynamic parallel sliding thrust bearings. They fabricated positive textures of different size and height with circular, elliptical, square and triangular cross-sections. The specimens were all made of mild steel. From the test results, they found that, under varying load and speed, all the textured surfaces produced lesser frictional torque and greater bearing clearance as compared to the untextured bearings. They also found that with the same texture height, bearings having small texture showed better tribological characteristics followed by medium and large texture size. Furthermore, it was observed that with the same texture size, a higher value of texture height produces better hydrodynamic performance for all shapes.

Syed et al. [78], in an experimental work, studied the effects of positive square shaped textures on the performance characteristics like film thickness and frictional torque of thrust bearing by varying the load and speed. The textures were made of Aluminium foil having an area of 100 mm^2 and a thickness of $5 \text{ }\mu\text{m}$. The textures were attached in an orientation such that the flow was towards the edge of the texture. The authors concluded that in the case of low loads, the film thickness decreased as the speed was increased whereas in case of high loads, the film thickness increased with the increasing speed. Frictional torque was found to be increasing as both speed and load were increased. However, the values of frictional torque in case of textured case were less than plain bearing case. Thus, textured thrust pad bearing gave higher load carrying capacity and lower value of frictional torque than plain thrust bearing.

Tala-Ighil et al. [79] studied the effects of deterministic texture shapes on the performance of hydrodynamic journal bearings. The different texture shapes used were spherical, cylindrical and parallelepipedic texture. They found that the presence of textures in journal bearing improved its performance compared to a plain bearing. The

parallelepipedic textures show advantages compared to the other geometries for the improvement of the performances of the bearing.

Syed and Sarangi [80] carried out numerical analysis to study the effect of texture orientation on the hydrodynamic performance characteristics of parallel sliding contacts. Two types of textures were used in the analysis viz. triangular and elliptical with maximum value of aspect ratio 0.3 and 0.38 respectively. The different angular orientations considered were 0° , 30° , 60° and 90° . From their analysis, it was found that positive textures showed better performance characteristics than negative textures in case of plain slider bearings. Orientation of positive textures had considerable effects on the hydrodynamic performance on the parallel sliding contacts, whereas, in case of negative texture, angular orientation may show positive or negative impact on the hydrodynamic performance depending upon the texture shapes. In case of positive texture, the 60° triangular and 90° elliptical orientation showed better performance than the other orientations. The same research group [81], as mentioned above, studied the performance of square shaped textured parallel sliding contacts under the combined influence of both fluid inertia and slip at the fluid-solid interface. The authors found that, when only inertia was considered, the effect of smaller values of modified Reynolds number was negligible, however, in case of combined fluid slip and inertia, smaller values of modified Reynolds number showed significant changes in load carrying capacity and end flow parameters, whereas the effect on friction parameter was negligible.

Cupillard et al. [82] studied the effects of surface texture on bearing friction and load carrying capacity using computational fluid dynamics. The authors observed that textured surface affected the performance of the journal bearings by reducing the friction coefficient for deep dimples located in maximum pressure region at high eccentricity ratio and for shallow dimples located at downstream of maximum fluid film at low eccentricity ratio. They also noticed an additional pressure build up due to surface texture at low eccentricity ratios. The same authors, in 2009, [83] presented a flow analysis carried out for a parallel textured slider to investigate the role of fluid inertia for a laminar, two-dimensional, steady and isothermal flow. From their study, they found the existence of critical value of texture depth, above which negative inertia effects were encountered and below which positive inertia effects were observed in case of load carrying capacity. In

addition to the critical texture depth, there existed an optimal texture depth, greater than the critical depth, which gave the maximum load carrying capacity.

Sinanoğlu et al. [84] studied the effects of shaft surface texturing on the performance of journal bearing pressure and consequently on the load carrying capacity, both experimentally and theoretically. The surface of the shafts has been in two types - smooth, that is, without profiles; with profiles, that is, trapezoidal and saw. They found that the trapezoidal shaft can carry more loads than the saw shafts. In addition, the shaft that has the same profile but a lower profile height and pitch value can carry fewer loads.

Yamada et al. [85,86] numerically and experimentally studied the dynamic characteristics of square textured journal bearing considering inertia effects. They observed that the stability-threshold shaft speed of the rotor supported by textured bearings with a large number of small dimples became higher than that supported by smooth surface bearings, especially in the range of higher Reynolds number.

Taura [87] studied the effects of square texturing on static and dynamic characteristics of partially textured journal bearings considering fluid inertia effect. To check the stability of the bearing the author applied Routh-Hurwitz stability criterion. From the analysis the author concluded that an appropriate partial texturing on bearing surface can improve the load carrying capacity and the stability characteristics of the bearing. Further they found that the start angle of the texture region should be set at 270° from the top of the bearing in the rotating direction to improve the bearing characteristics.

Ganji and Kakoty [88] numerically analysed the dynamic characteristics and stability of cylindrical textured hydrodynamic journal bearing. Stiffness and damping coefficients of fluid film and stability parameter are found using the first-order perturbation method for different eccentricity ratios and various texture parameters like texture depth and texture density. From the analysis the authors have found that the stability is enhanced with increase in texture depth, whereas there is an optimum texture density corresponding to the maximum stability of the bearing.

Smolík et al. [89] investigated the influences of mechanically indented texture in the case of fluid-film instability of journal bearings. They noticed considerable improvement in the stability, for low specific loads, when textures are located at the minimum film thickness region.

The effect of varnish on the stability of journal bearings was investigated by Jang et al. [90]. They concluded that the effect of varnishing led to a reduction in the stability of the bearing. Wang et al. [91] carried out a time transient stability analysis of offset-elliptical journal bearings under varying load and misalignment. Their study demonstrated satisfactory transient performance for offset-elliptical journal bearings. Gropper et al. [92] published a comprehensive review on the hydrodynamic performance of textured surfaces.

Sharma et al. [93] analyzed the dynamic and stability performance for triangular shaped textured journal bearing and suggested optimum texturing parameters for maximum performance and stability for triangular shaped textured journal bearings.

Byotra and Sharma [94,95] studied the static and dynamic characteristics of journal bearing with crescent shaped texture using nano lubricants and found that the crescent geometry surface texturing in the pressure-increasing region enhanced the stability parameters. Further, it was observed that the addition of nano lubricant additives enhanced the load-carrying capacity of textured journal bearings.

The dynamic characteristics of chevron shaped textured journal bearing was investigated by Jamwal et al. [96] and estimated the optimum texture depth and quantity of chevron shaped texture for maximum stability of journal bearing.

1.2.4 Cavitation in Hydrodynamic Bearings

Elrod [5], 1981, first proposed an algorithm incorporating the JFO boundary conditions to solve a modified form of the Reynolds equation. He used a switch function to automatically predict the Cavitation and the full film regions, thereby predicting the pressure distribution. Fesanghary and Khonsari [97] later modified the switch function, improving Elrod's algorithm's stability and convergence speed. Vijayaraghavan and Keith [98] used alternating-direction implicit (ADI) method to solve the cavitation algorithm for journal and slider bearing.

Qiu and Khonsari [99] analyzed the cavitation phenomenon in dimple-enhanced textured surfaces in mechanical seal-like structures. From the results, the authors have concluded that the JFO theory with an appropriate implementation algorithm can predict

Cavitation in dimples and give more realistic performance parameters than other boundary conditions.

Manser et al. [100] numerically studied the influence of surface texture geometries on the hydrodynamic journal-bearing performance using JFO boundary conditions. Pattanayak et al. [101] investigated the effects of bionic textures in the case of journal bearings considering mass conservation. They found that bionic texturing improves journal bearings' static and dynamic properties.

Syed and Kakoty [102] implemented the JFO boundary conditions to investigate the influence of protrusion and dimple spherical textures on the performance characteristics of journal bearings. They found that protrusion texturing showed better friction variables, whereas higher load capacity and flow coefficient were observed in the case of dimple texturing.

Ausas et al. [103] numerically analyzed the impact of the cavitation model in the case of microtextured journal bearings. Using the mass-conserving cavitation model, Usman and Park [104] investigated the tribological performance of textured hydrodynamic journal bearings under varying operating conditions. They noticed a significant improvement in the frictional characteristics.

Jamari et al. [105] studied the correlation between the cavitation and the inertia effects while considering the slip in the bearings. The authors concluded that inertia effects significantly affected the cavitation, as the presence of inertia in textured bearings decelerated the cavitation phenomenon. Further, the slip boundary reduced the cavitation area in the bearing. In case of low-inertia bearing, the slip effect became more dominant in changing the hydrodynamic pressure profiles than high-inertia bearings.

Tauviqirrahman et al. [106] studied the relation between inertia effect and the cavitation in case of a textured parallel sliding contact bearing using computational fluid dynamics approach. From the simulated results, the authors concluded that the inertia terms affected the occurrence of the cavitation strongly. The presence of slip in the bearings further modified the changes which were studied in a later work.

Panigrahi and Sarangi [107] studied the cavitation phenomenon of positive textured surfaces under full film lubrication condition on parallel thrust bearings with

rectangular textures. From the experiment, it was observed that hydrodynamic pressure development was completely influenced by cavitation pressure that occurred due to the presence of deterministic textures. The friction force increased with increasing speed at a particular load. The cavitation pressure also increased with the increase in speed leading to hydrodynamic pressure development. Hence, the film thickness increased and the recess pressure decreased with the increase in speed at a particular load.

Sawicki and Rao [108] analysed the effects of cavitation on the stability of submerged journal bearings. Guo [109] conducted a theoretical study on the effect of micro-spherical and cylindrical dimple textures on the load-carrying capacity and lubrication performance of journal bearings with axial grooves, using the JFO boundary conditions.

Dobrica et al. [110] proposed an in-depth study on the influence of cavitation and of different texturing parameters, especially the dimple depth, the texture extent, and the dimple aspect, on the hydrodynamic performance of textured contacts. From their analysis they found that cavitation had a detrimental effect on fully textured parallel slider bearing; however, had positive effects on partially textured parallel sliders, increasing the inlet flow (inlet suction) and allowing the development of full lubrication at some distance from the leading edge. In convergent sliders, cavitation had minimal influence.

1.3 Summary of Literature Review and Research Gap

Hydrodynamic journal bearings have been one of the most important of all types of bearings in various engineering applications due to their self-acting nature, allowing them to effectively support the applied load. Over the years, extensive research has been conducted to evaluate and enhance or optimize their performance characteristics such as load-carrying capacity, friction coefficient, and flow parameters – both numerically and experimentally. Among the various techniques explored, surface texturing has emerged as a promising approach for enhancing the tribological performance of journal bearings. Studies have shown that incorporating surface textures – such as grooves, discrete protrusions, dimples, and modifications in surface roughness and geometry – can significantly influence the hydrodynamic lubrication characteristics.

Lubricant inertia, which is often neglected in classical lubrication theory, has been found to influence the performance of hydrodynamic bearings, particularly at high speed and in the case of low-viscosity lubricants. While substantial work has been carried out to estimate the effects of surface texturing in the static and dynamic characteristics of hydrodynamic bearings, there have been limited studies to explore the role of lubricant inertia in textured bearings. Previous studies on lubricant inertia have primarily focused on parallel slider bearings, leaving a significant gap in understanding its influence on textured journal bearings. Additionally, while the influence of lubricant inertia on steady-state operation has been found to be relatively minor, its impact on bearing stability is substantial. Stability is a critical factor in the reliable operation of journal bearings, as instability can lead to issues such as half-frequency whirling ending up with oil whip and ultimately affecting the longevity and efficiency of the machinery.

Another significant factor influencing the tribological performance of textured journal bearings is cavitation. However, existing studies on the performance of textured hydrodynamic journal bearings while considering lubricant inertia effects have largely overlooked the role of cavitation. Reynolds boundary conditions are widely used to model cavitation in bearings due to their simplicity, whereas the more accurate Jakobsson-Floberg-Olsson (JFO) boundary conditions, are less frequently used in practice, due to difficulty in implementation. While the onset of cavitation is accurately predicted by Reynolds boundary conditions, the location of film reformation is not captured. The JFO conditions address this limitation by ensuring mass conservation throughout the lubricant film. Despite the individual importance of both fluid inertia and cavitation, no comprehensive study has simultaneously assessed the combined influences of lubricant inertia and cavitation on the performance characteristics of textured hydrodynamic journal bearings.

Furthermore, while the effects of surface texturing and lubricant inertia have been extensively studied individually, their combined influence on journal bearing stability has not been explored. Given the growing demand for high-speed machinery and the use of unconventional lubricants such as water and liquid metals, understanding this combined effect is crucial. The stability of journal bearings depends on parameters such as the critical mass parameter (a function of speed) and the whirl ratio, which have not been

systematically analyzed for different texturing geometries under the influence of lubricant inertia.

Thus, a significant research gap exists in understanding how surface texturing and lubricant inertia effect together influence the stability of hydrodynamic journal bearings. Addressing this gap is crucial for developing more stable and efficient bearing designs, particularly in high-speed and low-viscosity lubrication conditions.

1.4 Scope of the Present Work

In view of the above gaps in the existing literature, an attempt has been made to address them through the present study, which deals with the estimation of the steady-state and stability characteristics of textured hydrodynamic journal bearings while considering the combined effects of lubricant inertia and cavitation. The following objectives have been drawn accordingly.

1.4.1 Objectives

1. To study the effect of lubricant inertia on the performance of textured hydrodynamic journal bearings considering Reynolds boundary conditions.
2. To derive a novel modified Reynolds equation incorporating both lubricant inertia effect and cavitation effects and to utilize the equation for steady-state analysis and characterization of textured journal bearings.
3. To perform a nonlinear stability analysis of a textured journal bearing with lubricant inertia effect.

1.5 Organization of the Thesis

The present study deals with the estimation of the steady-state and stability characteristics of textured hydrodynamic journal bearings while considering the combined effects of lubricant inertia and cavitation. The present thesis is broadly divided into six chapters.

Chapter 1 provides a comprehensive review of the current state of research on hydrodynamic journal bearings. The objectives for the present work have been drawn based on the extensive literature review in this chapter.

Chapter 2 outlines the theoretical framework for textured journal bearings, incorporating both Reynolds boundary conditions and mass-conserving Jakobsson-Floberg-Olsson (JFO) boundary conditions, to ascertain the influence of lubricant inertia. The computationally efficient progressive mesh densification (PMD) [72,73,111] method has also been implemented in the steady-state analysis to accelerate the convergence process. The chapter, further, includes the theoretical formulations for the non-linear time transient analysis for textured journal bearings incorporating the lubricant inertia effect.

Chapter 3 presents the steady-state performance analysis of textured journal bearings under the influence of lubricant inertia using Reynolds boundary conditions.

In Chapter 4, the combined influence of cavitation and lubricant inertia on the performance characteristics of textured journal bearings is analyzed, incorporating the mass-conserving Jakobsson-Floberg-Olsen (JFO) boundary conditions.

Chapter 5 investigates the dynamic stability of textured journal bearings considering lubricant inertia. The stability performance of textured journal bearings has been explored by determining the critical mass parameter, a function of speed, and the whirl ratio for different texturing geometries. A non-linear time-transient method is used to simulate the journal centre trajectory and generate stability maps, providing deeper insights into the role of surface texturing in improving bearing stability.

Finally, the major inferences and conclusions derived from the work conducted in this thesis are presented in Chapter 6.

Basic Equations, Boundary Conditions and Computational Methods

Contents

Basic Equations, Boundary Conditions and Computational Methods	31
2.1 Introduction	33
2.2 Theory for Textured Journal Bearing with Lubricant Inertia Effect using Reynolds Boundary Conditions	33
2.2.1 Modified Reynolds Equation incorporating Fluid Inertia Effect	33
2.2.2 Modified Reynolds Equation for Textured Journal Bearing incorporating Fluid Inertia Effect	38
2.2.3 Numerical Solution	40
2.2.4 Performance Characteristics	42
2.2.5 Reynolds Boundary Conditions	46
2.2.6 Stability Analysis of Textured Journal Bearing	46
2.3 Theory for Textured Journal Bearing with Lubricant Inertia Effect using Mass-Conserving (JFO) Boundary Conditions	49
2.3.1 Governing Equation	49
2.3.2 Numerical Solution	51
2.3.3 Performance Characteristics	55
2.4 Fluid Film Thickness	55
2.5 Progressive Mesh Densification	56
2.6 Summary	57



and the ratio of eccentricity to the radial clearance is known as the eccentricity ratio (ε). A bearing is said to be a lightly loaded bearing when $\varepsilon \leq 0.4$, whereas for $0.4 < \varepsilon$, the bearing is known as heavily loaded bearing [112].

The generalized Reynolds equation, formulated by Reynolds [8] does not account for the lubricant inertia effect. Therefore, it is necessary to derive the governing equation from the Navier-Stokes equation and continuity equation incorporating the lubricant inertia effect.

The Navier-Stokes equations are given by [112]

$$\rho \frac{Du}{Dt} = \rho X - \frac{\partial p}{\partial x} + \frac{\partial}{\partial x} \left\{ \eta \left[2 \frac{\partial u}{\partial x} - \frac{2}{3} \left(\frac{\partial u}{\partial x} + \frac{\partial v}{\partial y} + \frac{\partial w}{\partial z} \right) \right] \right\} + \frac{\partial}{\partial y} \left[\eta \left(\frac{\partial u}{\partial y} + \frac{\partial v}{\partial x} \right) \right] + \frac{\partial}{\partial z} \left[\eta \left(\frac{\partial w}{\partial x} + \frac{\partial u}{\partial z} \right) \right] \quad (2.1)$$

$$\rho \frac{Dv}{Dt} = \rho Y - \frac{\partial p}{\partial y} + \frac{\partial}{\partial y} \left\{ \eta \left[2 \frac{\partial v}{\partial y} - \frac{2}{3} \left(\frac{\partial u}{\partial x} + \frac{\partial v}{\partial y} + \frac{\partial w}{\partial z} \right) \right] \right\} + \frac{\partial}{\partial z} \left[\eta \left(\frac{\partial v}{\partial z} + \frac{\partial w}{\partial y} \right) \right] + \frac{\partial}{\partial x} \left[\eta \left(\frac{\partial u}{\partial y} + \frac{\partial v}{\partial x} \right) \right] \quad (2.2)$$

$$\rho \frac{Dw}{Dt} = \rho Z - \frac{\partial p}{\partial z} + \frac{\partial}{\partial z} \left\{ \eta \left[2 \frac{\partial w}{\partial z} - \frac{2}{3} \left(\frac{\partial u}{\partial x} + \frac{\partial v}{\partial y} + \frac{\partial w}{\partial z} \right) \right] \right\} + \frac{\partial}{\partial x} \left[\eta \left(\frac{\partial w}{\partial x} + \frac{\partial u}{\partial z} \right) \right] + \frac{\partial}{\partial y} \left[\eta \left(\frac{\partial v}{\partial z} + \frac{\partial w}{\partial y} \right) \right] \quad (2.3)$$

where u , v , and w are velocities in x , y , and z directions. p is the pressure in the fluid film. $\frac{Du}{Dt}$, $\frac{Dv}{Dt}$, and $\frac{Dw}{Dt}$ are the three components of acceleration.

where

$$\left. \begin{aligned} \frac{Du}{Dt} &= u \frac{\partial u}{\partial x} + v \frac{\partial u}{\partial y} + w \frac{\partial u}{\partial z} + \frac{\partial u}{\partial t} \\ \frac{Dv}{Dt} &= u \frac{\partial v}{\partial x} + v \frac{\partial v}{\partial y} + w \frac{\partial v}{\partial z} + \frac{\partial v}{\partial t} \\ \frac{Dw}{Dt} &= u \frac{\partial w}{\partial x} + v \frac{\partial w}{\partial y} + w \frac{\partial w}{\partial z} + \frac{\partial w}{\partial t} \end{aligned} \right\} \quad (2.4)$$

Again, the continuity equation is given by,

$$\frac{\partial \rho}{\partial t} + \frac{\partial}{\partial x}(\rho u) + \frac{\partial}{\partial y}(\rho v) + \frac{\partial}{\partial z}(\rho w) = 0 \quad (2.5)$$

The assumptions to be followed are as follows

- i. Body force terms are negligible compared to the pressure, inertia, and viscous force terms.
- ii. There is no variation of pressure across the fluid film, $\frac{\partial p}{\partial y} = 0$.
- iii. There is no slip in the fluids-solid boundaries.
- iv. No external forces act on the film.
- v. The flow is viscous and laminar.
- vi. Due to the geometry of fluid film, the derivatives of u and w with respect to y are much larger than other derivatives of velocity components.

The Equations (2.1), (2.2) and (2.3) after the application of the above assumptions, becomes

$$\rho \left(\frac{\partial u}{\partial t} + u \frac{\partial u}{\partial x} + v \frac{\partial u}{\partial y} + w \frac{\partial u}{\partial z} \right) = -\frac{\partial p}{\partial x} + \eta \frac{\partial^2 u}{\partial y^2} \quad (2.6)$$

$$\rho \left(\frac{\partial w}{\partial t} + u \frac{\partial w}{\partial x} + v \frac{\partial w}{\partial y} + w \frac{\partial w}{\partial z} \right) = -\frac{\partial p}{\partial z} + \eta \frac{\partial^2 w}{\partial y^2} \quad (2.7)$$

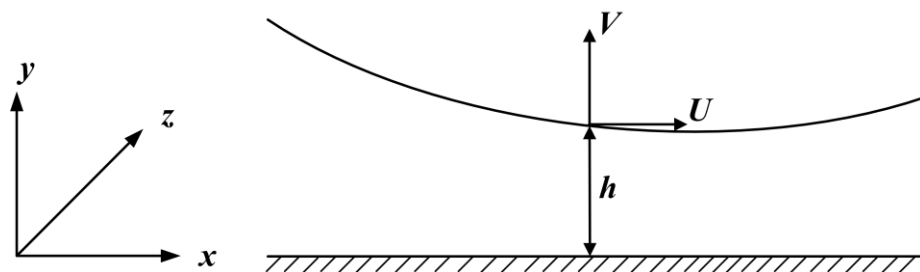


Fig. 2.2. The fluid film

The schematic diagram of the fluid film with the flow velocities is shown in Fig.

2.2. Flow velocities at the boundaries are:

$$\begin{array}{l} \text{At } y = 0 \quad u = 0 \quad v = 0 \quad w = 0 \\ \text{At } y = h \quad u = U \quad v = V \quad w = 0 \end{array} \quad (2.8)$$

Non-dimensional forms of equations (2.6), (2.7) and (2.5) respectively are

$$Re^* \left[\frac{\partial \bar{u}}{\partial \tau} + \bar{u} \frac{\partial \bar{u}}{\partial \theta} + \bar{v} \frac{\partial \bar{u}}{\partial \bar{y}} + \left(\frac{D}{L} \right) \bar{w} \frac{\partial \bar{u}}{\partial \bar{z}} \right] = - \frac{\partial \bar{p}}{\partial \theta} + \frac{\partial^2 \bar{u}}{\partial \bar{y}^2} \quad (2.9)$$

$$Re^* \left[\frac{\partial \bar{w}}{\partial \tau} + \bar{u} \frac{\partial \bar{w}}{\partial \theta} + \bar{v} \frac{\partial \bar{w}}{\partial \bar{y}} + \left(\frac{D}{L} \right) \bar{w} \frac{\partial \bar{w}}{\partial \bar{z}} \right] = - \left(\frac{D}{L} \right) \frac{\partial \bar{p}}{\partial \bar{z}} + \frac{\partial^2 \bar{w}}{\partial \bar{y}^2} \quad (2.10)$$

$$\frac{\partial \rho}{\partial \tau} + \frac{\partial}{\partial \theta} (\rho \bar{u}) + \frac{\partial}{\partial \bar{y}} (\rho \bar{v}) + \left(\frac{D}{L} \right) \frac{\partial}{\partial \bar{z}} (\rho \bar{w}) = 0 \quad (2.11)$$

where,

$$\begin{array}{l} \bar{u} = u/R\omega \quad \bar{v} = v/C\omega \quad \bar{w} = w/R\omega \quad Re^* = (C/R)Re \\ x = R\theta \quad \bar{y} = y/C \quad \bar{z} = z/(L/2) \quad \tau = \omega t \quad \bar{p} = pC^2/\eta\omega R^2 \end{array} \quad (2.12)$$

Kakoty and Majumdar [43] considered laminar flow with parabolic velocity profiles of the velocity components. The parabolic velocity components are expressed in non-dimensional form as follows:

$$\bar{u} = \bar{y}/\bar{h} + Q_\theta \left\{ \left(\bar{y}^2/\bar{h}^2 \right) - \left(\bar{y}/\bar{h} \right) \right\} \quad (2.13)$$

$$\bar{w} = Q_z \left\{ \left(\bar{y}^2/\bar{h}^2 \right) - \left(\bar{y}/\bar{h} \right) \right\} \quad (2.14)$$

Substituting Equations (2.13) and (2.14) in Equations (2.9) and (2.10) and integrating:

$$Q_\theta = \frac{\bar{h}^2}{2} \frac{\partial \bar{p}}{\partial \theta} + Re^* I_\theta \quad (2.15)$$

$$Q_z = \frac{\bar{h}^2}{2} \left(\frac{D}{L} \right) \frac{\partial \bar{p}}{\partial \bar{z}} + Re^* I_z \quad (2.16)$$

Integrating Equation (2.11), the modified Reynolds equation is obtained as:

$$\frac{\partial}{\partial \theta} \left(\bar{h}^3 \frac{\partial \bar{p}}{\partial \theta} \right) + \left(\frac{D}{L} \right) \frac{\partial}{\partial \bar{z}} \left(\bar{h}^3 \frac{\partial \bar{p}}{\partial \bar{z}} \right) = 12\bar{V} - 6 \frac{\partial \bar{h}}{\partial \theta} - Re^* \left(\frac{\partial (\bar{h} I_\theta)}{\partial \theta} + \left(\frac{D}{L} \right) \frac{\partial (\bar{h} I_{\bar{z}})}{\partial \bar{z}} \right) \quad (2.17)$$

where

$$\bar{V} = \frac{\partial \bar{h}}{\partial \theta} + \frac{\partial \varepsilon}{\partial \tau} \cos \theta + \varepsilon \frac{\partial \theta}{\partial \tau} \sin \theta \quad (2.18)$$

$$I_\theta = \frac{\bar{h}}{2} \left[-\frac{1}{2} \left(\frac{\partial \bar{h}}{\partial \tau} + \frac{4}{3} \frac{\partial \bar{h}}{\partial \theta} - 2\bar{V} + \left(\frac{D}{L} \right) \frac{\bar{h}}{6} \frac{\partial Q_{\bar{z}}}{\partial \bar{z}} \right) - \frac{Q_\theta}{6} \left(\frac{\partial \bar{h}}{\partial \tau} + \frac{\partial \bar{h}}{\partial \theta} - \left(\frac{D}{L} \right) \frac{\bar{h}}{5} \frac{\partial Q_{\bar{z}}}{\partial \bar{z}} \right) - \frac{\bar{h}}{6} \left(\frac{\partial Q_\theta}{\partial \tau} + \frac{\partial Q_\theta}{\partial \theta} - \left(\frac{D}{L} \right) \frac{Q_{\bar{z}}}{5} \frac{\partial Q_\theta}{\partial \bar{z}} \right) + \frac{Q_\theta}{15} \left(\bar{h} \frac{\partial Q_\theta}{\partial \theta} + \frac{Q_\theta}{2} \frac{\partial \bar{h}}{\partial \theta} \right) - \left(\frac{D}{L} \right) \frac{Q_{\bar{z}}}{6} \left(\frac{1}{2} \frac{\partial \bar{h}}{\partial \bar{z}} - \frac{Q_\theta}{5} \frac{\partial \bar{h}}{\partial \bar{z}} \right) \right] \quad (2.19)$$

$$I_{\bar{z}} = \frac{\bar{h}}{2} \left[\left(\frac{D}{L} \right) \frac{Q_{\bar{z}}^2}{30} \frac{\partial \bar{h}}{\partial \bar{z}} - \frac{\bar{h}}{6} \left(\frac{\partial Q_{\bar{z}}}{\partial \tau} + \frac{1}{2} \frac{\partial Q_{\bar{z}}}{\partial \theta} - \frac{Q_{\bar{z}}}{5} \frac{\partial Q_\theta}{\partial \theta} \right) + \frac{\bar{h}}{15} \left(\frac{Q_\theta}{2} \frac{\partial Q_{\bar{z}}}{\partial \theta} + Q_{\bar{z}} \left(\frac{D}{L} \right) \frac{\partial Q_{\bar{z}}}{\partial \bar{z}} \right) - \frac{Q_{\bar{z}}}{6} \left(\frac{\partial \bar{h}}{\partial \tau} + \frac{1}{2} \frac{\partial \bar{h}}{\partial \theta} - \frac{Q_\theta}{5} \frac{\partial \bar{h}}{\partial \theta} \right) \right] \quad (2.20)$$

Equation (2.17) represents the Modified Reynolds equation incorporating the lubricant inertia effect. The 2nd term on the right-hand side of Equation (2.17) refers to the effect of lubricant inertia. In the case of steady-state analysis, the time varying terms are neglected. Hence, the Equations (2.17), (2.19) and (2.20) become:

$$\frac{\partial}{\partial \theta} \left(\bar{h}^3 \frac{\partial \bar{p}}{\partial \theta} \right) + \left(\frac{D}{L} \right) \frac{\partial}{\partial \bar{z}} \left(\bar{h}^3 \frac{\partial \bar{p}}{\partial \bar{z}} \right) = 6 \frac{\partial \bar{h}}{\partial \theta} - Re^* \left(\frac{\partial (\bar{h} I_\theta)}{\partial \theta} + \left(\frac{D}{L} \right) \frac{\partial (\bar{h} I_{\bar{z}})}{\partial \bar{z}} \right) \quad (2.21)$$

$$I_\theta = \frac{\bar{h}}{2} \left[-\frac{1}{2} \left(\frac{4}{3} \frac{\partial \bar{h}}{\partial \theta} + \left(\frac{D}{L} \right) \frac{\bar{h}}{6} \frac{\partial Q_{\bar{z}}}{\partial \bar{z}} \right) - \frac{Q_\theta}{6} \left(\frac{\partial \bar{h}}{\partial \theta} - \left(\frac{D}{L} \right) \frac{\bar{h}}{5} \frac{\partial Q_{\bar{z}}}{\partial \bar{z}} \right) - \frac{\bar{h}}{6} \left(\frac{\partial Q_\theta}{\partial \theta} - \frac{Q_{\bar{z}}}{5} \left(\frac{D}{L} \right) \frac{\partial Q_\theta}{\partial \bar{z}} \right) + \frac{Q_\theta}{15} \left(\bar{h} \frac{\partial Q_\theta}{\partial \theta} + \frac{Q_\theta}{2} \frac{\partial \bar{h}}{\partial \theta} \right) + \left(\frac{D}{L} \right) \left(-\frac{Q_{\bar{z}}}{12} + \frac{Q_\theta Q_{\bar{z}}}{30} \right) \frac{\partial \bar{h}}{\partial \bar{z}} \right] \quad (2.22)$$

$$I_{\bar{z}} = \frac{\bar{h}}{2} \left[\left(\frac{D}{L} \right) \frac{Q_{\bar{z}}^2}{30} \frac{\partial \bar{h}}{\partial \bar{z}} - \frac{\bar{h}}{6} \left(\frac{1}{2} \frac{\partial Q_{\bar{z}}}{\partial \theta} - \frac{Q_{\bar{z}}}{5} \frac{\partial Q_\theta}{\partial \theta} \right) + \frac{\bar{h}}{15} \left(\frac{Q_\theta}{2} \frac{\partial Q_{\bar{z}}}{\partial \theta} + Q_{\bar{z}} \left(\frac{D}{L} \right) \frac{\partial Q_{\bar{z}}}{\partial \bar{z}} \right) - \frac{Q_{\bar{z}}}{6} \left(\frac{1}{2} \frac{\partial \bar{h}}{\partial \theta} - \frac{Q_\theta}{5} \frac{\partial \bar{h}}{\partial \theta} \right) \right] \quad (2.23)$$

2.2.2 Modified Reynolds Equation for Textured Journal Bearing incorporating Fluid Inertia Effect

In the preceding subsection, a modified form of the Reynolds equation accounting for lubricant inertia effect was presented. To extend this formulation for textured journal bearings, it is essential to derive a further modified form of the Reynolds equation by incorporating the surface texture parameters. This is accomplished by substituting the texture parameters from Equation (2.24) into the Modified Reynolds equation given in Equation (2.21). The resulting equation, which incorporates the combined effects of surface texturing and the effect of lubricant inertia, has not been previously reported in the literature and has been derived as a novel contribution of the present work. This subsection presents the derivation of this newly formulated modified Reynolds equation.

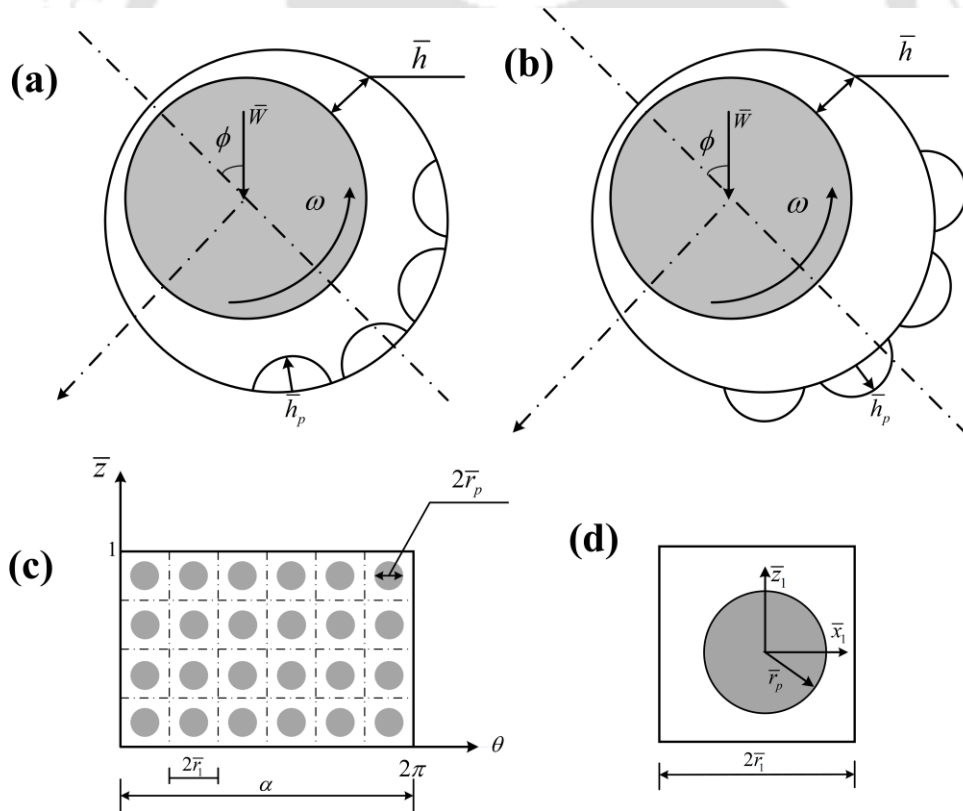


Fig. 2.3. Textured journal bearing with (a) protrusion; (b) dimple texture; (c) developed view of a hydrodynamic journal bearing with texturing; (d) micro texture inside an imaginary unit cell

Figure 2.3 (a) and 2.3 (b) show the schematic of a textured journal bearing with protrusion and dimple texturing. Fig. 2.3 (c) shows the developed view of textured journal bearing, whereas Fig. 2.3 (d) shows one micro texture inside an imaginary unit cell. The non-dimensional parameters used for defining protruded and dimple texture are as follows:

$$x = R\theta; \bar{z} = z/(L/2); \delta = C/2r_p; \bar{R} = R/r_p; \bar{L} = L/r_p; \bar{h}_p = h_p/C; \bar{h} = h/C \quad (2.24)$$

$$\theta_1 = x/r_p = \bar{R}\theta; \bar{z}_1 = z/r_p = \bar{z}\bar{L}/2; \psi = h_p/2r_p; S_p = (\pi r_p^2)/(4r_1^2); \bar{p}_1 = 2r_p p/3\eta U$$

Substituting the non-dimensional texturing parameters from Equation (2.24), Equations (2.15), (2.16), (2.21), (2.22), and (2.23) become

$$\frac{\partial}{\partial \theta_1} \left(\bar{h}^3 \frac{\partial \bar{p}_1}{\partial \theta_1} \right) + \frac{\partial}{\partial \bar{z}_1} \left(\bar{h}^3 \frac{\partial \bar{p}_1}{\partial \bar{z}_1} \right) = \frac{1}{\delta^2} \frac{\partial \bar{h}}{\partial \theta_1} - \frac{Re^*}{3\delta^2} \left(\frac{\partial (\bar{h}I_{\theta_1})}{\partial \theta_1} + \frac{\partial (\bar{h}I_{\bar{z}_1})}{\partial \bar{z}_1} \right) \quad (2.25)$$

$$Q_{\theta_1} = 3\delta^2 \bar{h}^2 \frac{\partial \bar{p}_1}{\partial \theta_1} + Re^* I_{\theta_1} \quad (2.26)$$

$$Q_{\bar{z}_1} = 3\delta^2 \bar{h}^2 \frac{\partial \bar{p}_1}{\partial \bar{z}_1} + Re^* I_{\bar{z}_1} \quad (2.27)$$

$$I_{\theta_1} = \frac{\bar{R}\bar{h}}{2} \left[-\frac{1}{2} \left(\frac{4}{3} \frac{\partial \bar{h}}{\partial \theta_1} + \frac{\bar{h}}{6} \frac{\partial Q_{\bar{z}_1}}{\partial \bar{z}_1} \right) - \frac{Q_{\theta_1}}{6} \left(\frac{\partial \bar{h}}{\partial \theta_1} - \frac{\bar{h}}{5} \frac{\partial Q_{\bar{z}_1}}{\partial \bar{z}_1} \right) - \frac{\bar{h}}{6} \left(\frac{\partial Q_{\theta_1}}{\partial \theta_1} - \frac{Q_{\bar{z}_1}}{5} \frac{\partial Q_{\theta_1}}{\partial \bar{z}_1} \right) + \frac{Q_{\theta_1}}{15} \left(\frac{\partial Q_{\theta_1}}{\partial \theta_1} + \frac{Q_{\theta_1}}{2} \frac{\partial \bar{h}}{\partial \theta_1} \right) + \left(-\frac{Q_{\bar{z}_1}}{12} + \frac{Q_{\theta_1} Q_{\bar{z}_1}}{30} \right) \frac{\partial \bar{h}}{\partial \bar{z}_1} \right] \quad (2.28)$$

$$I_{\bar{z}_1} = \frac{\bar{R}\bar{h}}{2} \left[-\frac{Q_{\bar{z}_1}}{6} \left(\frac{1}{2} \frac{\partial \bar{h}}{\partial \theta_1} - \frac{Q_{\theta_1}}{5} \frac{\partial \bar{h}}{\partial \theta_1} \right) - \frac{\bar{h}}{6} \left(\frac{1}{2} \frac{\partial Q_{\bar{z}_1}}{\partial \theta_1} - \frac{Q_{\bar{z}_1}}{5} \frac{\partial Q_{\theta_1}}{\partial \theta_1} \right) + \frac{\bar{h}}{15} \left(\frac{Q_{\theta_1}}{2} \frac{\partial Q_{\bar{z}_1}}{\partial \theta_1} + Q_{\bar{z}_1} \frac{\partial Q_{\bar{z}_1}}{\partial \bar{z}_1} \right) + \frac{Q_{\bar{z}_1}^2}{30} \frac{\partial \bar{h}}{\partial \bar{z}_1} \right] \quad (2.29)$$

Equation (2.25), derived above, represents the modified Reynolds equation for textured bearing incorporating the lubricant inertia effect. The second term on the right-hand side of Equation (2.25) accounts for the influence of lubricant inertia. When the modified Reynolds number (Re^*) is set to zero, this term vanishes, corresponding to a

condition with no inertia effects. As the value of Re^* increases, the impact of lubricant inertia becomes more pronounced. Furthermore, if Re^* is set to zero and the texturing parameters are omitted, Equation (2.25) reduces to the classical Reynolds equation.

2.2.3 Numerical Solution

Equations (2.25) – (2.29) are discretized by using the central difference scheme. The discretized equations are expressed as follows:

$$\bar{p}_{i,j} = \frac{A_{i,j}\bar{p}_{i+1,j} + B_{i,j}\bar{p}_{i-1,j} + C_{i,j}\bar{p}_{i,j+1} + D_{i,j}\bar{p}_{i,j-1} - E_{i,j} + F_{i,j}}{G_{i,j}} \quad (2.30)$$

where

$$A_{i,j} = \left\{ \frac{\bar{h}_{i,j}^3}{(\Delta\theta_1)^2} + \frac{3\bar{h}_{i,j}^2}{2\Delta\theta_1} \left(\frac{\bar{h}_{i+1,j} - \bar{h}_{i-1,j}}{2\Delta\theta_1} \right) \right\} \quad (2.30a)$$

$$B_{i,j} = \left\{ \frac{\bar{h}_{i,j}^3}{(\Delta\theta_1)^2} - \frac{3\bar{h}_{i,j}^2}{2\Delta\theta_1} \left(\frac{\bar{h}_{i+1,j} - \bar{h}_{i-1,j}}{2\Delta\theta_1} \right) \right\} \quad (2.30b)$$

$$C_{i,j} = \left\{ \frac{\bar{h}_{i,j}^3}{(\Delta\bar{z}_1)^2} + \frac{3\bar{h}_{i,j}^2}{2\Delta\bar{z}_1} \left(\frac{\bar{h}_{i,j+1} - \bar{h}_{i,j-1}}{2\Delta\bar{z}_1} \right) \right\} \quad (2.30c)$$

$$D_{i,j} = \left\{ \frac{\bar{h}_{i,j}^3}{(\Delta\bar{z}_1)^2} - \frac{3\bar{h}_{i,j}^2}{2\Delta\bar{z}_1} \left(\frac{\bar{h}_{i,j+1} - \bar{h}_{i,j-1}}{2\Delta\bar{z}_1} \right) \right\} \quad (2.30d)$$

$$E_{i,j} = \left\{ \frac{1}{\delta^2} \left(\frac{\bar{h}_{i+1,j} - \bar{h}_{i-1,j}}{2\Delta\theta_1} \right) \right\} \quad (2.30e)$$

$$F_{i,j} = \left[\frac{Re^*}{3\delta^2} \left\{ \frac{(\bar{h}I_{\theta_1})_{i+1,j} - (\bar{h}I_{\theta_1})_{i-1,j}}{2\Delta\theta_1} + \frac{(\bar{h}I_{\bar{z}_1})_{i,j+1} - (\bar{h}I_{\bar{z}_1})_{i,j-1}}{2\Delta\bar{z}_1} \right\} \right] \quad (2.30f)$$

$$G_{i,j} = \left\{ \frac{\bar{h}_{i,j}^3}{(\Delta\theta_1)^2} + \frac{\bar{h}_{i,j}^3}{(\Delta\bar{z}_1)^2} \right\} \quad (2.30g)$$

$$(Q_{\theta})_{i,j} = \left\{ 3\delta^2 \bar{h}_{i,j}^2 \left(\frac{\bar{p}_{1,i+1,j} - \bar{p}_{1,i-1,j}}{2\Delta\theta_1} \right) + Re^*(I_{\theta})_{i,j} \right\} \quad (2.31)$$

$$(Q_{\bar{z}})_{i,j} = \left\{ 3\delta^2 \bar{h}_{i,j}^2 \left(\frac{\bar{p}_{1,i,j+1} - \bar{p}_{1,i,j-1}}{2\Delta\bar{z}} \right) + Re^*(I_{\bar{z}})_{i,j} \right\} \quad (2.32)$$

$$(I_{\theta})_{i,j} = \frac{\bar{R}\bar{h}_{i,j}}{2} \left[-\frac{1}{2} \left\{ \frac{4}{3} \left(\frac{\bar{h}_{i+1,j} - \bar{h}_{i-1,j}}{2\Delta\theta_1} \right) + \frac{\bar{h}_{i,j}}{6} \frac{(Q_{\bar{z}})_{i,j+1} - (Q_{\bar{z}})_{i,j-1}}{2\Delta\bar{z}_1} \right\} \right. \\ \left. - \frac{(Q_{\theta})_{i,j}}{6} \left(\left(\frac{\bar{h}_{i+1,j} - \bar{h}_{i-1,j}}{2\Delta\theta_1} \right) - \frac{\bar{h}_{i,j}}{5} \frac{(Q_{\bar{z}})_{i,j+1} - (Q_{\bar{z}})_{i,j-1}}{2\Delta\bar{z}_1} \right) \right. \\ \left. - \frac{\bar{h}_{i,j}}{6} \left(\frac{(Q_{\theta})_{i+1,j} - (Q_{\theta})_{i-1,j}}{2\Delta\theta_1} - \frac{(Q_{\bar{z}})_{i,j}}{5} \frac{(Q_{\theta})_{i,j+1} - (Q_{\theta})_{i,j-1}}{2\Delta\bar{z}_1} \right) \right. \\ \left. + \frac{(Q_{\theta})_{i,j}}{15} \left[\frac{\bar{h}_{i,j}}{\bar{h}_{i,j}} \frac{(Q_{\theta})_{i+1,j} - (Q_{\theta})_{i-1,j}}{2\Delta\theta_1} + \frac{(Q_{\theta})_{i,j}}{2} \left(\frac{\bar{h}_{i+1,j} - \bar{h}_{i-1,j}}{2\Delta\theta_1} \right) \right. \right. \\ \left. \left. + \left(-\frac{(Q_{\bar{z}})_{i,j}}{12} + \frac{(Q_{\theta})_{i,j} (Q_{\bar{z}})_{i,j}}{30} \right) \left(\frac{\bar{h}_{i,j+1} - \bar{h}_{i,j-1}}{2\Delta\bar{z}_1} \right) \right] \right] \quad (2.33)$$

$$(I_{\bar{z}})_{i,j} = \frac{\bar{R}\bar{h}_{i,j}}{2} \left[-\frac{(Q_{\bar{z}})_{i,j}}{6} \left\{ \frac{1}{2} \frac{\bar{h}_{i+1,j} - \bar{h}_{i-1,j}}{2\Delta\theta_1} - \frac{(Q_{\theta})_{i,j}}{5} \frac{\bar{h}_{i+1,j} - \bar{h}_{i-1,j}}{2\Delta\theta_1} \right\} \right. \\ \left. - \frac{\bar{h}_{i,j}}{6} \left\{ \frac{1}{2} \frac{(Q_{\bar{z}})_{i+1,j} - (Q_{\bar{z}})_{i-1,j}}{2\Delta\theta_1} - \frac{(Q_{\bar{z}})_{i,j}}{5} \frac{(Q_{\theta})_{i+1,j} - (Q_{\theta})_{i-1,j}}{2\Delta\theta_1} \right\} \right. \\ \left. + \frac{\bar{h}_{i,j}}{15} \left[\frac{(Q_{\theta})_{i,j}}{2} \frac{(Q_{\bar{z}})_{i+1,j} - (Q_{\bar{z}})_{i-1,j}}{2\Delta\theta_1} + (Q_{\bar{z}})_{i,j} \frac{(Q_{\bar{z}})_{i,j+1} - (Q_{\bar{z}})_{i,j-1}}{2\Delta\bar{z}_1} \right. \right. \\ \left. \left. + \frac{(Q_{\bar{z}})_{i,j}^2}{30} \frac{\bar{h}_{i,j+1} - \bar{h}_{i,j-1}}{2\Delta\bar{z}_1} \right] \right] \quad (2.34)$$

The Equation (2.25) is solved by the Gauss-Seidel method with successive over-relaxation (SOR) to find the pressure distribution inside the bearing. Due to convergence

issues, it is difficult to directly solve the governing equation with lubricant inertia effect. In view of this, the pressure developed inside the bearing is initially estimated by solving the modified Reynolds equation for $Re^* = 0.0$. The resulting pressure values are then used to estimate the flow parameters (Q_{θ_1} and $Q_{\bar{z}_1}$) and the integrating factors (I_{θ_1} and $I_{\bar{z}_1}$) for $Re^* = 0.0$. These values are then used as input and Equation (2.25) is solved for finite values of Re^* . This process continues until all the values fulfil the desired convergence criteria. The convergence criterion for pressure is $\left|1 - \left(\frac{\sum \bar{p}_{new}}{\sum \bar{p}_{old}}\right)\right| \leq \zeta$, where ζ is decreased from 10^{-3} to 10^{-5} as the mesh is progressively densified.

2.2.4 Performance Characteristics

Once the pressure distribution is estimated, the non-dimensional load-carrying capacity, the Sommerfeld number, attitude angle, non-dimensional flow coefficient, and friction variable can be estimated using Simpson's 1/3rd rule of numerical integration method, as shown in the following equations. The solution scheme discussed here is depicted as a flowchart in Fig. 2.4.

$$\left. \begin{aligned} \bar{F}_\varepsilon &= -2\bar{R} \int_0^1 \int_0^{2\pi} \bar{p}_1 \cos \theta d\theta d\bar{z} \\ \bar{F}_\phi &= 2\bar{R} \int_0^1 \int_0^{2\pi} \bar{p}_1 \sin \theta d\theta d\bar{z} \\ \bar{W} &= \sqrt{\bar{F}_\varepsilon^2 + \bar{F}_\phi^2} \end{aligned} \right\} \quad (2.35)$$

$$\phi = \tan^{-1} \left(\frac{\bar{F}_\phi}{\bar{F}_\varepsilon} \right) \quad (2.36)$$

$$S = \frac{\bar{L}}{6\pi\bar{W}} \left(\frac{\bar{R}}{\delta} \right)^2 \quad (2.37)$$

$$\bar{q}_z = -\frac{2\delta^2}{D} \int_0^{2\pi} \bar{h}^3 \frac{\partial \bar{p}_1}{\partial \bar{z}} d\theta \quad (2.38)$$

$$\mu = \frac{2 \int_0^{2\pi} \left(3\delta^2 \bar{h}^2 \frac{\partial \bar{p}_1}{\partial \theta} + \frac{1}{h} \right) d\theta}{D\bar{W}} \quad (2.39)$$

It is worthwhile to mention that In this study, an inverse method has been followed for the analysis of the journal bearing, in which the eccentricity ratio (ε) is employed as a non-dimensional parameter to enable a generalized investigation across various operating conditions and bearing geometries.

By solving the non-dimensional Reynolds equation for a specified value of ε , the corresponding Sommerfeld number can be estimated.

The Sommerfeld number is a dimensionless parameter that depends on the applied load, rotational speed, bearing geometry, and lubricant properties. Therefore, once the Sommerfeld number is determined for a given eccentricity ratio, the actual load can be estimated if the speed, lubricant viscosity, and bearing dimensions are known.

For example, referring to the standard results presented on Table 3.1 in section 3.3 of this these, for a bearing with $L/D=1$, for $\varepsilon=0.2$, the Sommerfeld number, $S=0.632$.

We have

$$S = \frac{\eta N}{p} \left(\frac{R}{C} \right)^2$$

$$\text{or } S = \frac{\eta N}{\left(\frac{W}{LD} \right)} \left(\frac{R}{C} \right)^2$$

$$\text{or } \frac{W}{N} = \frac{\eta LD}{S} \left(\frac{R}{C} \right)^2$$

Now, considering a standard bearing with radius (R) = 50 mm, clearance (C) = 50 μm , and Viscosity (η) = 0.01 Pa.S

The Load to speed (W/N) ratio = 12500/79

Sl no	Speed	Load
1	50 rps	7911.3 MN
2	100 rps	15822.78 MN
3	150 rps	23734.18 MN

Sl no	Load	Speed
1	5000 MN	31.6 rps
2	10000 MN	63.2 rps
3	15000 MN	94.8 rps

Similarly, for $L/D = 1$, $\varepsilon = 0.3$, $S = 0.382$

The W/N ratio = 50000/191.

Sl no	Speed	Load
1	50 rps	13089.00 MN
2	100 rps	26178.01 MN
3	150 rps	39267.02 MN

Sl no	Load	Speed
1	5000 MN	19.1 rps
2	10000 MN	38.2 rps
3	15000 MN	57.3 rps

Therefore, from the W/N ratio, the load at different speed or speed at different load can be estimated for different eccentricity ratios.

This gives a comprehensive understanding of the relationship between the load and speed of journal bearing with the eccentricity ratio. Therefore, by solving the Reynolds equation for a specific value of eccentricity ratio, one can ascertain the corresponding load-carrying capacity or the required operating speed of the bearing for given geometric and lubricant conditions.

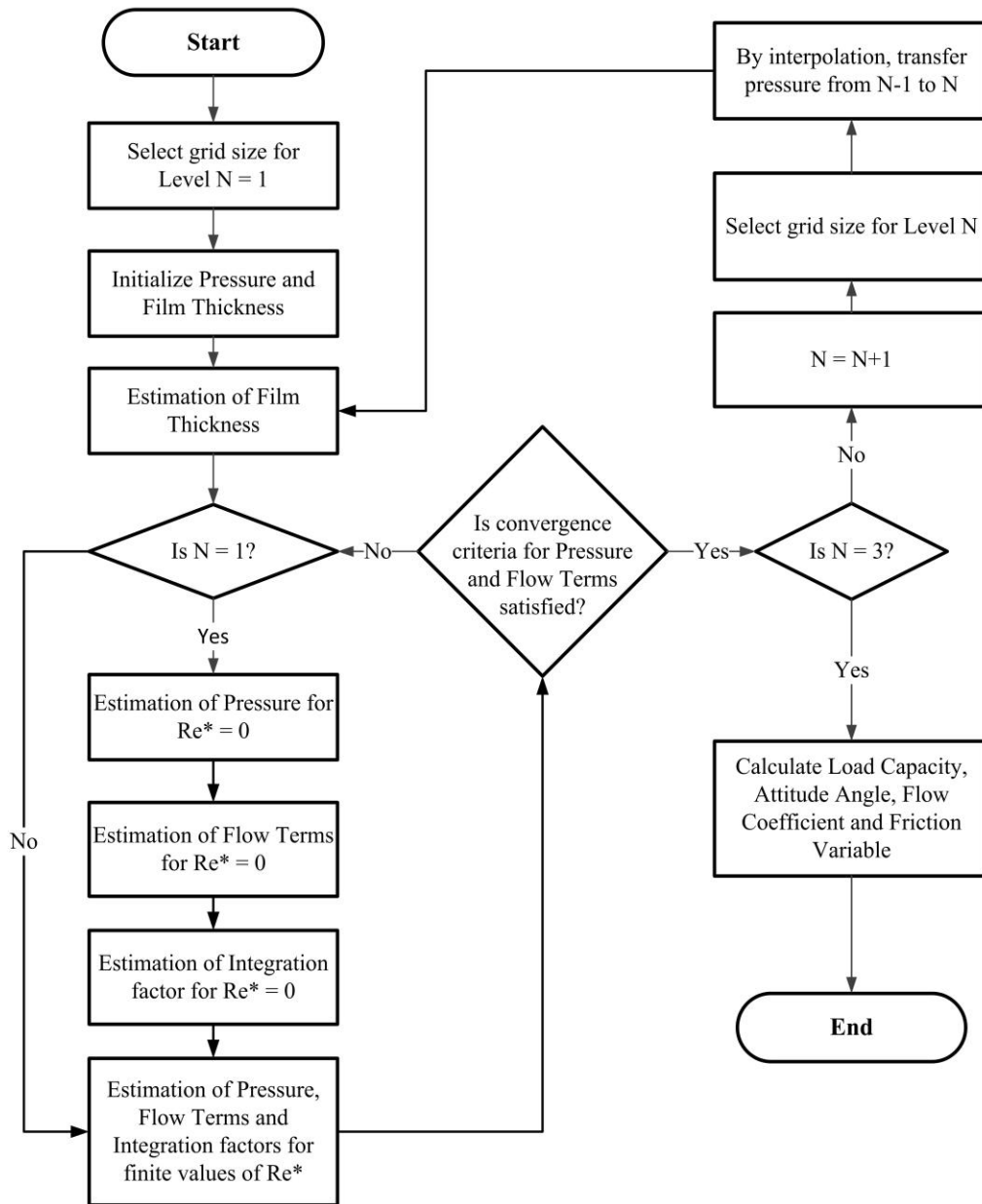


Fig. 2.4. Flowchart of solution procedure using Reynolds boundary conditions

2.2.5 Reynolds Boundary Conditions

The Reynolds boundary conditions used for the solution of the above equations are given as follows [112]:

$$\begin{aligned}\bar{p}_1(\theta, \pm 1) &= 0 \\ \bar{p}_1(0, \bar{z}) &= \bar{p}_1(2\pi, \bar{z}) \\ \frac{\partial \bar{p}_1}{\partial \bar{z}} &= 0 \text{ at } \bar{z} = 0 \\ \bar{p}_1 &= 0, \quad \partial \bar{p}_1 / \partial \theta = 0 \text{ at } \theta = \theta_c\end{aligned}\tag{2.40}$$

Here θ_c is the angle where the film cavitates. The fourth condition of the boundary conditions given in Equation (2.40) refers to this location which is not known a-priori. In an iterative solution scheme of the governing equations, the negative pressure at every iteration is taken as 0, which satisfies the cavitation condition which was originally demonstrated by Christopherson [11] in 1942.

2.2.6 Stability Analysis of Textured Journal Bearing

For stability analysis, a time transient analysis is carried out by solving the following non-dimensional equations of motions:

$$\bar{M}\ddot{x} = \bar{F}_x + \bar{W}_0\tag{2.41}$$

$$\bar{M}\ddot{y} = \bar{F}_y\tag{2.42}$$

where,

$$\bar{F}_x = \bar{F}_\varepsilon \cos \phi + \bar{F}_\phi \sin \phi\tag{2.43}$$

$$\bar{F}_y = \bar{F}_\varepsilon \sin \phi - \bar{F}_\phi \cos \phi\tag{2.44}$$

$$x = \varepsilon \cos \phi\tag{2.45}$$

$$y = \varepsilon \sin \phi\tag{2.46}$$

Substituting Equations (2.43), (2.44), (2.45) and (2.46) in Equations (2.41) and (2.42):

$$\bar{M}C\omega^2\ddot{\varepsilon} - \bar{M}C\omega^2\varepsilon\dot{\phi}^2 - \bar{F}_\varepsilon\bar{W}_0 \cos \phi = 0 \quad (2.47)$$

$$\bar{M}C\omega^2\varepsilon\ddot{\phi} + 2\bar{M}C\omega^2\varepsilon\dot{\phi} - \bar{F}_\phi + \bar{W}_0 \sin \phi = 0 \quad (2.48)$$

After simplifying Equations (2.47) and (2.48), the equations of motion are obtained in the following form:

$$\ddot{\varepsilon} = \frac{\bar{F}_\varepsilon}{\bar{W}_0\bar{M}} + \frac{\cos \phi}{\bar{M}} + \varepsilon\dot{\phi}^2 \quad (2.49)$$

$$\ddot{\phi} = \frac{\bar{F}_\phi}{\bar{M}\bar{W}_0\varepsilon} - \frac{\sin \phi}{\bar{M}\varepsilon} - \frac{2\varepsilon\dot{\phi}}{\varepsilon} \quad (2.50)$$

Equations (2.49) and (2.50) are numerically solved using 4th order Runge-Kutta method to estimate the time-dependent values of the eccentricity ratio (ε), attitude angle (ϕ), and their time derivatives ($\dot{\varepsilon}$ and $\dot{\phi}$). During the computation, the non-dimensional steady-state load (\bar{W}_0) corresponding to the initial eccentricity ratio is assumed to remain constant. For a particular value of mass-parameter (\bar{M}), a function of speed, the trajectory of the journal centre is obtained by plotting the attitude angle against the eccentricity ratio at each time step. This trajectory effectively captures the dynamic behaviour of the journal over time. By analyzing such trajectory, the stability of the rotor can be assessed, allowing classification into stable, unstable, or critically stable operating conditions.

In addition to the mass-parameters, the whirl ratio of the rotor can be estimated from the FFT-spectrum of the horizontal and vertical displacement of the rotor. The whirl ratio ($\bar{\omega}$) is defined by the ratio of whirling speed of the rotor to the rotor spin speed. The flowchart of the described solution process is depicted in Fig. 2.5.

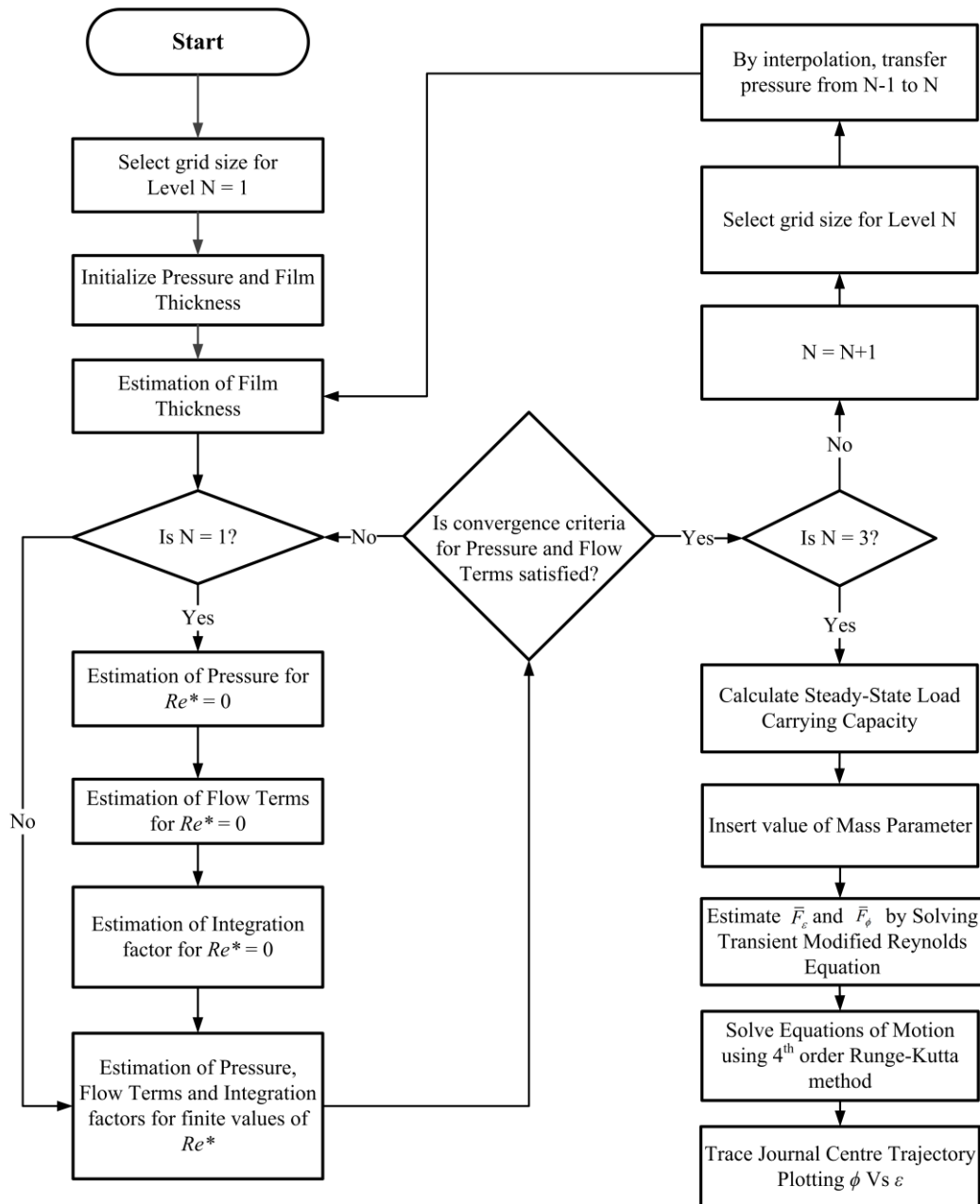


Fig. 2.5. Flowchart for Stability Analysis of Textured Journal Bearing

2.3 Theory for Textured Journal Bearing with Lubricant Inertia Effect using Mass-Conserving (JFO) Boundary Conditions

2.3.1 Governing Equation

The published literature does not provide a governing equation incorporating the fluid inertia effect using the JFO boundary conditions. Therefore, a derivation leading to the governing equation is presented here.

The derivation involves consideration of certain basic assumptions, which were mentioned in section 2.2.1. The non-dimensional Navier-Stokes equations, after the applications of the basic assumptions, are given by Equations (2.9) and (2.10). The continuity equation in the dimensional form is given by Equation (2.5). Equation (2.5) in non-dimensional form can be written as:

$$\frac{\partial(\theta_D)}{\partial\tau} + \frac{\partial(\bar{u}\theta_D)}{\partial\theta} + \frac{\partial(\bar{v}\theta_D)}{\partial\bar{y}} + \left(\frac{D}{L}\right)\frac{\partial(\bar{w}\theta_D)}{\partial\bar{z}} = 0 \quad (2.51)$$

where, $\theta_D = \rho/\rho_c$, is the fractional film content introduced by Elrod [5]. The introduction of the fractional film content enables the formulation of a universal modified Reynolds equation that accounts for both cavitated and full film regions.

The full film pressure due to cavitation can be determined using Equation (2.52) [97]:

$$\bar{p} = \bar{p}_c + \bar{\beta} \ln \theta_D \quad (2.52)$$

Using parabolic velocity profiles from Equations (2.13) and (2.14), which are feasible in the case of laminar flow, the flow terms, Q_θ and $Q_{\bar{z}}$, are obtained by integrating the momentum Equations (2.9) and (2.10).

$$Q_\theta = \frac{\bar{h}^2}{2} \frac{\bar{g}\bar{\beta}}{\theta_D} \frac{\partial\theta_D}{\partial\theta} + Re^* I_\theta \quad (2.53)$$

$$Q_{\bar{z}} = \left(\frac{D}{L}\right) \frac{\bar{h}^2}{2} \frac{\bar{g}\bar{\beta}}{\theta_D} \frac{\partial \theta_D}{\partial \bar{z}} + Re^* I_{\bar{z}} \quad (2.54)$$

In Equations (2.53) and (2.54) the pressure derivative terms are substituted in terms of the derivatives of the fractional film content (θ_D), using Equation (2.52).

where, the terms I_θ and $I_{\bar{z}}$ are given as follows:

$$I_\theta = \frac{\bar{h}}{2} \left[\frac{4}{3} \frac{\partial \bar{h}}{\partial \theta} + \frac{3}{2} \frac{\partial \bar{h}}{\partial \tau} + \left(\frac{D}{L}\right) \frac{\bar{h}}{6} \frac{\partial Q_{\bar{z}}}{\partial \bar{z}} - \frac{Q_\theta}{6} \left(\frac{\partial \bar{h}}{\partial \tau} + \frac{\partial \bar{h}}{\partial \theta} - \left(\frac{D}{L}\right) \frac{\bar{h}}{5} \frac{\partial Q_{\bar{z}}}{\partial \bar{z}} \right) - \frac{\bar{h}}{6} \left(\frac{\partial Q_\theta}{\partial \tau} + \frac{\partial Q_\theta}{\partial \theta} - \left(\frac{D}{L}\right) \frac{Q_{\bar{z}}}{5} \frac{\partial Q_\theta}{\partial \bar{z}} \right) + \frac{Q_\theta}{15} \left(\frac{\partial Q_\theta}{\partial \theta} + \frac{Q_\theta}{2} \frac{\partial \bar{h}}{\partial \theta} \right) - \left(\frac{D}{L}\right) \frac{Q_{\bar{z}}}{6} \left(\frac{1}{2} \frac{\partial \bar{h}}{\partial \bar{z}} - \frac{Q_\theta}{5} \frac{\partial \bar{h}}{\partial \bar{z}} \right) \right] \quad (2.55)$$

$$I_{\bar{z}} = \frac{\bar{h}}{2} \left[\left(\frac{D}{L}\right) \frac{Q_{\bar{z}}^2}{30} \frac{\partial \bar{h}}{\partial \bar{z}} - \frac{\bar{h}}{6} \left(\frac{1}{2} \frac{\partial Q_{\bar{z}}}{\partial \theta} - \frac{Q_{\bar{z}}}{5} \frac{\partial Q_\theta}{\partial \theta} + \frac{\partial Q_{\bar{z}}}{\partial \tau} \right) + \frac{\bar{h}}{15} \left(Q_\theta \frac{\partial Q_{\bar{z}}}{\partial \theta} + Q_{\bar{z}} \left(\frac{D}{L} \right) \frac{\partial Q_{\bar{z}}}{\partial \bar{z}} \right) - \frac{Q_{\bar{z}}}{6} \left(\frac{1}{2} \frac{\partial \bar{h}}{\partial \theta} - \frac{Q_\theta}{5} \frac{\partial \bar{h}}{\partial \theta} + \frac{\partial \bar{h}}{\partial \tau} \right) \right] \quad (2.56)$$

Integration of the non-dimensional continuity Equation (2.51) yields a Novel Modified Reynolds equation that simultaneously incorporates the effects of lubricant inertia and cavitation effect, as expressed in Equation (2.57).

$$\frac{\partial}{\partial \theta} \left(\bar{g}\bar{\beta}\bar{h}^3 \frac{\partial \theta_D}{\partial \theta} \right) + \left(\frac{D}{L}\right)^2 \frac{\partial}{\partial \bar{z}} \left(\bar{g}\bar{\beta}\bar{h}^3 \frac{\partial \theta_D}{\partial \bar{z}} \right) = 12\bar{V}_C - 6 \frac{\partial(\bar{h}\theta_D)}{\partial \theta} - 2Re^* \left\{ \frac{\partial(\bar{h}I_\theta)}{\partial \theta} + \left(\frac{D}{L}\right) \frac{\partial(\bar{h}I_{\bar{z}})}{\partial \bar{z}} \right\} \quad (2.57)$$

where, \bar{g} is the switch function proposed by Elrod [5], and it is defined as follows:

$$\bar{g} = \begin{cases} 0 & \theta_D < 1 \\ 1 & \theta_D \geq 1 \end{cases} \quad (2.58)$$

$$\bar{V}_C = \frac{\partial \bar{h}}{\partial \theta} + \frac{\partial \varepsilon}{\partial \tau} \cos \theta + \varepsilon \frac{\partial \theta}{\partial \tau} \sin \theta \quad (2.59)$$

The above equations for steady-state condition is given as follows

$$\frac{\partial}{\partial \theta} \left(\bar{g} \bar{\beta} \bar{h}^3 \frac{\partial \theta_D}{\partial \theta} \right) + \left(\frac{D}{L} \right)^2 \frac{\partial}{\partial \bar{z}} \left(\bar{g} \bar{\beta} \bar{h}^3 \frac{\partial \theta_D}{\partial \bar{z}} \right) = 6 \frac{\partial (\bar{h} \theta_D)}{\partial \theta} - 2Re^* \left\{ \frac{\partial (\bar{h} I_\theta \theta_D)}{\partial \theta} + \left(\frac{D}{L} \right) \frac{\partial (\bar{h} I_{\bar{z}} \theta_D)}{\partial \bar{z}} \right\} \quad (2.60)$$

$$I_\theta = \frac{\bar{h}}{2} \left[\frac{4}{3} \frac{\partial \bar{h}}{\partial \theta} + \left(\frac{D}{L} \right) \frac{\bar{h}}{6} \frac{\partial Q_{\bar{z}}}{\partial \bar{z}} - \frac{Q_\theta}{6} \left(\frac{\partial \bar{h}}{\partial \theta} - \left(\frac{D}{L} \right) \frac{\bar{h}}{5} \frac{\partial Q_{\bar{z}}}{\partial \bar{z}} \right) - \frac{\bar{h}}{6} \left(\frac{\partial Q_\theta}{\partial \theta} \right. \right. \\ \left. \left. - \left(\frac{D}{L} \right) \frac{Q_{\bar{z}}}{5} \frac{\partial Q_\theta}{\partial \bar{z}} \right) + \frac{Q_\theta}{15} \left(\frac{\partial Q_\theta}{\partial \theta} + \frac{Q_\theta}{2} \frac{\partial \bar{h}}{\partial \theta} \right) - \left(\frac{D}{L} \right) \frac{Q_{\bar{z}}}{6} \left(\frac{1}{2} \frac{\partial \bar{h}}{\partial \bar{z}} - \frac{Q_\theta}{5} \frac{\partial \bar{h}}{\partial \bar{z}} \right) \right] \quad (2.61)$$

$$I_{\bar{z}} = \frac{\bar{h}}{2} \left[\left(\frac{D}{L} \right) \frac{Q_{\bar{z}}^2}{30} \frac{\partial \bar{h}}{\partial \bar{z}} - \frac{\bar{h}}{6} \left(\frac{1}{2} \frac{\partial Q_{\bar{z}}}{\partial \theta} - \frac{Q_{\bar{z}}}{5} \frac{\partial Q_\theta}{\partial \theta} \right) + \frac{\bar{h}}{15} \left(Q_\theta \frac{\partial Q_{\bar{z}}}{\partial \theta} \right. \right. \\ \left. \left. + Q_{\bar{z}} \left(\frac{D}{L} \right) \frac{\partial Q_{\bar{z}}}{\partial \bar{z}} \right) - \frac{Q_{\bar{z}}}{6} \left(\frac{1}{2} \frac{\partial \bar{h}}{\partial \theta} - \frac{Q_\theta}{5} \frac{\partial \bar{h}}{\partial \theta} \right) \right] \quad (2.62)$$

The second term on the right-hand side, in Equation (2.60), represents the lubricant inertia effect. In Equation (2.58) the switch function (\bar{g}) allows the equation to be accurate under the assumption of uniform pressure in the cavitated zone [97]. When the fractional film content (θ_D) is less than 1, the switch function (\bar{g}) assumes the value of 0. Therefore, the left-hand side of the Equation (2.60) vanishes, and the Equation (2.60) becomes valid for the cavitated region. When the fractional film content (θ_D) is more than or equal to 1, the switch function (\bar{g}) assumes the value of 1, thus the equation corresponds to the full film region in this case.

2.3.2 Numerical Solution

The Equations (2.53), (2.54), (2.60), (2.61) and (2.62) are discretized using the central difference method (CDM) and solved by the Gauss-Seidel method with relaxation and the progressive mesh densification (PMD) method. Initially, Equation (2.57) is solved by setting $Re^* = 0$, i.e., under inertia less condition, followed by the calculations of Q_θ , $Q_{\bar{z}}$, I_θ and $I_{\bar{z}}$ using Equations (2.53), (2.54), (2.61) and (2.62) respectively. It is important to highlight that the estimation of the above parameters using $Re^* = 0$ is done only once at the beginning of the iteration. These values, from the first iteration, are then used in the subsequent iteration, to solve Equations (2.53), (2.54), (2.60), (2.61) and (2.62), for finite

values of Re^* . The process continues until all the values fulfil the desired convergence criteria of $\left|1 - \left(\frac{\Sigma\theta_{D_{new}}}{\Sigma\theta_{D_{old}}}\right)\right| \leq \zeta$, where ζ is progressively decreased from 10^{-3} to 10^{-5} . The same convergence criteria have been applied to the calculations of Q_θ and $Q_{\bar{z}}$. The switch function algorithm has been implemented by following the work of Fesanghary and Khonsari [97]. Once the fractional film content is calculated, the pressure distribution inside the bearing can be estimated using the Equation (2.52). Fig. 2.6 shows a flowchart of the solution scheme described here. The discretized form of Equations (2.53), (2.54), (2.60), (2.61) and (2.62) are presented below:

$$Q_{\theta_{i,j}} = \frac{\bar{h}_{i,j}^2 \bar{g}_{i,j} \bar{\beta}}{2 \theta_{D_{i,j}}} \frac{\theta_{D_{i+1,j}} - \theta_{D_{i-1,j}}}{2\Delta\theta} + Re^* I_{\theta_{i,j}} \quad (2.63)$$

$$Q_{\bar{z}_{i,j}} = \left(\frac{D}{L}\right) \frac{\bar{h}_{i,j}^2 \bar{g}_{i,j} \bar{\beta}}{2 \theta_{D_{i,j}}} \frac{\theta_{D_{i,j+1}} - \theta_{D_{i,j-1}}}{2\Delta\bar{z}} + Re^* I_{\bar{z}_{i,j}} \quad (2.64)$$

$$I_{\theta_{i,j}} = \frac{\bar{h}_{i,j}}{2} \left[\frac{4}{3} \frac{\bar{h}_{i+1,j} - \bar{h}_{i-1,j}}{2\Delta\theta} + \left(\frac{D}{L}\right) \frac{\bar{h}_{i,j}}{6} \frac{Q_{\bar{z}_{i,j+1}} - Q_{\bar{z}_{i,j-1}}}{2\Delta\bar{z}} - \frac{Q_{\theta_{i,j}}}{6} \left(\frac{\bar{h}_{i+1,j} - \bar{h}_{i-1,j}}{2\Delta\theta} - \left(\frac{D}{L}\right) \frac{\bar{h}_{i,j}}{5} \frac{Q_{\bar{z}_{i,j+1}} - Q_{\bar{z}_{i,j-1}}}{2\Delta\bar{z}} \right) \right. \\ \left. - \frac{\bar{h}_{i,j}}{6} \left(\frac{Q_{\theta_{i+1,j}} - Q_{\theta_{i-1,j}}}{2\Delta\theta} - \left(\frac{D}{L}\right) \frac{Q_{\bar{z}_{i,j}}}{5} \frac{Q_{\theta_{i,j+1}} - Q_{\theta_{i,j-1}}}{2\Delta\bar{z}} \right) + \frac{Q_{\theta_{i,j}}}{15} \left(\frac{Q_{\theta_{i+1,j}} - Q_{\theta_{i-1,j}}}{2\Delta\theta} + \frac{Q_{\theta_{i,j}}}{2} \frac{\bar{h}_{i+1,j} - \bar{h}_{i-1,j}}{2\Delta\theta} \right) \right. \\ \left. \left(\frac{D}{L} \right) \frac{Q_{\bar{z}_{i,j}}}{6} \left(\frac{1}{2} \frac{\bar{h}_{i,j+1} - \bar{h}_{i,j-1}}{2\Delta\bar{z}} - \frac{Q_{\theta_{i,j}}}{5} \frac{\bar{h}_{i,j+1} - \bar{h}_{i,j-1}}{2\Delta\bar{z}} \right) \right] \quad (2.65)$$

$$I_{\bar{z}_{i,j}} = \frac{\bar{h}_{i,j}}{2} \left[\left(\frac{D}{L}\right) \frac{Q_{\bar{z}_{i,j}}^2}{30} \frac{\bar{h}_{i,j+1} - \bar{h}_{i,j-1}}{2\Delta\bar{z}} - \frac{\bar{h}_{i,j}}{6} \left(\frac{1}{2} \frac{Q_{\bar{z}_{i,j+1}} - Q_{\bar{z}_{i,j-1}}}{2\Delta\theta} - \frac{Q_{\bar{z}_{i,j}}}{5} \frac{Q_{\theta_{i,j+1}} - Q_{\theta_{i,j-1}}}{2\Delta\bar{z}} \right) + \frac{\bar{h}_{i,j}}{15} \left(Q_{\theta_{i,j}} \frac{Q_{\bar{z}_{i+1,j}} - Q_{\bar{z}_{i-1,j}}}{2\Delta\theta} \right. \right. \\ \left. \left. Q_{\bar{z}_{i,j}} \left(\frac{D}{L} \right) \frac{Q_{\bar{z}_{i,j+1}} - Q_{\bar{z}_{i,j-1}}}{2\Delta\bar{z}} \right) - \frac{Q_{\bar{z}_{i,j}}}{6} \left(\frac{1}{2} \frac{\bar{h}_{i+1,j} - \bar{h}_{i-1,j}}{2\Delta\theta} - \frac{Q_{\theta_{i,j}}}{5} \frac{\bar{h}_{i+1,j} - \bar{h}_{i-1,j}}{2\Delta\theta} \right) \right] \quad (2.66)$$

$$\begin{aligned}
 & \left[\frac{6}{\Delta\theta} (1-g_{i-1,j}) h_{i-1,j} + \frac{\bar{\beta}}{\Delta\theta^2} (g_{i-1,j}) (\bar{h}_{i-1/2,j})^3 - \frac{2Re^*}{\Delta\theta} (\bar{h}I_\theta)_{i-1,j} (1-g_{i-1,j}) \right] \theta_{D_{i-1,j}} \\
 & + \left[\frac{\beta}{\Delta\theta^2} (g_{i+1,j}) (\bar{h}_{i+1/2,j})^3 \right] \theta_{D_{i+1,j}} + \left[\left(\frac{D}{L} \right)^2 \frac{\beta}{\Delta\bar{z}^2} (g_{i,j+1}) (\bar{h}_{i,j+1/2})^3 \right] \theta_{D_{i,j+1}} \\
 & + \left[\left(\frac{D}{L} \right)^2 \frac{\beta}{\Delta\bar{z}^2} (g_{i,j-1}) (\bar{h}_{i,j-1/2})^3 - \frac{2Re^*}{\Delta\bar{z}} \left(\frac{D}{L} \right) (\bar{h}I_{\bar{z}})_{i,j-1} (1-g_{i,j-1}) \right] \theta_{D_{i,j-1}} \\
 & + \left[\frac{6}{\Delta\theta} (g_{i,j}-1) h_{i,j} - \frac{\bar{\beta}}{\Delta\theta^2} (g_{i,j}) \left((\bar{h}_{i-1/2,j})^3 + (\bar{h}_{i+1/2,j})^3 \right) - \left(\frac{D}{L} \right)^2 \frac{\beta}{\Delta\bar{z}^2} (g_{i,j}) \left((\bar{h}_{i,j+1/2})^3 + (\bar{h}_{i,j-1/2})^3 \right) \right] \\
 & + \frac{2Re^*}{\Delta\theta} (\bar{h}I_\theta)_{i,j} (1-g_{i,j}) + \frac{2Re^*}{\Delta\bar{z}} \left(\frac{D}{L} \right) (\bar{h}I_{\bar{z}})_{i,j} (1-g_{i,j}) \theta_{D_{i,j}} \\
 & + \frac{6}{\Delta\theta} \left[\frac{(g_{i-1,j})(\bar{h}_{i-1,j})(2-g_{i,j})}{2} + \frac{(g_{i,j})(\bar{h}_{i,j})(g_{i-1,j}-2+g_{i+1,j})}{2} - \frac{(g_{i+1,j})(\bar{h}_{i+1,j})(g_{i,j})}{2} \right] \\
 & - \frac{2Re^*}{\Delta\theta} \left[\frac{(g_{i-1,j})(\bar{h}I_\theta)_{i-1,j}(2-g_{i,j})}{2} + \frac{(g_{i,j})(\bar{h}I_\theta)_{i,j}(g_{i-1,j}-2+g_{i+1,j})}{2} - \frac{(g_{i+1,j})(\bar{h}I_\theta)_{i+1,j}(g_{i,j})}{2} \right] \\
 & - \frac{2Re^*}{\Delta\bar{z}} \left(\frac{D}{L} \right) \left[\frac{(g_{i,j-1})(\bar{h}I_{\bar{z}})_{i,j-1}(2-g_{i,j})}{2} + \frac{(g_{i,j})(\bar{h}I_{\bar{z}})_{i,j}(g_{i,j-1}-2+g_{i,j+1})}{2} - \frac{(g_{i,j+1})(\bar{h}I_{\bar{z}})_{i,j+1}(g_{i,j})}{2} \right] \\
 & + \frac{\bar{\beta}}{\Delta\theta^2} \left[(g_{i,j}) \left((\bar{h}_{i-1/2,j})^3 + (\bar{h}_{i+1/2,j})^3 \right) - (g_{i-1,j}) (\bar{h}_{i-1/2,j})^3 - (g_{i+1,j}) (\bar{h}_{i+1/2,j})^3 \right] \\
 & + \left(\frac{D}{L} \right)^2 \frac{\beta}{\Delta\bar{z}^2} \left[(g_{i,j}) \left((\bar{h}_{i,j+1/2})^3 + (\bar{h}_{i,j-1/2})^3 \right) - (g_{i,j-1}) (\bar{h}_{i,j-1/2})^3 - (g_{i,j+1}) (\bar{h}_{i,j+1/2})^3 \right] = 0
 \end{aligned} \tag{2.67}$$

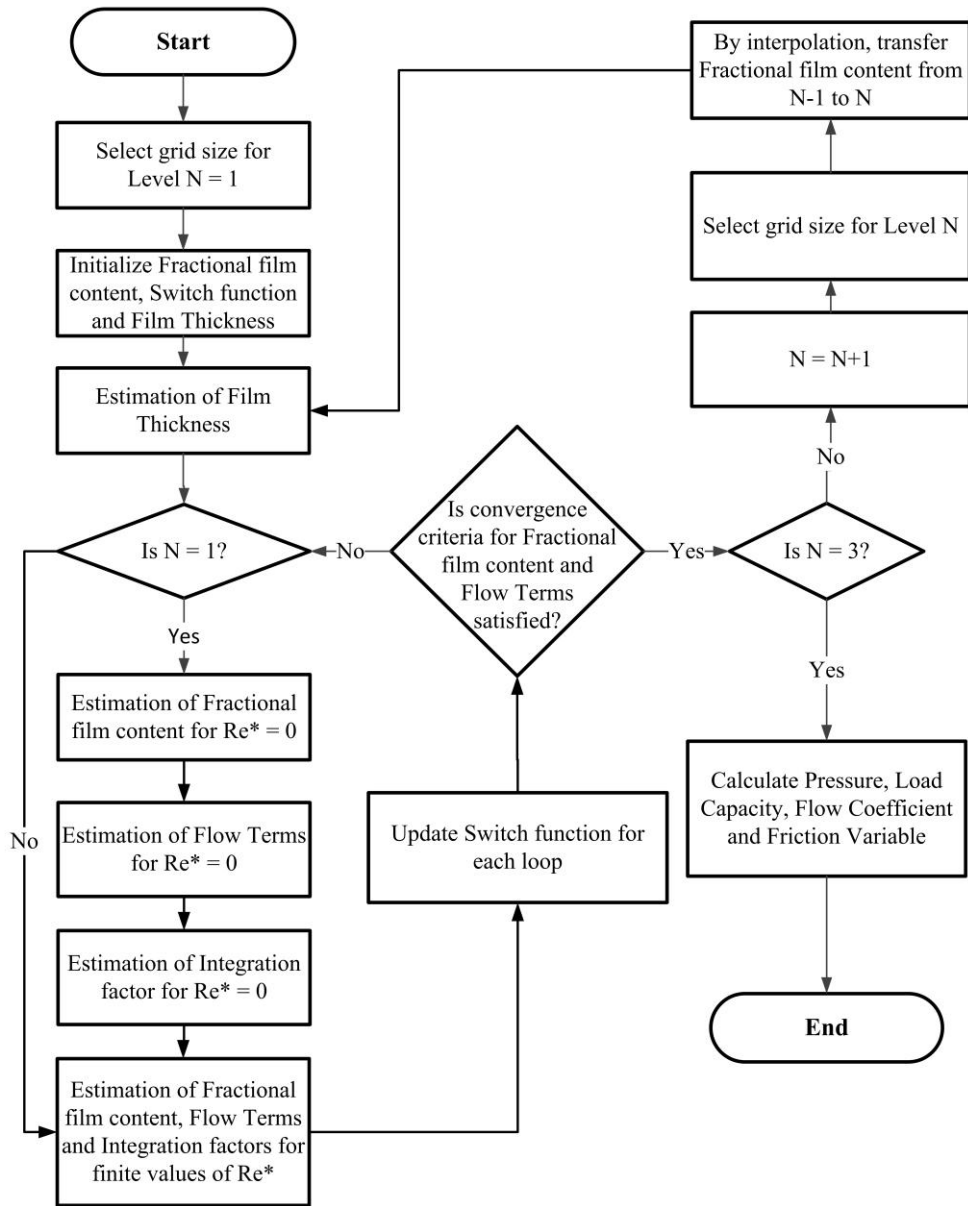


Fig. 2.6. Flowchart of the solution procedure using JFO boundary conditions

2.3.3 Performance Characteristics

The bearing performance parameters, viz., the non-dimensional load carrying capacity, the non-dimensional flow coefficient and the friction variable, are calculated as follows [102] using Simpson's 1/3rd rule of numerical integration.

$$\left. \begin{aligned} \bar{W}_\theta &= -\int_0^1 \int_0^{2\pi} \bar{p} \cos \theta d\theta d\bar{z} \\ \bar{W}_z &= \int_0^1 \int_0^{2\pi} \bar{p} \sin \theta d\theta d\bar{z} \\ \bar{W} &= \sqrt{(\bar{W}_\theta)^2 + (\bar{W}_z)^2} \end{aligned} \right\} \quad (2.68)$$

$$\bar{q}_z = -\frac{1}{3} \int_0^{2\pi} \frac{\bar{h}^3}{2} \left(\frac{D}{L} \right) \frac{\partial \bar{p}}{\partial \bar{z}} d\theta \quad (2.69)$$

$$\mu = \frac{1}{\bar{W}} \int_0^1 \int_0^{2\pi} \left(\frac{\bar{h}^2}{2} \frac{\partial \bar{p}}{\partial \theta} + \frac{1}{h} \right) d\theta d\bar{z} \quad (2.70)$$

2.4 Fluid Film Thickness

The space between the journal and the bearing is filled with lubricant having a thickness of h . The film thickness, h_0 , is a function of θ only in the case of plain journal bearing and is given by:

$$h_0 = 1 + \varepsilon \cos \theta \quad (2.71)$$

In the case of textured journal bearing, the film thickness, $h(\theta, \bar{z})$, is a function of both θ and \bar{z} . It is given as follows (refer to Fig. 2.2):

$$\bar{h}(\theta, z) = \begin{cases} h_0 \pm \bar{h}_p & \text{when } \bar{x}_1^2 + \bar{z}_1^2 \leq 1 \\ h_0 & \text{when } \bar{x}_1^2 + \bar{z}_1^2 > 1 \end{cases} \quad (2.72)$$

In Equation (2.72), the negative sign of \bar{h}_p corresponds to protrusion texturing, and the positive sign of \bar{h}_p corresponds to dimple texturing. For spherical, cylindrical and square texturing \bar{h}_p is given by Equations (2.73), (2.74) and (2.75) respectively.

$$\bar{h}_p = \begin{cases} -\left(\frac{1}{8\psi\delta} - \frac{\psi}{2\delta}\right) + \sqrt{\left(\frac{1}{8\psi\delta} + \frac{\psi}{2\delta}\right)^2 - \frac{1}{4\delta^2}\left((\bar{x}_1)^2 + (\bar{z}_1)^2\right)} & \text{when } \bar{x}_1^2 + \bar{z}_1^2 \leq 1 \\ 0 & \text{when } \bar{x}_1^2 + \bar{z}_1^2 > 1 \end{cases} \quad (2.73)$$

$$\bar{h}_p = \begin{cases} \psi & \text{when } \bar{x}_1^2 + \bar{z}_1^2 \leq 1 \\ 0 & \text{when } \bar{x}_1^2 + \bar{z}_1^2 > 1 \end{cases} \quad (2.74)$$

$$\bar{h}_p = \begin{cases} \psi & \text{when } |\bar{x}_1| + |\bar{z}_1| \leq 1 \\ 0 & \text{when } |\bar{x}_1| + |\bar{z}_1| > 1 \end{cases} \quad (2.75)$$

2.5 Progressive Mesh Densification

The progressive mesh densification (PMD) method [113] is a unidirectional mesh densification procedure where the mesh is progressively densified from coarse to the proposed highest mesh density. The errors at low frequencies are rectified at the initial stage, followed by those at intermediate and high frequencies. Thus, this iterative process swiftly achieves an initial approximation of the solution, which gradually converges towards its ultimate target in a unidirectional manner. Given that most iterations focus on low-level meshes, the overall solution procedure can proceed rapidly. Each time the mesh is densified, the nodal values of fractional film content (θ_D) are transferred through Lagrange interpolation [111]. The Lagrange interpolation formula for the fractional film content (θ_D) from Level N-1 to Level N is as follows:

$$\left[\theta_{D_{i,j}} \right]_N = \left[\left(\frac{\theta_{i,j} - \theta_{i+1,j}}{\theta_{i-1,j} - \theta_{i+1,j}} \right) \theta_{D_{i-1,j}} + \left(\frac{\theta_{i,j} - \theta_{i-1,j}}{\theta_{i+1,j} - \theta_{i-1,j}} \right) \theta_{D_{i+1,j}} \right]_{N-1} \quad (2.76)$$

To implement the PMD method in the solution, in the first level a coarse mesh of size $m \times n$ is selected corresponding to the loose convergence criterion of $\zeta = 10^{-3}$. Once converged, the mesh is densified in the next level by doubling the mesh size to $2m \times 2n$. The fractional film content values are interpolated to the new mesh using Lagrange interpolation [Equation (2.76)]. The convergence criterion in the 2nd level is set as $\zeta = 10^{-4}$. Once the convergence criterion in the 2nd level is satisfied, the mesh is further densified to $4m \times 4n$ and the convergence criterion is reduced to $\zeta = 10^{-5}$. The fractional film content is interpolated to this new mesh size and the simulation continues until the updated convergence criterion is satisfied.

2.6 Summary

This chapter discusses theories for textured journal bearings while accounting for the lubricant inertia effect, using both Reynolds and Jakobsson-Floberg-Olsson (JFO) boundary conditions. It presents the novel modified Reynolds equations, fluid film thickness equations, solution schemes, and formulations for estimating bearing performance parameters associated with these theories. Additionally, the progressive mesh densification method is explored. Furthermore, formulations for the stability analysis of textured journal bearings, considering the lubricant inertia effect and employing Reynolds boundary conditions, are illustrated. The equations, formulations, and computational methodologies introduced in this chapter are utilized in the subsequent three chapters.

The next chapter presents the steady-state analysis of a textured journal bearing, taking into account the influence of lubricant inertia using Reynolds boundary conditions.



Steady State Analysis of Textured Journal Bearing considering Lubricant Inertia Effect and using Reynolds Boundary Conditions

Contents

Steady State Analysis of Textured Journal Bearing considering Lubricant Inertia Effect and using Reynolds Boundary Conditions	59
3.1 Introduction	61
3.2 Methodology	61
3.3 Validation	61
3.4 Steady State Analysis of Textured Journal Bearing Considering Lubricant Inertia Effect	65
3.4.1 Load-carrying Capacity	66
3.4.2 Flow coefficient	70
3.4.3 Friction variable	73
3.5 Summary	77



3.1 Introduction

The theory pertaining to the steady-state analysis of textured journal bearing considering the lubricant inertia effect was discussed in Chapter 2. In the present chapter, the proposed methodology is validated with the existing results, followed by an analysis of the influence of the lubricant inertia effect on the steady-state characteristics of textured journal bearing.

3.2 Methodology

As discussed in sections 2.2.1 and 2.2.2, the modified Reynolds equation, equation (2.25), is solved by the Gauss-Seidel method with successive over-relaxation (SOR) and the pressure developed inside the bearing is estimated. Once the pressure developed inside the bearing is estimated, the steady-state performance characteristics are estimated using equations (2.35) – (2.39). The Reynolds boundary conditions are applied as per the discussion in section 2.2.5.

3.3 Validation

A MATLAB code has been developed as per the flowchart in Fig. 2.4, implementing the PMD method to calculate the performance parameters for the textured journal bearings, considering the effect of lubricant inertia. Table 3.1 shows the values of the Sommerfeld number and attitude angle obtained from the present analysis for the fixed mesh and PMD method. The results are compared with those of Majumdar [112]. A mesh convergence study was carried out using load capacity as the primary criterion. It was observed that a mesh size of 88×15 represents the minimum mesh size, beyond which further refinement yields negligible variation in results. For the fixed mesh method, a mesh of size 352×60 is used for the analysis with an over-relaxation factor (orf) value of 1.8. The L/D ratio of the bearing is taken as 1. In the PMD method, the mesh sizes for the three levels are 88×15 , 176×30 , and 352×60 .

Table 3.1. Comparison of Sommerfeld number and Attitude angle for Plain Journal Bearings

L/D	ε	Sommerfeld Number			Attitude Angle (degree)		
		FM	PMD	Ref [112]	FM	PMD	Ref [112]
1	0.1	1.33	1.33	1.35	80	80	79
	0.2	0.631	0.631	0.632	74	74	74
	0.3	0.388	0.389	0.382	68	68	68
	0.4	0.260	0.260	0.261	63	63	62
	0.5	0.179	0.179	0.179	57	57	56
	0.6	0.121	0.121	0.120	51	51	50
	0.7	0.078	0.078	0.077	44	44	43
	0.8	0.045	0.045	0.045	36	36	36
	0.9	0.019	0.019	0.019	26	26	25

From Table 3.1, we can see that the results from the present study are in good agreement with the published results. The results from the PMD method are also found to be in good agreement with the FM method.

Table 3.2. Comparison of results obtained by the PMD method and the FM method for Textured Journal bearing

ε	Sommerfeld Number		No of iteration		Time(s)	
	PMD	FM	PMD	FM	PMD	FM
0.1	1.841	1.837	151	964	42	666
0.2	0.742	0.743	147	978	33	734
0.3	0.440	0.442	151	984	41	735
0.4	0.290	0.293	236	1017	59	764
0.5	0.198	0.201	618	1036	169	797
0.6	0.131	0.137	77	1094	5	814
0.7	0.083	0.089	95	1274	5	899
0.8	0.050	0.053	299	4729	15	3235
0.9	0.026	0.026	2091	7015	164	3567

Table 3.2 compares results obtained by the Progressive Mesh Densification (PMD) method and the Fixed Mesh (FM) method for dimple textured bearings with an L/D ratio of 1. The orf is taken as 1.8. The mesh size considered for the first level of the PMD method is 283×45 with a loose convergence criterion 10^{-3} . The mesh sizes for the

successive levels are 566×90 and 1132×180 with convergence criteria of 10^{-4} and 10^{-5} respectively. In the case of the FM method, the mesh is fixed at 1132×180 , and the corresponding convergence criterion is 10^{-5} . It is observed that the values of the Sommerfeld number obtained by the PMD method match those obtained by the FM method for all eccentricity ratios. However, the number of iterations and the time taken by the PMD method is much less than the FM method. It should be noted that for eccentricity ratios 0.8 and 0.9, some inconsistencies in the convergence process occurred. Therefore, the orf value was changed to 1.6 for those two eccentricity ratios to counter the inconsistency. Consequently, we can confirm the computational efficiency of the PMD method for the current study of textured journal bearing.

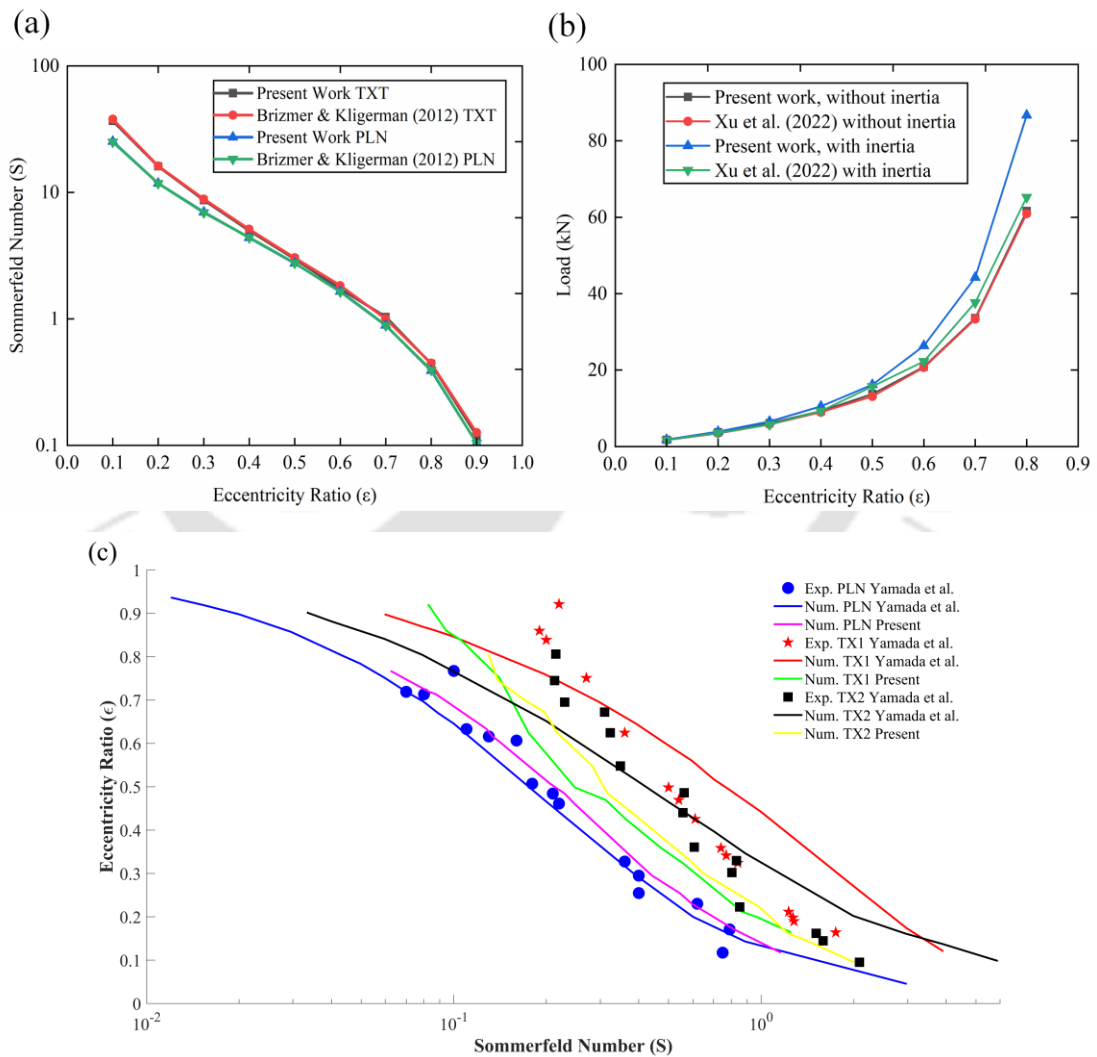


Fig. 3.1. Validation of present results for (a) textured and untextured bearing with Brizmer and Kligerman [67]; (b) inertia and without inertia case with Xu *et al.* [51] (c) textured journal bearing with experimental results of Yamada *et al.* [114]

The results for plain journal bearings and dimple textured journal bearings are compared with the numerical results of Brizmer and Kligerman [67] in Fig. 3.1(a), who used fixed mesh in the finite difference method to solve the non-dimensionalized Reynolds equation. Present results are estimated using the PMD method with mesh sizes of 754×24 for level 1, 1508×48 for level 2, 3016×96 for level 3, and $\text{orf} = 1.8$ to compare the published results as shown in Fig. 3.1(a) for $L/D = 0.2$. Identical texture parameters, viz., non-dimensional clearance $\delta = 0.05$, dimple aspect ratio $\phi = 0.06$, dimple area density $S_p = 0.13$, texture portion $\alpha = 1$, and non-dimensional length, $L_p = 20$ are used for the purpose of comparison. It has been observed that the present results match the published results.

The results with and without inertia conditions are compared with the numerical results of Xu *et al.* [51] in Fig. 3.1(b), who used fixed mesh in the finite difference method. The mesh sizes for the three levels of the PMD method are 88×15 , 176×30 , and 352×60 . The considered operating conditions for this case are; Bearing diameter = 100 mm, Bearing length = 80 mm, Clearance = 50 μm , Fluid density = 1000 kg/m^3 and Fluid viscosity = 0.001 Pa-s. The results are found to be in good agreement, particularly for the case without inertia. The same trend has been observed in the case of inertia. However, the present results give higher load-carrying capacity at eccentricity ratios above 0.5 than the published results.

Further, the values of the Sommerfeld numbers at different eccentricity ratios have been estimated and compared with the experimental and numerical results of Yamada *et al.* [114], shown in Fig. 3.1(c). It is observed that the results for plain bearings are in very good agreement with the experimental and numerical results of Yamada *et al.* In the case of textured bearing, the present results exhibit similar trends with some deviation from the results of Yamada *et al.*, which may be attributed to the variations in texture geometry and numerical solution method. Yamada *et al.* primarily considered square dimples with a fixed distribution, while the present study incorporates spherical dimples and protrusions with varying densities and aspect ratios. These geometric differences can influence localized pressure fields, leading to minor deviations in performance characteristics.

These comparisons validate the code developed using the PMD method; therefore, further analysis of textured journal bearing with and without fluid inertia has been carried out.

3.4 Steady State Analysis of Textured Journal Bearing Considering Lubricant Inertia Effect

This section presents the performance parameters, viz., load carrying capacity, flow coefficient and friction variable. Further, percentage changes of these parameters with inertia effects with respect to no inertia condition are presented to highlight the effects of fluid inertia on these parameters. The percentage changes of these parameters are defined as follows:

$$\% \text{ change in parameter } X = \frac{(X)_{with \text{ inertia}} - (X)_{without \text{ inertia}}}{(X)_{without \text{ inertia}}} \times 100\%$$

In the above expression, X may represent the load carrying capacity, flow coefficient, or friction variable, depending on the specific parameter being evaluated in the analysis. The texturing parameters considered in this present study, for all the cases from here on are non-dimensional clearance $\delta = 0.65$, dimple aspect ratio $\phi = 0.06$, dimple area density $S_p = 0.13$, texture portion $\alpha = 1$, non-dimensional length $L_p = 20$ and $L/D = 1$. The mesh size for level 1 of PMD is taken as 283×45 corresponding to a loose convergence criterion of 10^{-3} . The mesh sizes for the successive levels are 566×90 and 1132×180 with convergence criteria of 10^{-4} and 10^{-5} respectively. The modified Reynolds numbers considered are 0.28, 0.56, and 1.4.

3.4.1 Load-carrying Capacity

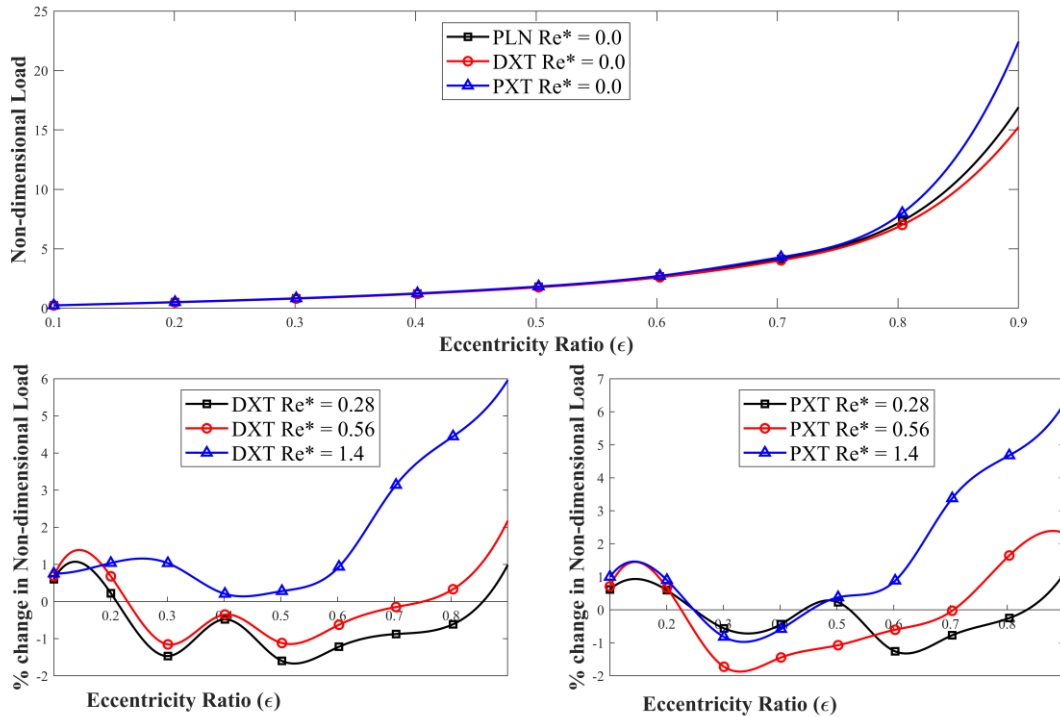


Fig. 3.2. (a) Non-dimensional Load carrying capacity against eccentricity ratio for spherical texture; (b) Percentage change in non-dimensional load carrying capacity with inertia for spherical dimple texturing; (c) Percentage change in non-dimensional load carrying capacity with inertia for spherical protrusion texturing

The effects of the eccentricity ratio on the load-carrying capacity are shown in Fig. 3.2(a) for plain bearings, spherical protruded, and spherical dimple textured bearings. It is observed that the load-carrying capacity increases with the increase in eccentricity ratio for both protruded and dimple textures. Protruded spherical texturing improves the load-carrying capacity, whereas dimple texturing reduces the same for all values of eccentricity ratios compared to plain journal bearings, which has also been reported in the literature [66,109]. The protruded texturing reduces the film thickness in the texturing regions, whereas dimple texturing increases the film thickness in the texturing region. Thus, in the case of protruded texturing, the reduction in film thickness results in more pressure developed, which increases the load carrying capacity for protruded texturing. Fig. 3.2 (b) and 3.2 (c) show the percentage change in the load-carrying capacity against the eccentricity ratio when the lubricant inertia effect is considered in the case of spherical dimple and protrusion textures, respectively. It is seen that, for an eccentricity ratio less

than 0.3, load-carrying capacity increases with increasing modified Reynolds numbers for both dimple and protrusion texturing. Beyond the eccentricity ratio of 0.3, load-carrying capacity deteriorates for lower values of the modified Reynolds number in both the cases. For modified Reynolds number 1.4, the load-carrying capacity increases gradually for $\epsilon > 0.4$ with a maximum of 5.9 % and 6.2 % increment, respectively, for dimple and protrusion texturing when the eccentricity ratio is 0.9.

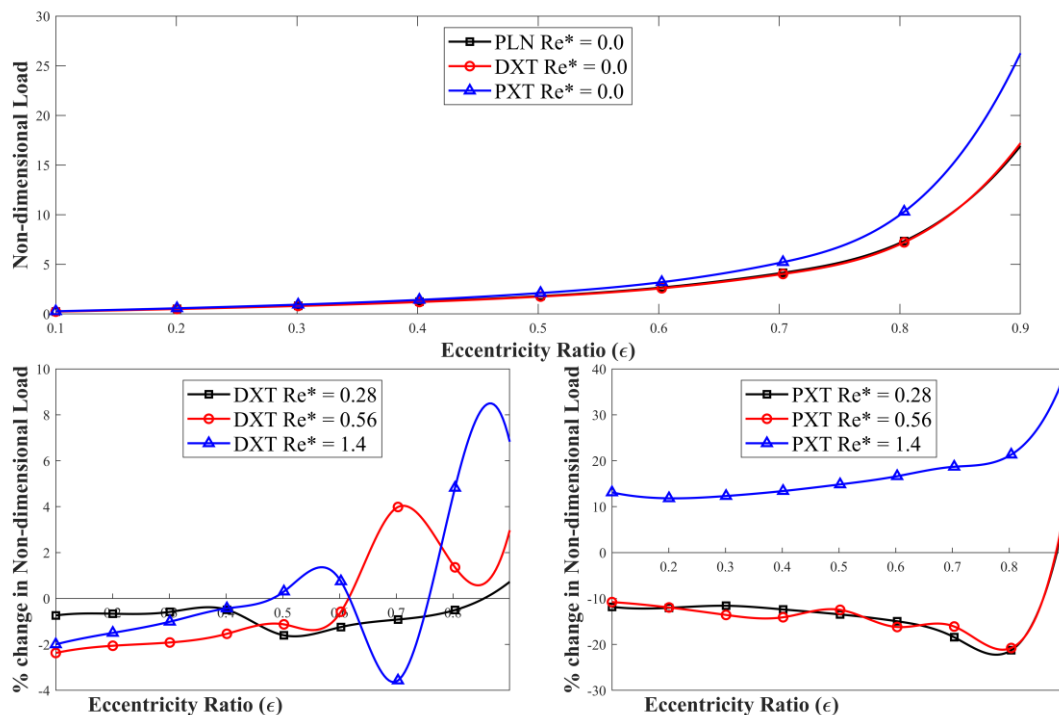


Fig. 3.3. (a) Non-dimensional Load carrying capacity against eccentricity ratio for cylindrical texture; (b) Percentage change in non-dimensional load carrying capacity with inertia for cylindrical dimple texturing; (c) Percentage change in non-dimensional load carrying capacity with inertia for cylindrical protrusion texturing

The effects of the eccentricity ratio on the load-carrying capacity are shown in Fig. 3.3(a) for plain bearings, cylindrical protruded, and cylindrical dimple textured bearings. It is observed that the load-carrying capacity increases with the increase in eccentricity ratio for plain, protruded and dimple textures. Among them, protrusion texturing exhibits the highest load values, particularly at higher eccentricity ratios, followed by dimple texturing and plain bearings, which show similar values of load-carrying capacity. Fig. 3.3 (b) presents the percentage change in non-dimensional load-carrying capacity for cylindrical dimple texturing at varying Re^* values. At lower

eccentricity ratios ($\epsilon < 0.5$), the percentage change is negligible or slightly negative, but as the eccentricity ratio increases beyond 0.5, the percentage change becomes positive and grows significantly, especially for higher modified Reynolds numbers ($Re^* = 1.4$). This indicates that increasing Reynolds numbers amplify the load-carrying capacity at higher eccentricities. Fig. 3.3 (c) shows the percentage change in non-dimensional load carrying capacity of cylindrical protrusion textured bearing, where percentage changes are plotted for $Re^* = 0.28$, $Re^* = 0.56$ and $Re^* = 1.4$. It is observed that for $Re^* = 0.28$ and $Re^* = 0.56$, the load carrying capacity is negatively affected except at $\epsilon = 0.9$. However, a steep positive increase is observed at a higher value of the modified Reynolds number, *i.e.* $Re^* = 1.4$.

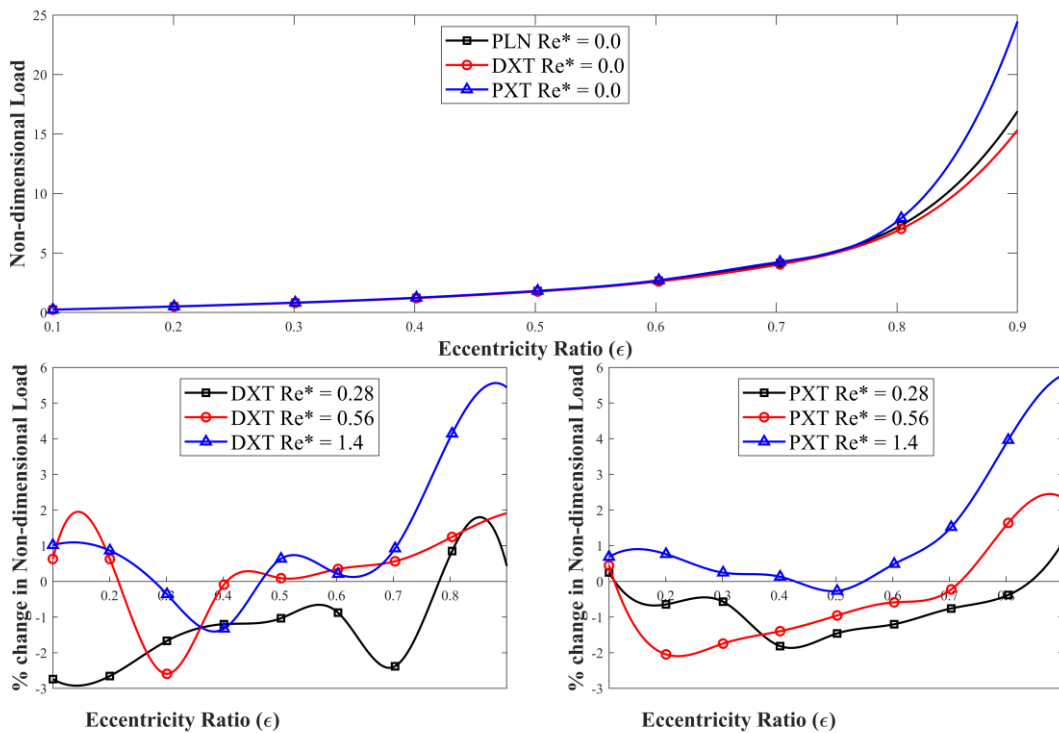


Fig. 3.4. (a) Non-dimensional Load carrying capacity against eccentricity ratio for square texture; (b) Percentage change in non-dimensional load carrying capacity with inertia for square dimple texturing; (c) Percentage change in non-dimensional load carrying capacity with inertia for square protrusion texturing

Figure 3.4 illustrates the variation of non-dimensional load-carrying capacity and its percentage change with respect to the eccentricity ratio for square dimple and protrusion texturing with varying modified Reynolds numbers. In Fig. 3.4 (a), the non-

dimensional load carrying capacity is plotted for three cases, *i.e.*, plain bearings, square dimple texturing, and square protrusion texturing at $Re^* = 0$. The non-dimensional load-carrying capacity increases with increasing eccentricity ratios for all the cases, showcasing the influence of eccentricity on hydrodynamic pressure generation. Protrusion texturing exhibits the highest load values at higher eccentricity ratios, followed closely by plain bearings, while dimple texturing shows the lowest values. Fig. 3.4 (b) presents the percentage change in non-dimensional load carrying capacity for square dimple texture at varying modified Reynolds number values. Unlike cylindrical texturing, oscillatory behaviour is observed at lower eccentricity ratios, particularly for $Re^* = 0.56$ and $Re^* = 1.4$, indicating sensitivity to lubricant inertia effect in the case of square texturing. Positive changes dominate at higher eccentricity ratios, with $Re^* = 1.4$ showing the largest increase in percentage change. Fig. 3.4 (c) illustrates similar trends for square protrusion texturing, where oscillatory behaviour is prominent at lower eccentricity ratios, especially for $Re^* = 0.56$. At higher eccentricity ratios, positive changes are observed, with $Re^* = 1.4$ exhibiting the steepest increase in percentage change compared to other Reynolds numbers. The square texture geometry demonstrates a more complex response to flow dynamics than cylindrical geometry, with oscillations at lower eccentricities and significant positive changes at higher eccentricities, particularly for PXT and DXT cases under high Reynolds numbers ($Re^* = 1.4$). These observations highlight how texture geometry influences hydrodynamic bearing performance under varying flow conditions and eccentricity ratios.

These results highlight the critical influence of texturing geometry and lubricant inertia effects on hydrodynamic bearing performance, emphasizing that both factors play a pivotal role in enhancing the load-carrying capacity of textured journal bearings.

3.4.2 Flow coefficient

The variation of flow coefficient with eccentricity ratio for plain journal bearings, protrusion textured journal bearings, and dimple textured journal bearings are shown in Fig. 3.5 (a). It is observed that the value of the flow coefficient increases with increasing eccentricity ratio for all the cases. Protruded texturing gives relatively better flow than dimple texturing; however, it is observed that both protruded and dimple texturing result in the reduction of flow coefficients compared to plain journal bearings for all eccentricity ratios, which is due to the fact that the presence of textures on the bearing surface results in pressure drop in the texturing regions. The results are in line with the reported works [61,74].

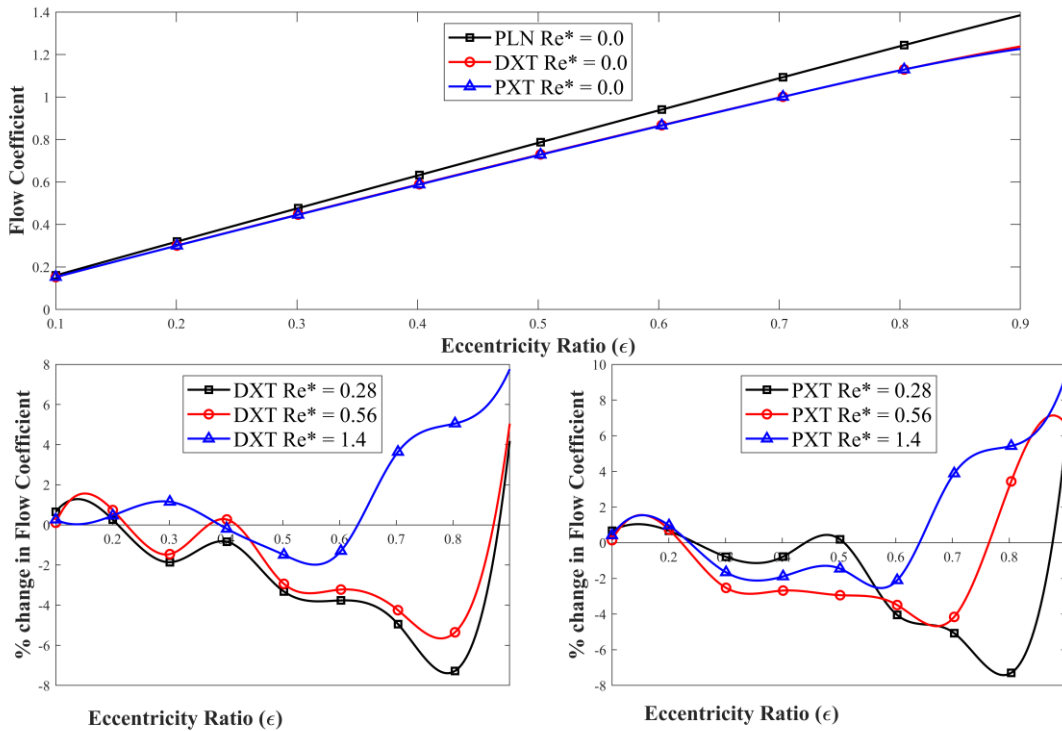


Fig. 3.5. (a) Non-dimensional flow coefficient against eccentricity ratio for spherical texture; (b) Percentage change in non-dimensional flow coefficient with inertia for spherical dimple texturing; (c) Percentage change in non-dimensional flow coefficient with inertia for spherical protrusion texturing

Figure 3.5 (b) examines the percentage change in flow coefficient for dimple cylindrical texture at varying modified Reynolds numbers. At $Re^* = 0.28$ and $Re^* = 0.56$, the percentage change fluctuates around zero for lower eccentricity ratios ($\epsilon < 0.3$),

indicating minimal impact of texture at low Reynolds numbers. At $Re^* = 1.4$, significant positive changes are observed as eccentricity increases, peaking sharply near $\varepsilon = 0.9$. Fig. 3.5 (c) presents similar trends for protrusion cylindrical texture across varying modified Reynolds numbers. At $Re^* = 0.28$, the percentage change in flow coefficients is minimal and fluctuates around zero until $\varepsilon > 0.8$, indicating limited influence of texture at low Reynolds numbers and lower eccentricities. For $Re^* = 0.56$, the gradual positive changes occur beyond $\varepsilon = 0.7$ showcasing the improved performance of protrusion spherical textures under moderate Reynolds numbers as eccentricity rises. At $Re^* = 1.4$, sharp increases are observed at higher eccentricities ($\varepsilon > 0.6$), peaking near $\varepsilon = 0.9$ with a maximum positive change of 9.4%.

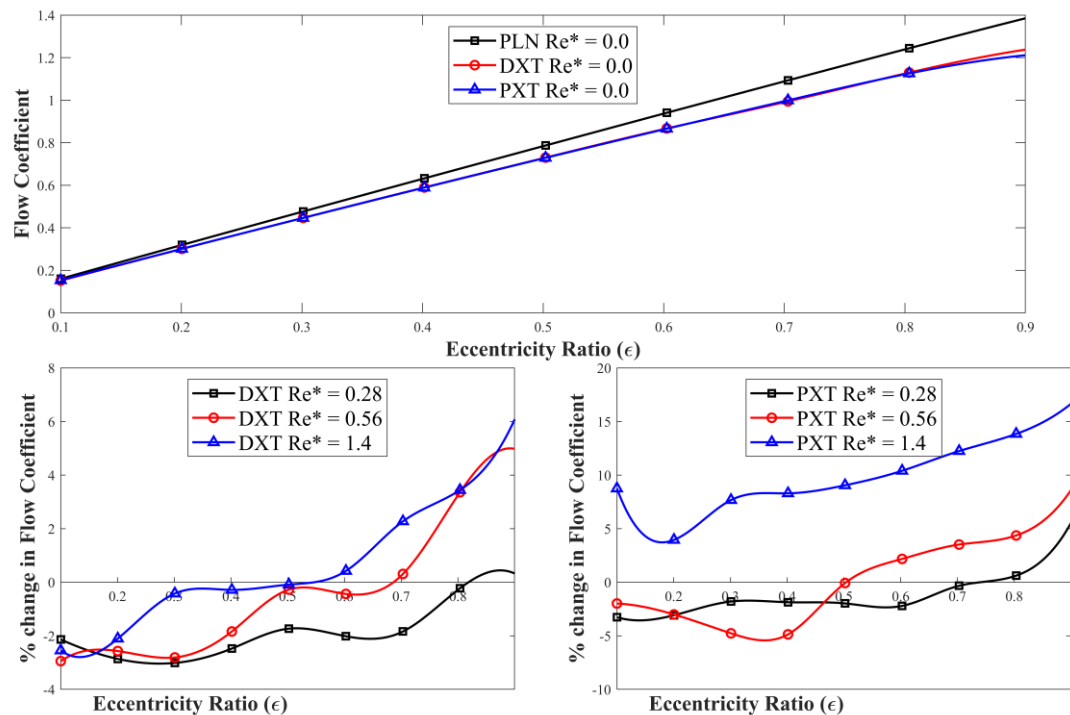


Fig. 3.6. (a) Non-dimensional flow coefficient against eccentricity ratio for cylindrical texture; (b) Percentage change in non-dimensional flow coefficient with inertia for cylindrical dimple texturing; (c) Percentage change in non-dimensional flow coefficient with inertia for cylindrical protrusion texturing

Figure 3.6 illustrates the relationship between flow coefficient and eccentricity ratio (ε) for cylindrical texture, along with percentage changes in flow coefficient for textured configurations (dimple and protrusion) across varying Reynolds numbers. In Fig.

3.6 (a), the flow coefficient increases linearly with the eccentricity ratio for plain (PLN), cylindrical dimple (DXT), and cylindrical protrusion-textured (PXT) bearings at $Re^* = 0.0$, with plain bearings showing slightly higher values, while dimple texturing and protrusion texturing exhibit almost identical behaviour, indicating minimal influence of surface texturing at low modified Reynolds numbers. Fig. 3.6 (b) and 3.6 (c) show the percentage change in the flow coefficient for cylindrical dimple and cylindrical protrusion textured bearings at higher modified Reynolds numbers. For dimple textured bearings, Fig. 3.6 (b) reveals that at low eccentricities ($\varepsilon < 0.5$), the flow coefficient change remains close to zero, but as the eccentricity ratio increases beyond 0.5, the flow coefficient starts to rise, particularly at higher Reynolds numbers, with $Re^* = 1.4$ showing a 5–6% increase. In Fig. 3.6 (c), cylindrical protrusion textured bearings demonstrate a much more pronounced effect, with the flow coefficient increasing by over 15% at $Re^* = 1.4$ and showing significant improvements even at moderate Reynolds numbers. This suggests that cylindrical protrusion textures (PXT) are more effective than cylindrical dimple texturing in enhancing lubricant flow, particularly at high eccentricity ratios and modified Reynolds numbers.

The variation of the flow coefficient with the eccentricity ratio (ε) for plain journal bearing, square dimple textured and square protrusion textured journal bearing configurations under varying Reynolds numbers are shown in Fig. 3.7 (a). Similar to spherical and cylindrical texturing, the flow coefficient increases almost linearly with eccentricity for plain (PLN), square dimple (DXT), and square protrusion-textured (PXT) bearings at $Re^* = 0.0$, with PLN showing slightly higher values compared to DXT and PXT, which exhibit nearly identical trends. Fig. 3.7 (b) and 3.7 (c) depict the percentage change in the flow coefficient for DXT and PXT bearings at different Reynolds numbers. DXT bearings show minor variations for $\varepsilon < 0.5$, but a significant increase beyond $\varepsilon = 0.5$, particularly for $Re^* = 1.4$, where the flow coefficient rises by over 6%. Fig 3.7 (c) highlights PXT bearings, where the flow coefficient change remains close to zero or negative for $\varepsilon < 0.6$, but beyond this threshold, a sharp increase is observed, especially for $Re^* = 1.4$, reaching over 10% at high eccentricities. These findings suggest that surface textures influence lubricant flow more prominently at higher Reynolds numbers

and higher eccentricity ratios, with protrusion texturing providing the most substantial enhancements in lubricant circulation.

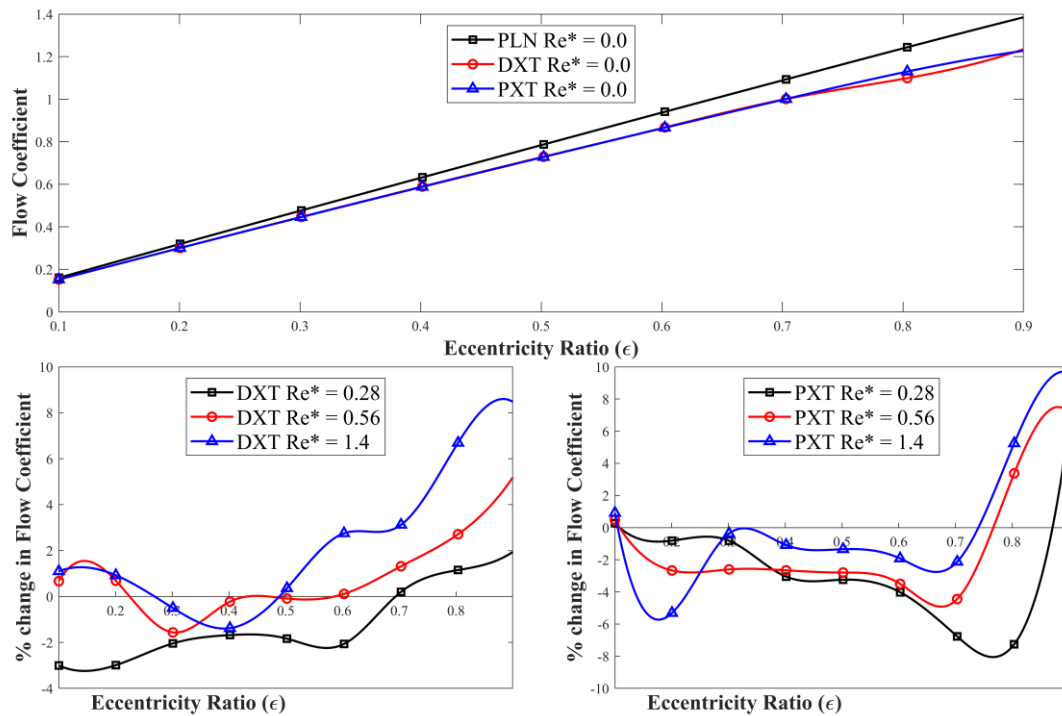


Fig. 3.7. (a) Non-dimensional flow coefficient against eccentricity ratio for square texture; (b) Percentage change in non-dimensional flow coefficient with inertia for square dimple texturing; (c) Percentage change in non-dimensional flow coefficient with inertia for square protrusion texturing

3.4.3 Friction variable

The effect of the eccentricity ratio on the friction variable for plain bearings, spherical dimple textured bearings and spherical protrusion textured bearings is shown in Fig. 3.8 (a). It is seen that the value of the friction variable decreases with increasing eccentricity ratios. For both spherical protruded and dimple texturing, the friction variable is found to be lesser than the plain journal bearing case, with protruded texturing showing more improvement than dimple texturing. This has also been reported by Sharma *et al.* [66]. There may be many reasons for the improvement in friction characteristics. One of the reasons may be that the load-carrying capacity is inversely proportional to the friction variable. Therefore, the increase in the load-carrying capacity decreases the friction variable in the case of protruded bearings.

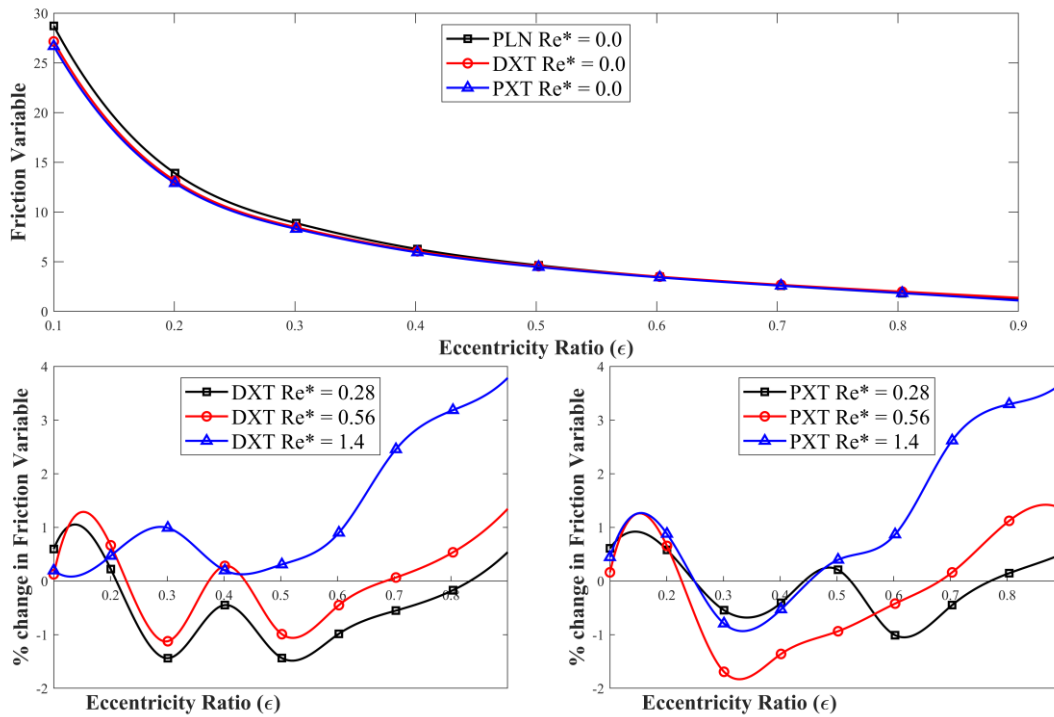


Fig. 3.8. (a) Friction variable against eccentricity ratio for spherical texture; (b) Percentage change in friction variable with inertia for spherical dimple texturing; (c) Percentage change in friction variable with inertia for spherical protrusion texturing

The percentage change in friction variable with eccentricity ratios due to the lubricant inertia effect for spherical dimple textured bearing is shown in Fig. 3.8 (b). Here, the reduction in the friction variable is depicted as a positive change in percentage. In the case of the spherical dimple textured (DXT) bearing, increasing the modified Reynolds number initially results in a reduction in friction at very low eccentricities ($\epsilon < 0.3$). However, in the intermediate eccentricity range ($\epsilon \approx 0.3 - 0.5$), the friction variable increases (negative percentage change) for certain Re^* values. At higher eccentricity ratios ($\epsilon > 0.6$), friction again decreases for higher modified Reynolds numbers, suggesting that at this stage, inertia effects dominate, improving lubricant circulation and film thickness, thereby reducing friction. The percentage change in friction variable with eccentricity ratios due to the lubricant inertia effect for spherical protrusion textured bearing is shown in Fig. 3.8 (c). It is seen that when the eccentricity ratio is less than 0.3, the percentage change in the friction variable increases with increasing modified

Reynolds number. For the modified Reynolds number of 1.4 and at eccentricity ratios of 0.3 and 0.4, the friction variable rises compared to the no inertia case. Beyond this, it improves significantly from 0.38% at $\varepsilon = 0.5$ to 3.7% at $\varepsilon = 0.9$. A similar trend is observed for the modified Reynolds number 0.56 beyond the eccentricity ratio of 0.6. This suggests that at high Reynolds numbers and large eccentricities, spherical protrusions help in stabilizing the lubrication film, enhancing load-carrying capacity, and thereby reducing friction variables.

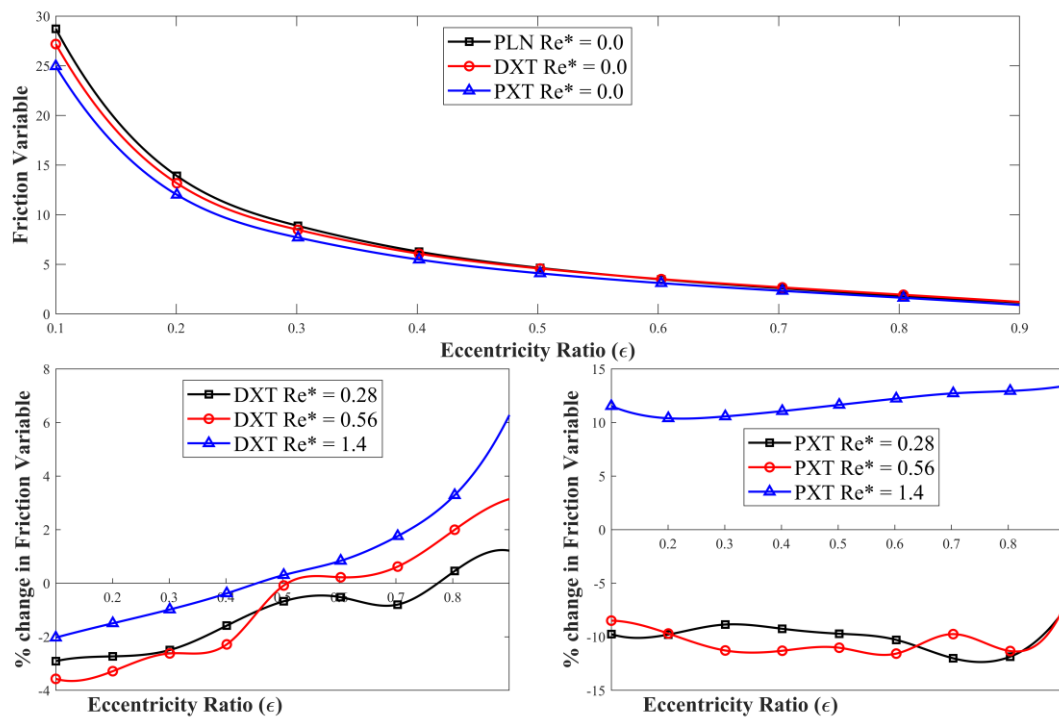


Fig. 3.9. (a) Friction variable against eccentricity ratio for cylindrical texture; (b) Percentage change in friction variable with inertia for cylindrical dimple texturing; (c) Percentage change in friction variable with inertia for cylindrical protrusion texturing

The variation of the friction variable with the eccentricity ratio (ε) for plain journal bearing, cylindrical dimple textured and cylindrical protrusion textured journal bearing are shown in Fig. 3.9 (a), whereas the percentage change in friction variable with increasing inertia for cylindrical dimple texture (DXT) and cylindrical protrusion texture (PXT) are presented in Fig. 3.9 (b) and 3.9 (c) respectively. From Fig. 3.9 (b), it is observed that DXT bearings exhibit a reduction in friction (positive percentage change) at higher eccentricity ratios ($\varepsilon > 0.5$) for increasing Re^* . On the other hand, in the case of PXT bearings (Fig. 3.9 (c)), a clear distinction is observed in friction behaviour, where

at higher modified Reynolds numbers ($Re^* = 1.4$), a substantial reduction in friction variables occurs for all values of eccentricity ratios. However, friction variables are found to be increasing at low modified Reynolds numbers, indicating that the presence of protrusions can disturb lubricant flow and cause shear amplification in certain conditions [115].

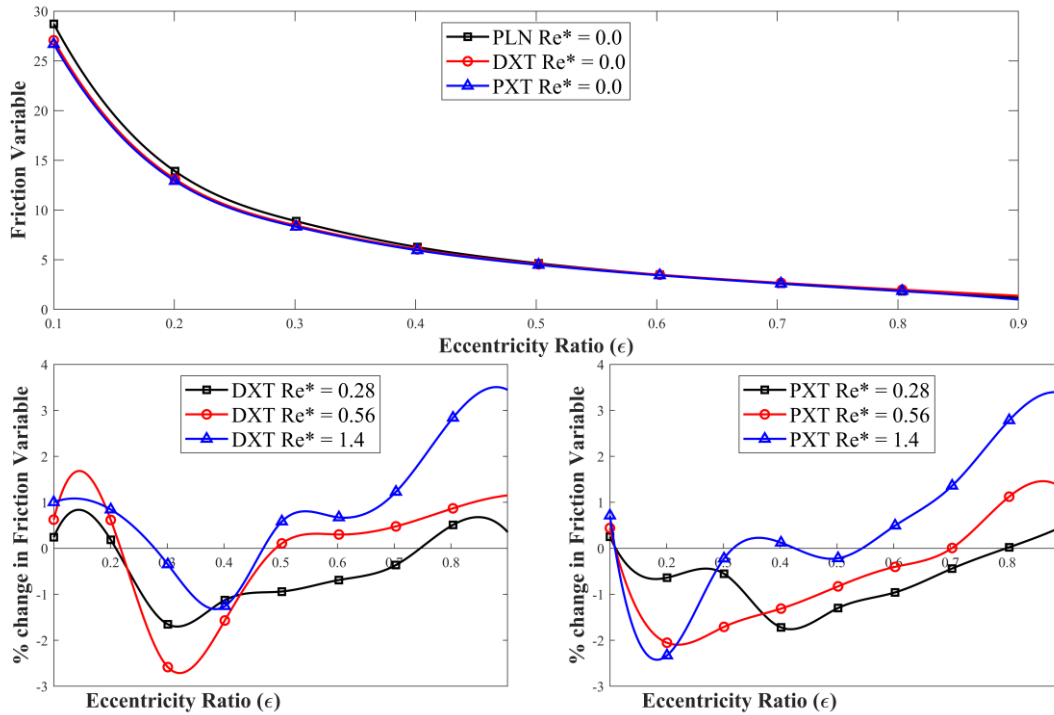


Fig. 3.10. (a) Friction variable against eccentricity ratio for square texture; (b) Percentage change in friction variable with inertia for square dimple texturing; (c) Percentage change in friction variable with inertia for square protrusion texturing

The variation of friction variable with increasing eccentricity ratio for plain (PLN), square dimple (DXT) and square protrusion (PXT) texturing is shown in Fig. 3.10 (a) for no inertia condition. The friction variable decreases with the increase in eccentricity ratio for all three configurations and protrusion texturing exhibits lesser friction variables than dimple texturing and plain bearings. Fig. 3.10 (b) and Fig. 3.10 (c) illustrate the percentage change in friction variable for the DXT and the PXT bearings under different Re^* values. In Fig. 3.10 (b), it is observed that the DXT bearings exhibit reduced friction (positive percentage change) at higher eccentricities ($\epsilon > 0.5$) as the modified Reynolds number increases. Fig. 3.10 (c) shows the percentage change in friction variable for square PXT bearings. At higher eccentricities ($\epsilon > 0.5$), the PXT

bearings demonstrate a more pronounced reduction in friction variable compared to the DXT bearings, particularly at $Re^* = 1.4$.

3.5 Summary

In this chapter, a numerical study has been carried out to assess the effect of lubricant inertia on the steady-state characteristics of textured journal bearings – for both protrusion and dimple textures. The effectiveness of the progressive mesh densification (PMD) method to achieve computational efficiency in the case of textured journal bearings analysis has been validated. The performance characteristics considered here are the non-dimensional load-carrying capacity, non-dimensional flow coefficient, and friction variable. The variations in the performance parameters are investigated with varying eccentricity ratios for different modified Reynolds numbers, a measure of lubricant inertia. The texture shapes considered are the spherical, cylindrical and square texture. It is observed that protrusion texturing enhances the non-dimensional load-carrying capacity and friction variable compared to plain bearings, whereas the non-dimensional flow coefficient is adversely affected due to texturing. Among the texture geometries, cylindrical texturing shows significant enhancement in the performance characteristics at higher modified Reynolds numbers, followed by spherical and square textures. Further, the increase in the effect of lubricant inertia significantly enhances the performance characteristics of textured journal bearings.

The next chapter presents the steady-state analysis of textured journal bearing considering the lubricant inertia effect incorporating mass-conserving (JFO) boundary conditions.



Steady State Analysis of Textured Journal Bearing Considering Lubricant Inertia Effect using Mass-Conserving (JFO) Boundary Conditions

Contents

Steady State Analysis of Textured Journal Bearing Considering Lubricant Inertia Effect using Mass-Conserving (JFO) Boundary Conditions	79
4.1 Introduction	81
4.2 Methodology	81
4.3 Validation	82
4.4 Steady State Analysis of Textured Journal Bearing Considering Lubricant Inertia effect and cavitation	83
4.4.1 Load-carrying Capacity	84
4.4.2 Flow coefficient	90
4.4.3 Friction variable	95
4.5 Summary	101



4.1 Introduction

The steady-state analysis of textured journal bearings considering lubricant inertia effect using Reynolds boundary conditions was presented in the Chapter 3. The analysis provided insight into the performance of textured bearings without accounting for cavitation, which can significantly influence bearing behaviour in practical applications. Cavitation in journal bearings occurs when the pressure of the lubricant drops below the vapour pressure. Numerically, the cavitation occurring in the bearings can be treated by using the Jacobson-Floberg-Olsen (JFO) boundary conditions, which is a mass-conserving type boundary condition. A Novel Modified Reynolds equation, incorporating the JFO boundary conditions and the lubricant inertia effect, has been developed and presented in chapter 2. In the present chapter, the proposed methodology has been validated with the benchmark results from existing literature, followed by the discussion on the influence of lubricant inertia effect and cavitation on the steady-state characteristics of textured journal bearing.

4.2 Methodology

As discussed in the section 2.3, a Novel Modified Reynolds equation has been formulated incorporating the JFO boundary conditions and the lubricant inertia effect. The Novel Modified Reynolds equation, represented by Equation (2.60), along with the flow terms, Equations (2.53) and (2.54), are simultaneously solved by the Gauss-Seidel method with successive over-relaxation (SOR) and the fractional film content is estimated. The pressure developed inside the bearing is estimated by Equation (2.52). Once the pressure developed inside the bearing is estimated, the steady-state performance characteristics are estimated using Equations (2.68)–(2.70).

4.3 Validation

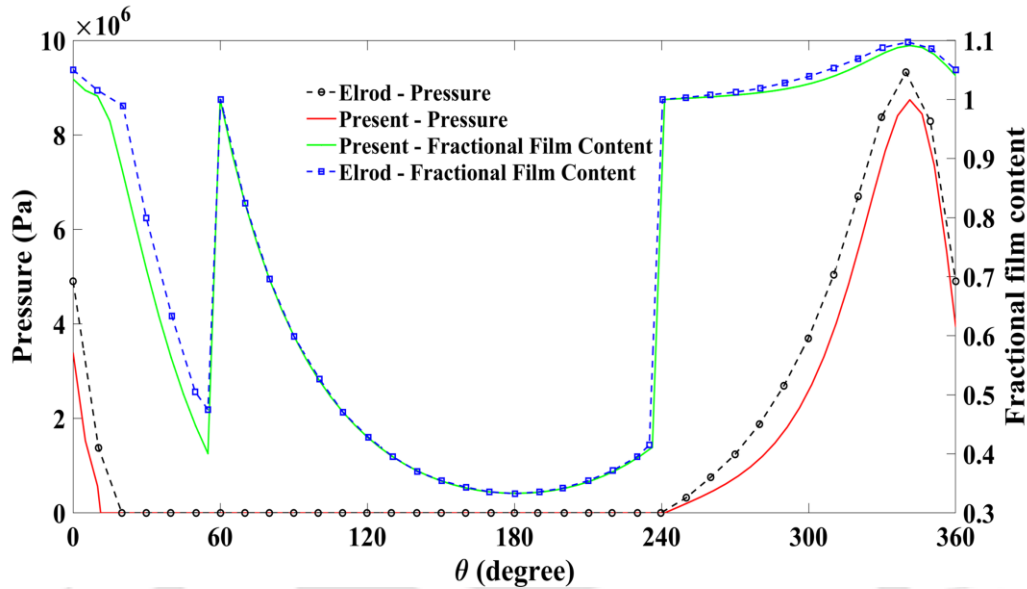


Fig. 4.1. Comparison of current results with Elrod [5]

A MATLAB code has been developed based on the numerical scheme described in the preceding sections, incorporating the Progressive Mesh Densification (PMD) method. This code is used to estimate the non-dimensional performance characteristics of a journal bearing with dimple and protrusion texturing, accounting for cavitation and lubricant inertia effects.

Since no benchmark results are available for direct validation, the present results are generated with $Re^* = 0$ (*i.e.*, no inertia effect) and compared with those of Elrod [5] in Fig. 4.1. The results are found to be satisfactory though a slight but acceptable difference is observed between the two sets of results, particularly for pressure, which can be attributed to the differences in numerical approaches – while the present study employs PMD, Elrod [5] used a Fixed Mesh for the iterative solution. Additionally, the modified switch function algorithm proposed by Fesanghary and Khonsari [97] has been implemented in the present analysis. Being satisfied with the comparative analysis between the Elrod and Present models, the validated numerical framework is now employed to generate the pressure distribution and the fractional film contents for textured journal bearings for different modified Reynolds numbers.

4.4 Steady State Analysis of Textured Journal Bearing Considering Lubricant Inertia effect and cavitation

Table 1 presents the texturing parameters used in the current analysis, derived from the works of Brizmer and Kligerman [67]. The texturing considered is a full textured journal bearing. Brizmer and Kligerman specified a value of 13% for dimple area density (S_p) corresponding to maximum load. In our study, the maximum load is observed at a dimple area density, $S_p = 15\%$, closely aligning with the selected value of 13% by Brizmer and Kligerman. The dimple aspect ratio and non-dimensional clearance are determined to prevent metal-to-metal contact in the case of protrusion-textured bearings. In the case of protrusion textured journal bearings at higher eccentricity ratios, if the value of non-dimensional clearance is too low or the value of the dimple aspect ratio is too high, the scope of metal-to-metal contact arises. Therefore, a non-dimensional clearance (δ) in the range of 0.50 – 0.70 and a dimple aspect ratio (ψ) of 0.01 – 0.09 allows us to avoid such scenarios. For the Progressive Mesh Densification (PMD) method, the mesh size ($m \times n$) at level 1 is set at 88×14 , ensuring a square grid, which is subsequently densified to 176×28 and 352×56 in the successive levels. The convergence criterion is reduced from 10^{-3} to 10^{-5} , and the relaxation factor varies between 0.01 and 1. The considered values of Re^* are 0.5, 1.0 and 1.5.

Table 4.1. Operating and texturing parameters

Parameters	Values
Dimple area density (S_p)	0.15
Dimple aspect ratio (ψ)	0.06
Non-dimensional clearance (δ)	0.65
Texture portion (α)	1
Eccentricity Ratio (ε)	0.1 – 0.9
L/D ratio	1
$\bar{\beta}$	60
Non-dimensional Cavitation pressure	0

4.4.1 Load-carrying Capacity

Spherical Textured Bearing

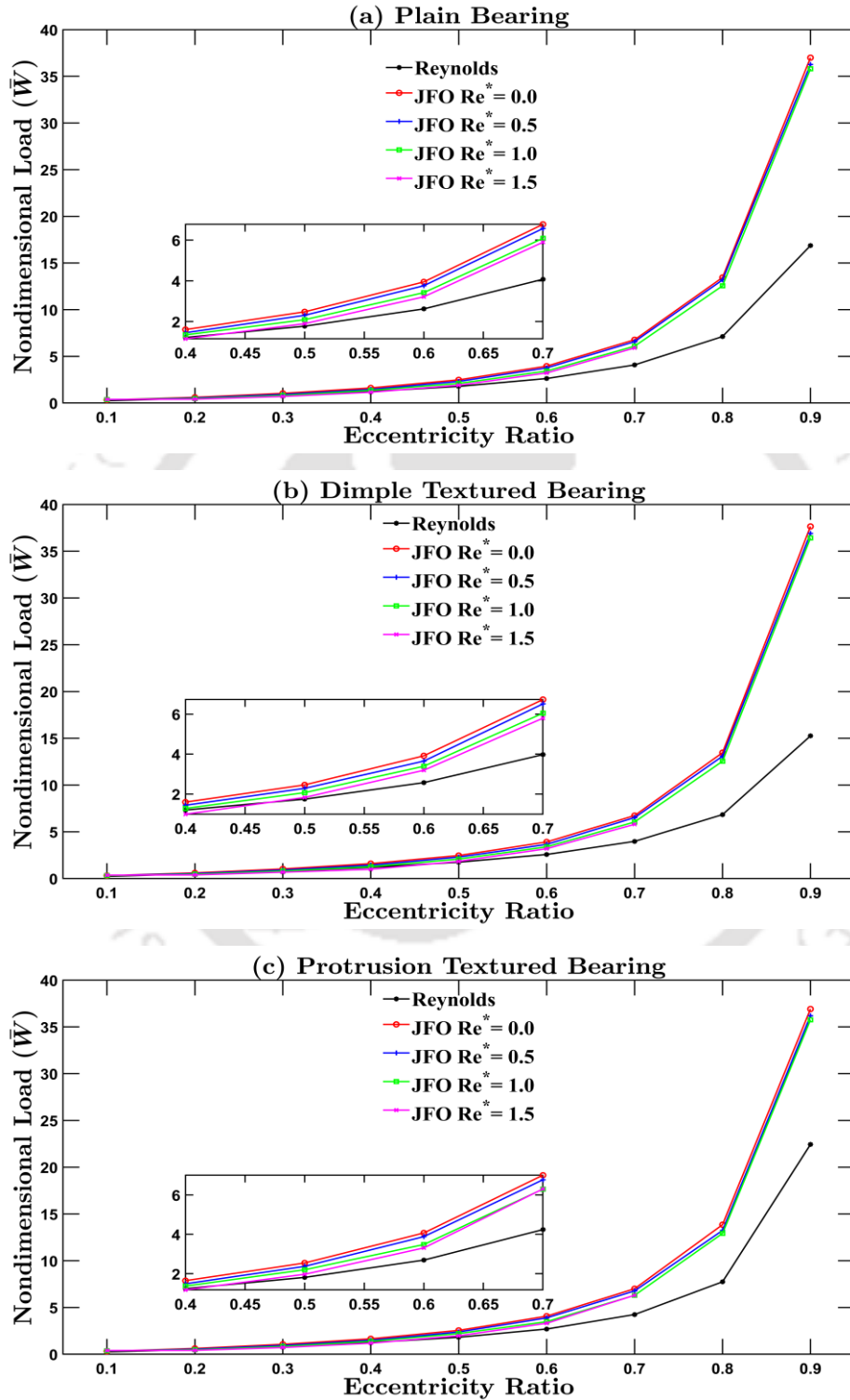


Fig. 4.2. Comparison of non-dimensional load capacity for Reynolds and JFO boundary conditions for (a) plain, (b) dimple and (c) protrusion textured bearing

The non-dimensional load carrying capacity (LCC) with increasing eccentricity ratio (ε) and increasing modified Reynolds number (Re^*) are presented in Fig. 4.2 for spherical textured bearing. The analysis involves both Reynolds and JFO boundary conditions and the results are presented for plain bearings (PLN) in Fig. 4.2 (a), and for dimple-textured bearings (DXT) in Fig. 4.2 (b), and protrusion-textured bearings (PXT) in Fig. 4.2 (c). As expected, the non-dimensional load carrying capacity increases with increasing modified Reynolds number under both Reynolds and JFO boundary conditions. This trend is consistent with classical lubrication theory, where a higher eccentricity ratio results in a more pronounced converging wedge, leading to increased hydrodynamic pressure buildup and consequently higher load-carrying capacity. It is observed that the load-carrying capacity values predicted using the JFO boundary conditions are consistently higher than those obtained using Reynolds boundary conditions across different bearing types. This discrepancy arises due to the fundamental differences between these two cavitation models. The Reynolds boundary condition assumes that the pressure in the cavitated region is constant and does not account for mass flow conservation, which can lead to an underestimation of the pressure developed at the film reformation boundaries. In contrast, the JFO boundary conditions enforce mass conservation, ensuring a more realistic representation of lubricant film behaviour, particularly at higher eccentricity ratios [97].

Upon introducing inertia, the combined influence of cavitation and inertia leads to a reduction in LCC with increasing modified Reynolds numbers (Re^*) for all the cases of texturing as seen in Fig. 4.2. Due to the presence of the textures, the increased inertia may prevent the effective redistribution of lubricant into cavitated areas, resulting in a reduction in load-carrying capacity as inertia increases. These findings for textured journal bearings are in line with the results for textured slider bearings [83,105,116]. Further, it has been observed that under the effect of lubricant inertia, the protrusion textured bearing shows higher values of non-dimensional load-carrying capacity than plain and dimple textured bearings under JFO boundary conditions. The protrusion texture decreases the local film thickness in textured regions, whereas the dimple texture increases it. Consequently, the decreased film thickness in the protrusion textured bearing generates higher pressure, enhancing the load-carrying capacity. This improvement in

load-carrying capacity becomes particularly significant for moderate to heavily loaded bearings ($0.4 \leq \varepsilon \leq 0.9$).

Effect of Texture Geometry

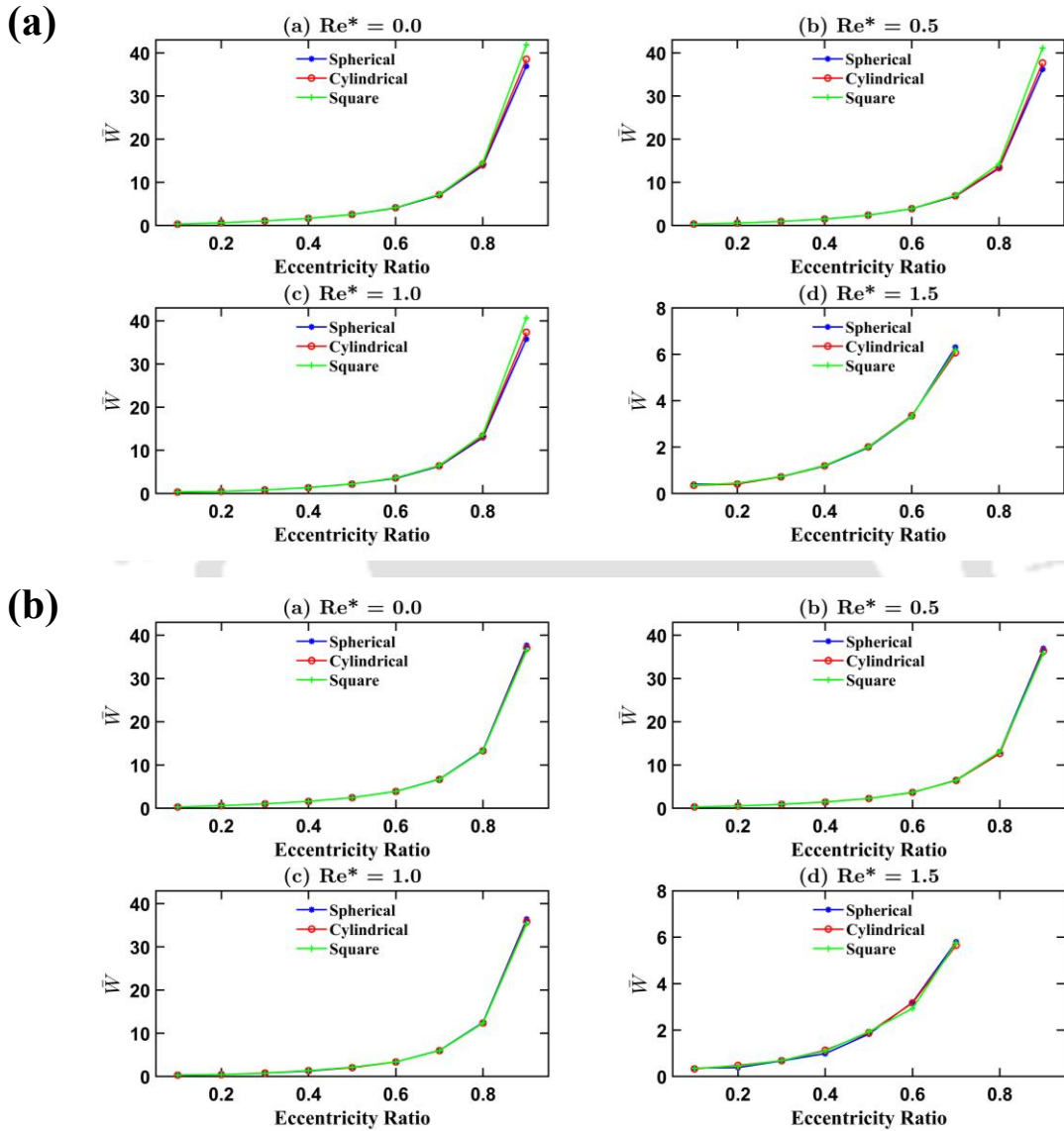


Fig. 4.3. Variation of non-dimensional load-carrying capacity with eccentricity ratio for spherical, cylindrical and square texture with increasing inertia using JFO boundary conditions for (a) protrusion and (b) dimple texturing

The variation of non-dimensional load-carrying capacity (\bar{W}) with increasing eccentricity ratio (ε) and increasing modified Reynolds numbers (Re^*) under JFO boundary conditions for spherical, cylindrical and square texture for protrusion and dimple texturing are shown in Figs. 4.3 (a) and 4.3 (b) respectively. The non-dimensional

load-carrying capacity increases with increasing eccentricity ratio for all three texturing geometries for both dimple and protrusion texturing. The texturing geometries, however, have less influence up to an eccentricity ratio of 0.7, for protrusion texturing. Beyond this, square texturing produces a higher load-carrying capacity, followed by cylindrical and spherical texturing.

Further, the load-carrying capacity decreases with the increase in modified Reynolds numbers for all the texturing configurations. On the other hand, in the case of dimple texturing, the texturing geometry doesn't have much influence on the load-carrying capacity except at $\varepsilon = 0.9$, where spherical texturing produces more load-carrying capacity than cylindrical and square texturing. The load-carrying capacity, however, was found to be decreasing with the increase in modified Reynolds numbers. This suggests that, under hydrodynamic lubrication conditions, texture geometry alone does not drastically alter the overall bearing performance. However, at higher Reynolds numbers, variations become more apparent, with square textures showing a slight advantage. This suggests that the choice of texture geometry may be more relevant in applications with significant inertia effects.

Effect of Dimple Aspect Ratio

The influence of dimple aspect ratio on the non-dimensional load-carrying capacity with increasing inertia effect under JFO boundary conditions for spherical, cylindrical and square texture for protrusion and dimple texturing for a fixed eccentricity ratio of 0.5 are shown in Figs. 4.4 (a) and 4.4 (b) respectively. It is observed that, for all the three texturing geometries, the load-carrying capacity increases with increasing dimple aspect ratio (ψ) for protrusion texturing whereas the load-carrying capacity decreases with increasing dimple aspect ratio (ψ) for dimple texturing, with protrusion texturing yielding higher load-carrying capacity than dimple texturing. Further, it is observed that the load-carrying capacity decreases with the increase in modified Reynolds number for both protrusion and dimple texturing. Spherical dimples exhibit the highest load capacity at lower Re^* , while square textures yield slightly higher load-carrying capacity at higher Re^* due to increased surface interaction, whereas cylindrical protrusions consistently yield the highest load capacity than spherical and square protrusions.

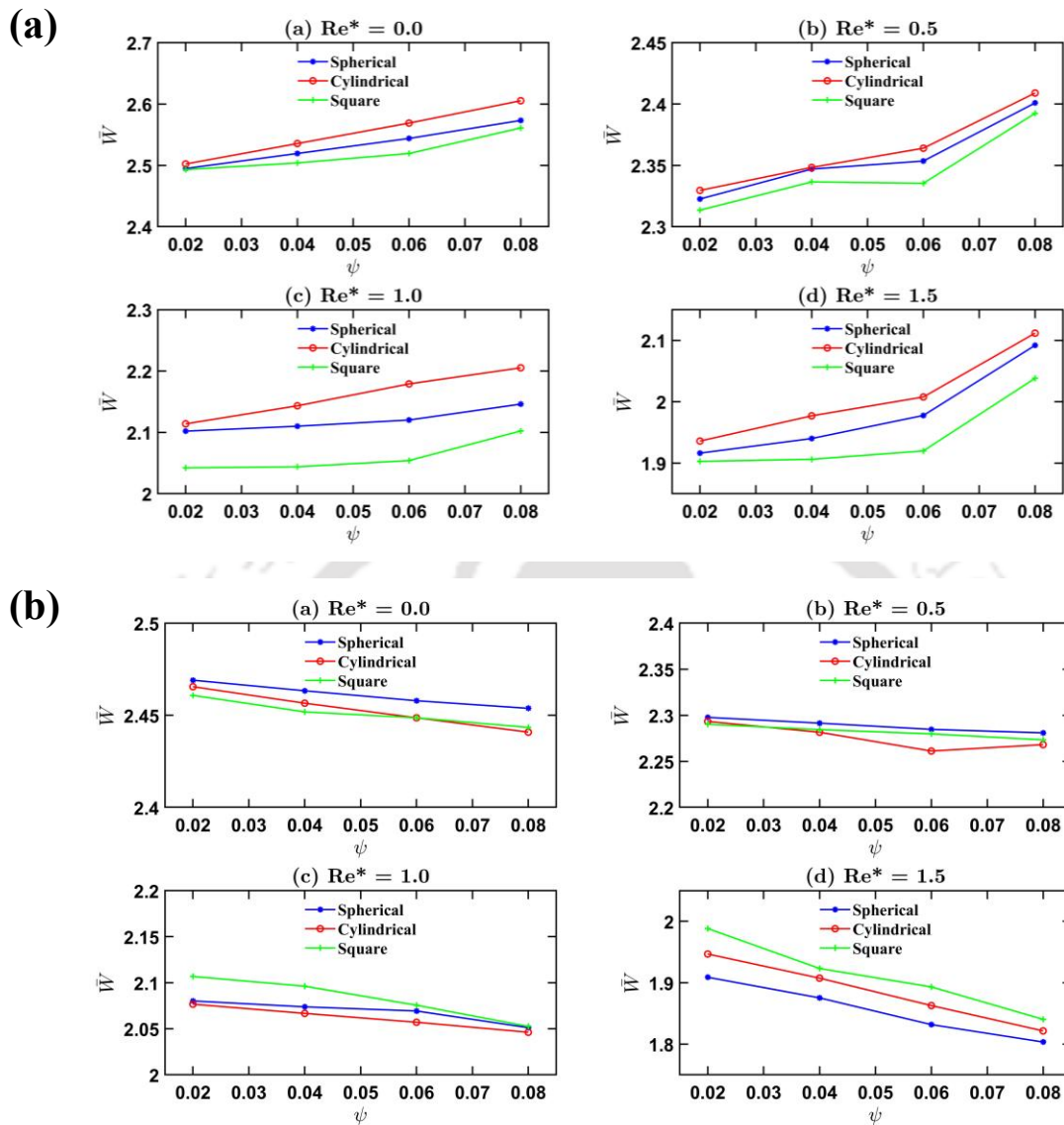


Fig. 4.4. Non-dimensional load-carrying capacity Vs Dimple aspect ratio for spherical, cylindrical and square texture with increasing inertia and JFO boundary conditions for (a) protrusion and (b) dimple texturing for $\varepsilon = 0.5$

Effect of Dimple Area Density

Figures 4.5 (a) and 4.5 (b) illustrate the influence of dimple area density (S_p) on the non-dimensional load-carrying capacity (\bar{W}) under JFO boundary conditions, for spherical, cylindrical, and square texture geometries for both protrusion and dimple textured journal bearings, across various modified Reynolds numbers (Re^*) for a fixed eccentricity ratio of 0.5. It is observed that, for protrusion texturing, with the increase in the dimple area density the load-carrying capacity initially decreases and then increases for all the three

texture geometry. However, in the case of dimple texturing, the load-carrying capacity initially increases and then decreases, as dimple are density increases. Further, for both protrusion and dimple texturing, the load-carrying capacity decreases with increasing modified Reynolds numbers, a trend consistent with earlier observations. At $S_p = 0.15$, the minimum and maximum load-carrying capacity are observed for protrusion and dimple texturing respectively. Cylindrical texturing produces higher load-carrying capacity in the case of protrusion texturing, whereas square texturing is found to be producing more load-carrying capacity in the case of dimple texturing.

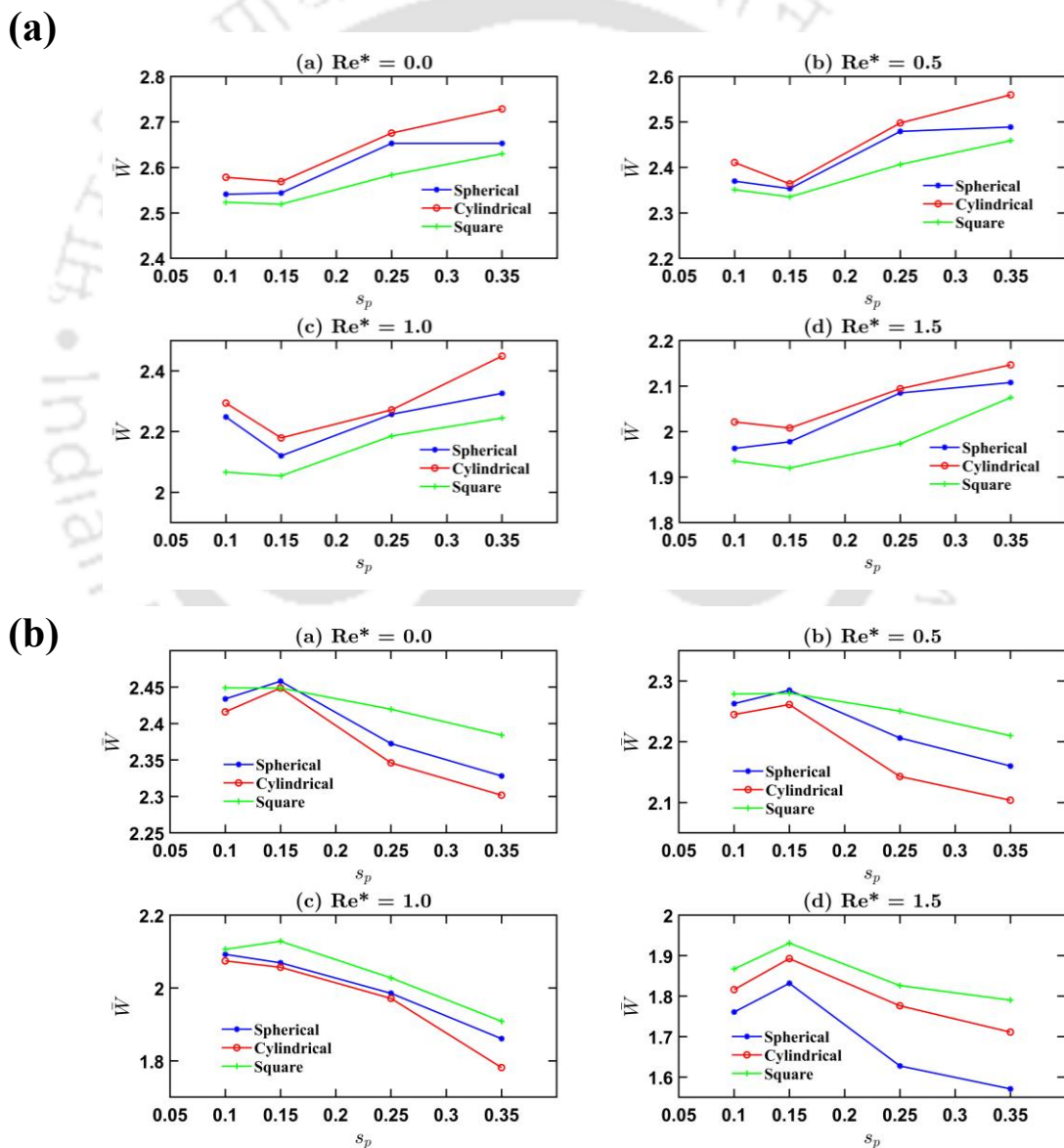


Fig. 4.5. Non-dimensional load-carrying capacity Vs Dimple area density for spherical, cylindrical and square texture with increasing inertia and JFO boundary conditions for (a) protrusion and (b) dimple texturing for $\varepsilon = 0.5$

4.4.2 Flow coefficient

Spherical Textured Bearing

The flow coefficient for Reynolds and JFO boundary conditions with increasing eccentricity ratio and modified Reynolds numbers for plain, spherical dimple textured and spherical protrusion textured bearing cases are shown in Figs. 4.6 (a), 4.6 (b) and 4.6 (c) respectively. A general trend observed across all cases is that the flow coefficient increases with increasing eccentricity ratio. This is expected, as higher eccentricity results in a thinner lubricant film on the loaded side, enhancing pressure buildup and flow through the converging wedge of the bearing. Importantly, the flow coefficients predicted using JFO boundary conditions are consistently lower than those estimated with Reynolds boundary conditions, with the exception at $\varepsilon = 0.1$, where cavitation effects are negligible. The protrusion textured bearing yields more flow compared to the plain bearing, whereas the dimple textured bearing gives less flow than the plain bearing. This observation is consistent with previous findings, such as those by Manser *et al.* [100], who reported that dimple texturing under JFO conditions resulted in a lower flow coefficient than a smooth bearing due to the cavitation boundary limiting fluid recirculation. Thus, one can say that the Reynolds boundary conditions lead to overestimating the flow coefficient because the end of the cavitation is not well defined.

When inertia is introduced, it has been found that the protrusion bearing produces more flow than the plain and dimple bearings under JFO boundary conditions, with dimple texturing giving the least amount of flow. The flow coefficient is found to be improving with increasing Re^* for $\varepsilon < 0.2$, with protrusion texturing showing the highest improvement. For $\varepsilon > 0.2$, the flow coefficient is reduced with increasing Re^* with a maximum reduction of 26.5% for DXT at $Re^* = 1.5$ and $\varepsilon = 0.4$. The improvement in flow coefficient for $\varepsilon < 0.2$ may be justified by the fact that at low eccentricity ratios, the textured surface can facilitate better distribution and flow of the lubricant.

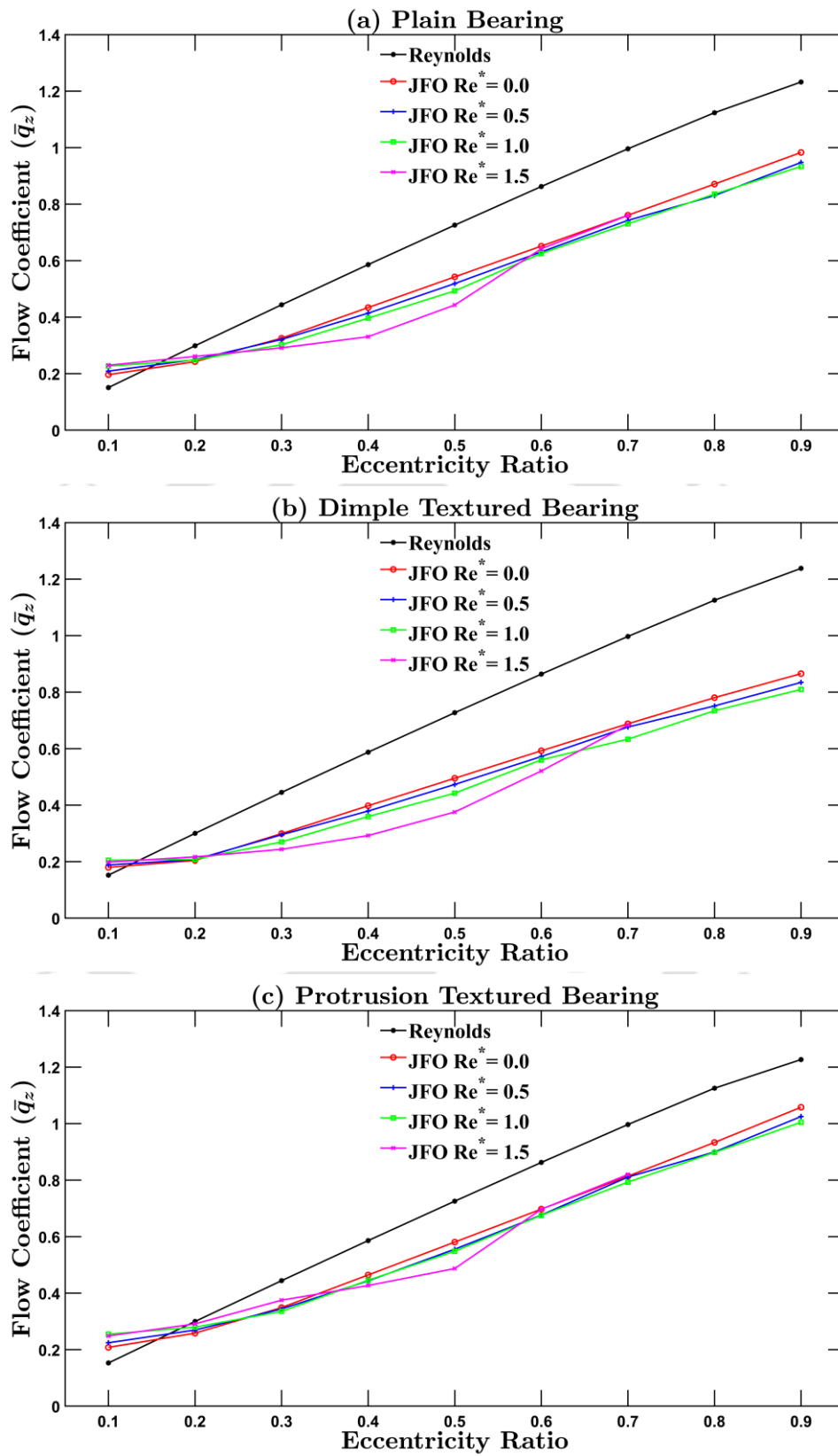


Fig. 4.6. Comparison of non-dimensional flow coefficient for Reynolds and JFO boundary conditions for (a) plain, (b) spherical dimple and (c) spherical protrusion textured bearing

Effect of Texture Geometry

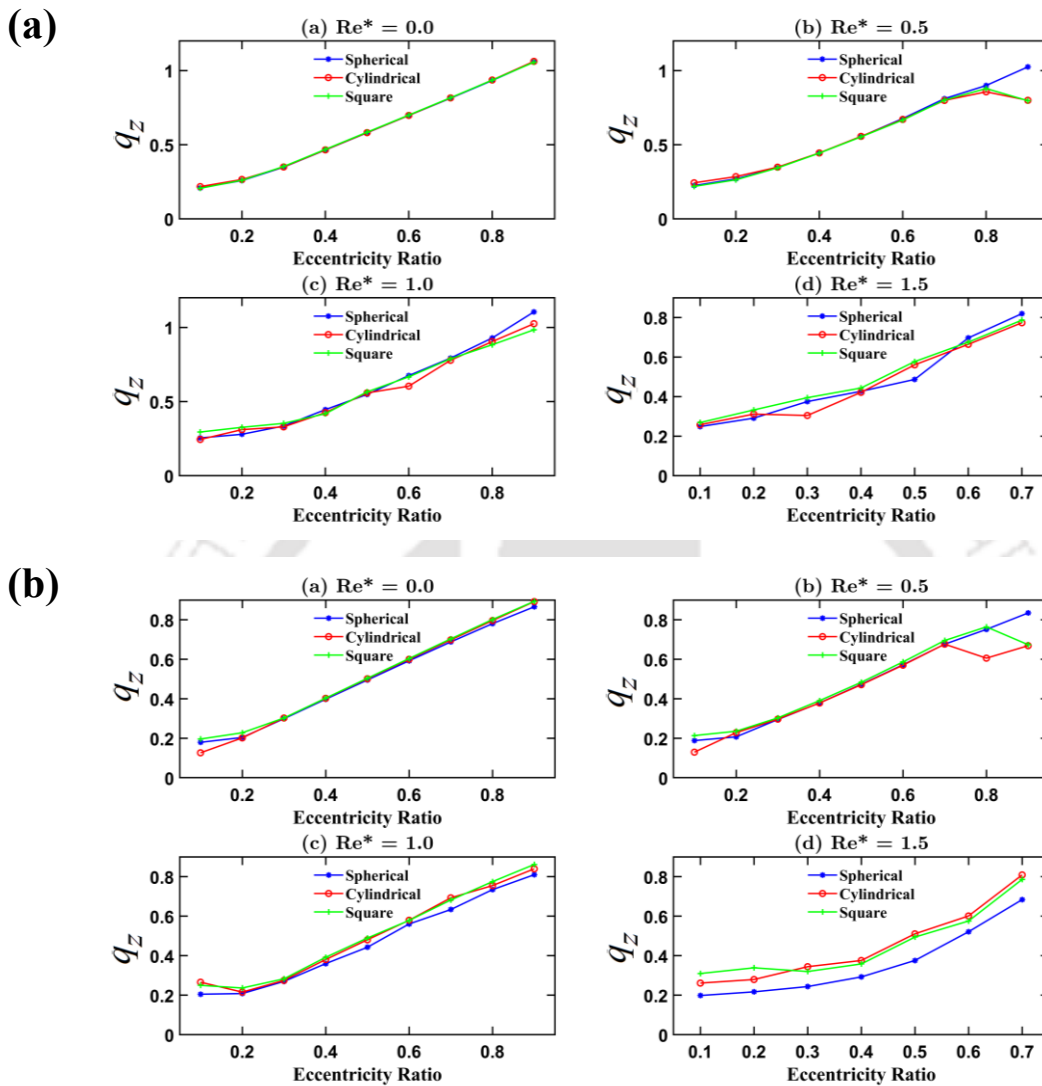


Fig. 4.7. Variation of non-dimensional flow coefficient with eccentricity ratio for spherical, cylindrical and square texture with increasing inertia and JFO boundary conditions for (a) protrusion and (b) dimple texturing

Figure 4.7 (a) and 4.7 (b) show the variation of flow coefficients for protrusion and dimple textured bearings with increasing eccentricity ratio (ε) and modified Reynolds number (Re^*). In both the cases, the flow coefficient increases with increasing eccentricity ratio, as the narrowing film gap enhances pressure buildup and lubricant transport. For protrusion textures, square texturing yields the highest flow coefficients at $Re^* = 1.0$ and 1.5 , particularly for $\varepsilon < 0.4$. However, the influence of inertia remains negligible, indicating flow is primarily driven by geometric effects. In the case of dimple texturing, square dimples also show superior flow performance under JFO conditions,

while cylindrical dimples show higher flow coefficients at $Re^* = 1.5$ and $\varepsilon > 0.3$. Overall, protrusion textures promote greater lubricant flow than dimples, which tend to trap fluid and limit transport, especially under higher inertia conditions.

Effect of Dimple Aspect Ratio

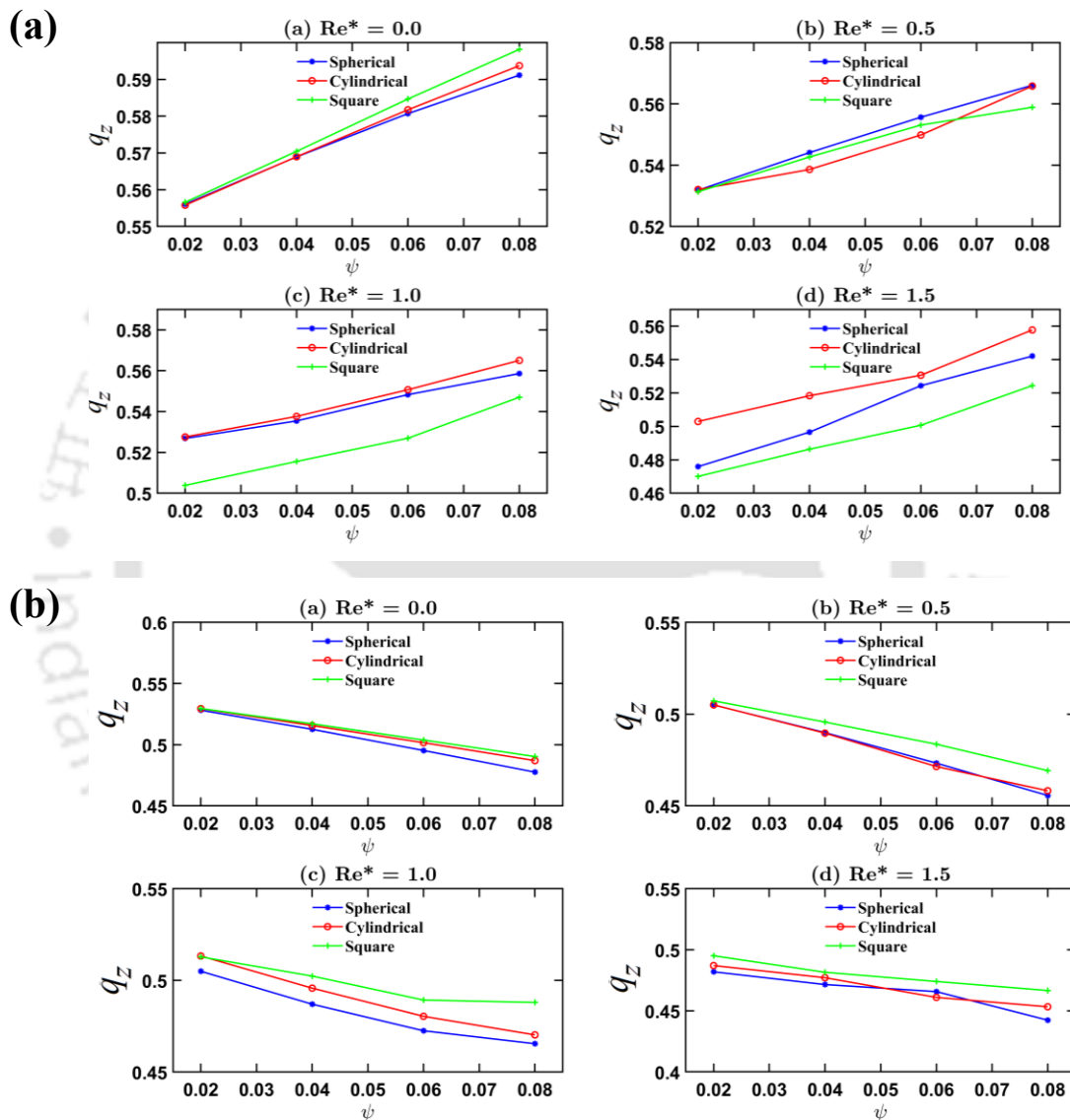


Fig. 4.8. Non-dimensional flow coefficient Vs Dimple aspect ratio for spherical, cylindrical and square texture with increasing inertia and JFO boundary conditions for (a) protrusion and (b) dimple texturing for $\varepsilon = 0.5$

The influence of dimple aspect ratio on the non-dimensional flow coefficient with increasing inertia effect under JFO boundary conditions for spherical, cylindrical and square texture for protrusion and dimple texturing are shown in Figs. 4.8 (a) and 4.8 (b) respectively. The value of eccentricity ratio has been fixed at 0.5. It is observed that the

flow coefficient increases with the increase in dimple aspect ratio in the case of protrusion texturing, whereas it decreases in the case of dimple texturing. Similar trend is observed for all the three texturing geometries and for the values of modified Reynolds numbers. Cylindrical protrusion texturing yields higher flow coefficients at high modified Reynolds numbers, whereas square dimple texturing gives higher flow coefficients across all modified Reynolds numbers.

Effect of Dimple Area Density

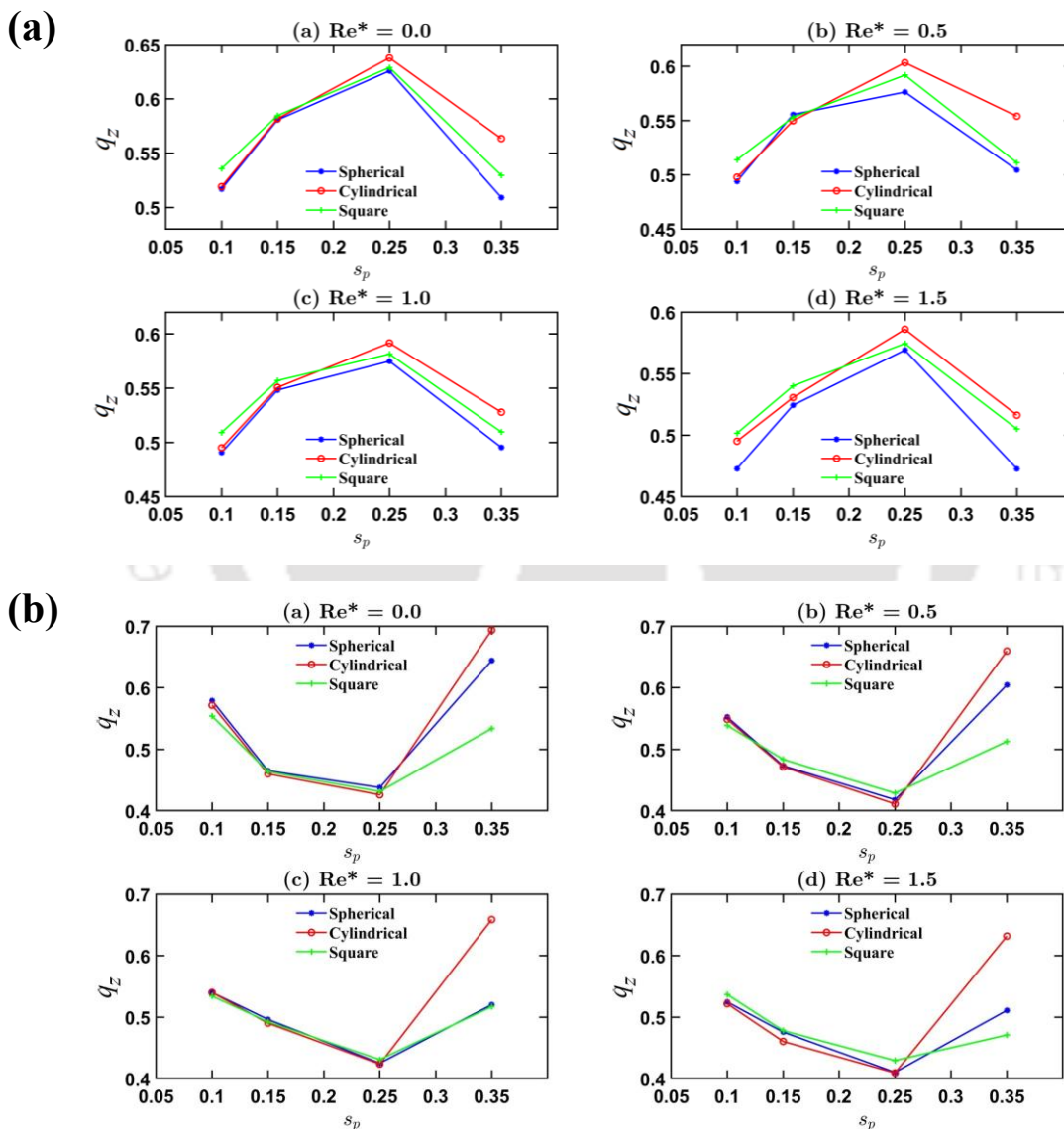


Fig. 4.9. Non-dimensional flow coefficient Vs Dimple area density for spherical, cylindrical and square texture with increasing inertia and JFO boundary conditions for (a) protrusion and (b) dimple texturing for $\varepsilon = 0.5$

Figures 4.9 (a) and 4.9 (b) illustrates the variation of flow coefficient (q_z) with increasing dimple area density (S_p) and modified Reynolds number (Re^*) for spherical, cylindrical, and square protrusion and dimple texturing respectively, under JFO boundary conditions. In the protrusion texturing, the flow coefficient decreases with increasing dimple area density (S_p) and modified Reynolds numbers (Re^*), until $S_p = 0.25$ with cylindrical texturing producing more flow coefficient at high modified Reynolds numbers ($Re^* = 1.5$). However, in the case of dimple texturing, the flow coefficient decreases with increasing dimple area density and modified Reynolds numbers, until $S_p = 0.25$. The opposite trends observed in flow coefficient variation for protrusion and dimple texturing with increasing dimple area density and modified Reynolds number may arise from the fundamental difference in how these textures interact with the lubricant flow. Dimple textures tend to trap the lubricant, and as S_p increases, more fluid becomes isolated within cavities, reducing the effective flow, especially under cavitation-aware JFO boundary conditions [100].

4.4.3 Friction variable

Spherical Textured Bearing

The variation of friction variable for Reynolds and JFO boundary condition with increasing eccentricity ratios and modified Reynolds numbers for plain, spherical dimple textured and spherical protrusion textured journal bearing is presented in Figs. 4.10 (a), 4.10 (b) and 4.10 (c) respectively. The friction variable decreases with the increasing eccentricity ratio. When inertia is neglected, *i.e.*, $Re^* = 0.0$, the JFO boundary conditions give lesser friction variables than the Reynolds boundary conditions, irrespective of the texturing configuration. With the increase in inertia, the friction variable increases slightly till $\varepsilon < 0.6$. When $\varepsilon \geq 0.6$, the plain, spherical dimple textured, and spherical protrusion textured bearings exhibit comparable frictional performance for all the values of the modified Reynolds number, and as such, friction variables are not much influenced by the texturing arrangement when JFO boundary conditions are used. Further, it is observed that the friction variables estimated for $\varepsilon = 0.1$, for all the cases of texturing and all the values of modified Reynolds number are significantly less in the case of JFO boundary conditions than in Reynolds boundary conditions.

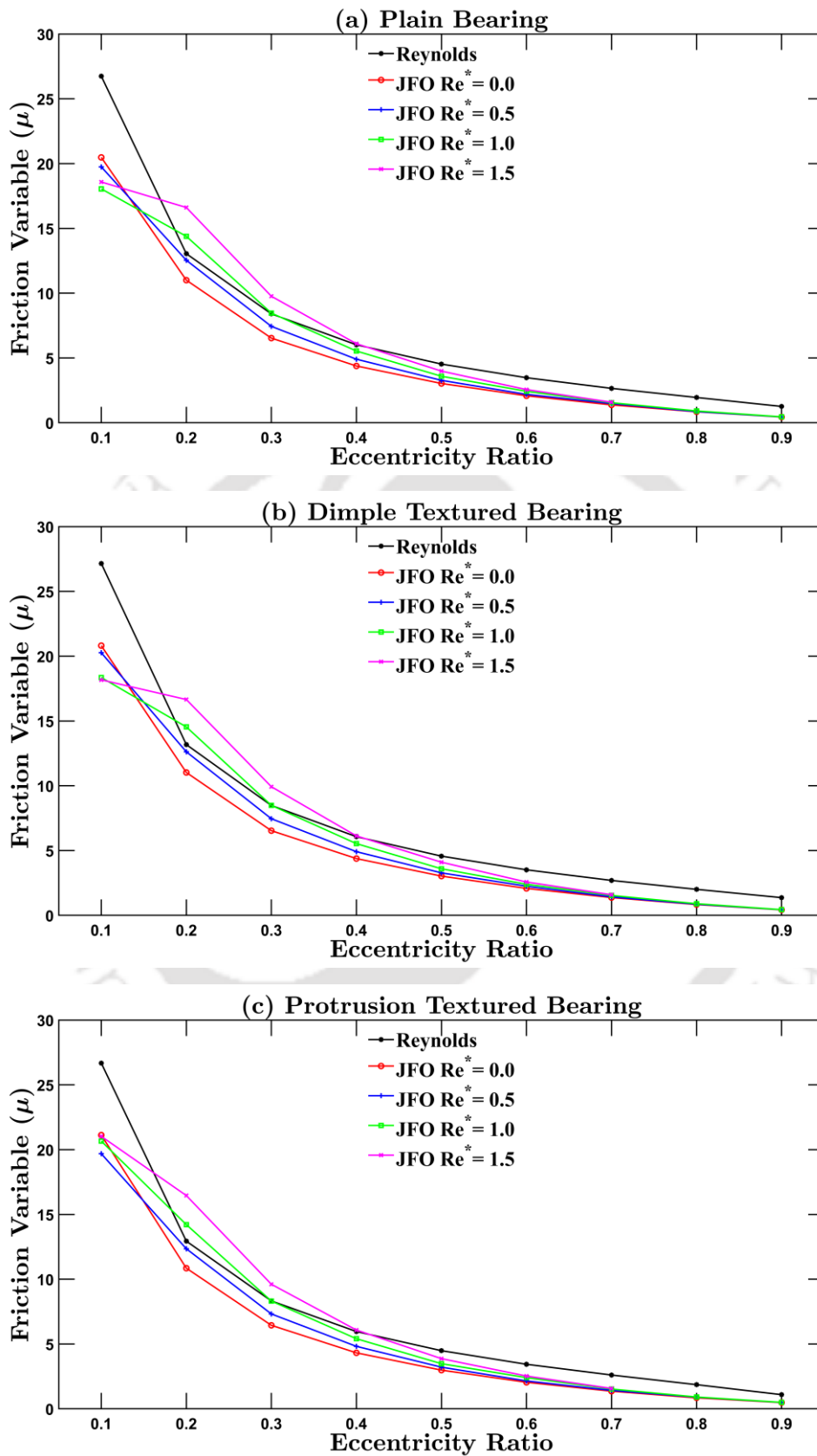


Fig. 4.10. Comparison of non-dimensional flow coefficient for Reynolds and JFO boundary conditions for (a) plain, (b) dimple and (c) protrusion textured bearing

Furthermore when $Re^* = 1.5$, particularly at low eccentricity ratios, the results are found to be erratic, which may be because of transition flow. However, these issues require further investigation.

Effect of Texture Geometry

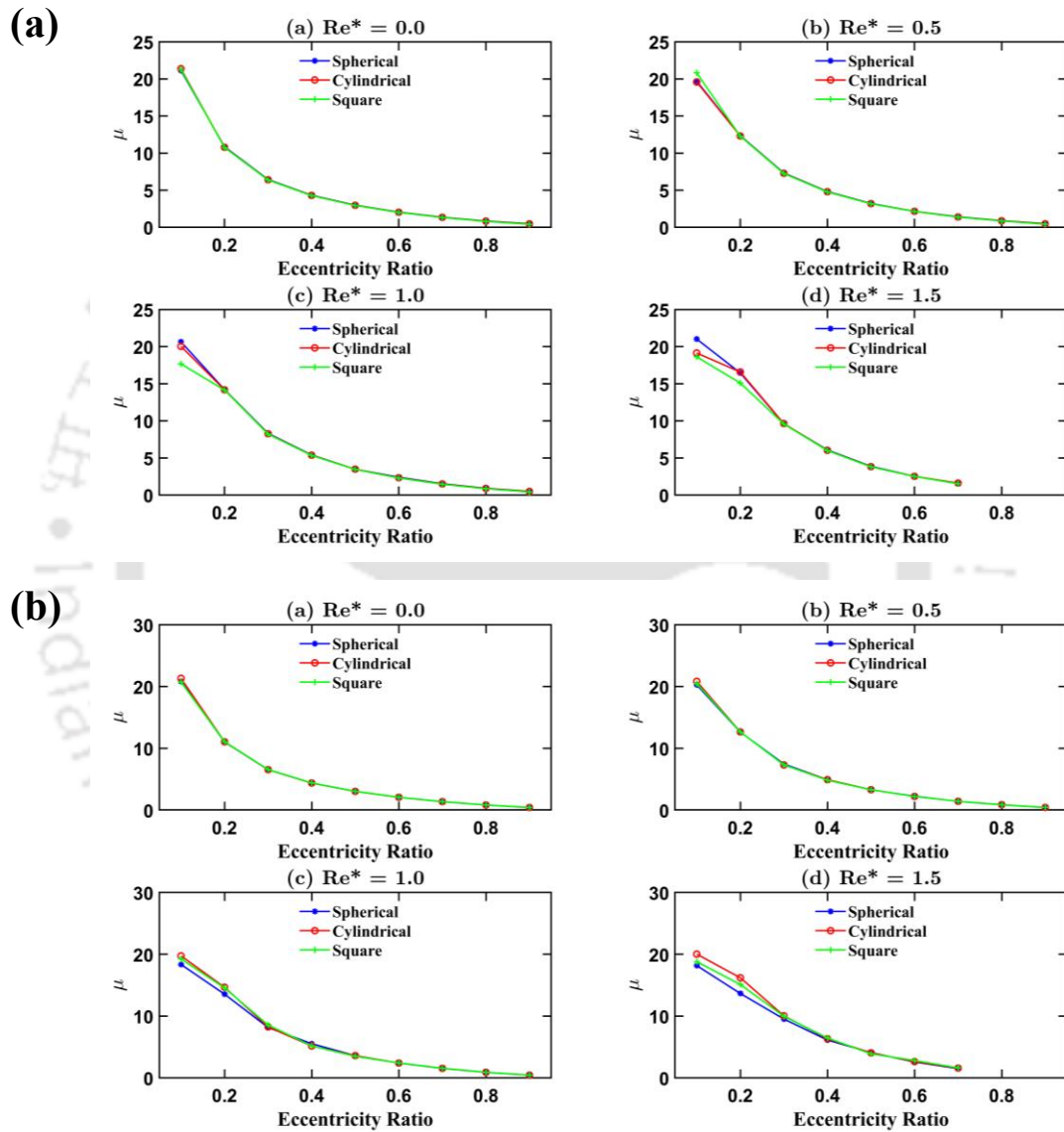


Fig. 4.11. Variation of friction variable for spherical, cylindrical and square texture with increasing inertia and JFO boundary conditions for (a) protrusion and (b) dimple texturing

The influence of surface texture geometry on the friction variable, as a function of increasing eccentricity ratio (ϵ) and modified Reynolds number (Re^*), is presented in Figs. 4.11(a) and 4.11(b) for protrusion and dimple textures, respectively. The results

indicate that the friction variable decreases with increasing eccentricity ratio for all three texture geometries – spherical, cylindrical, and square – and for both protrusion and dimple texturing. At relatively low modified Reynolds numbers ($Re^* = 0.0$ and 0.5), the variation in the friction variable due to changes in texture geometry is minimal for both protrusion and dimple texturing. However, for $Re^* = 1.0$ and 1.5 , the effect of texture geometry becomes more pronounced. In the case of protrusion texturing, square-shaped protrusions exhibit lower friction variable in comparison to spherical and cylindrical ones for $\varepsilon < 0.3$. In the case of dimple texturing, spherical dimples yield the lowest friction variable at higher Reynolds numbers for $\varepsilon < 0.3$.

These observations highlight the significance of tailoring texture geometry based on specific operating conditions. In particular, at higher modified Reynolds numbers, *i.e.*, when the effect of fluid inertia is dominant, a particular texture design, such as square protrusions or spherical dimples, can significantly enhance tribological performance by lowering frictional losses.

Effect of Dimple Aspect Ratio

The influence of dimple aspect ratio on the friction variable with increasing inertia effect under JFO boundary conditions for spherical, cylindrical and square texture for protrusion and dimple texturing are shown in Figs. 4.12 (a) and 4.12 (b) respectively. The value of eccentricity ratio has been fixed at 0.5. It is observed that, for dimple texturing, the friction variable remains nearly constant at low modified Reynolds numbers across all the values of dimple aspect ratio for each geometry, with spherical and cylindrical dimples yielding lower friction than square ones. As the Reynolds number increases, particularly at $Re^* = 1.5$, friction variable increases significantly, especially for cylindrical textures which show a sharp rise at higher dimple area density. In contrast, protrusion textures demonstrate a clear reduction in friction variable with increasing dimple aspect ratio for all the texture geometry and for all values of modified Reynolds numbers. However, the friction variable increases with the increase in modified Reynolds number. Square protrusion texturing has been found to be more effective at low inertia condition, whereas, for $Re^* = 1.5$, the cylindrical protrusion texturing produces lesser friction variables.

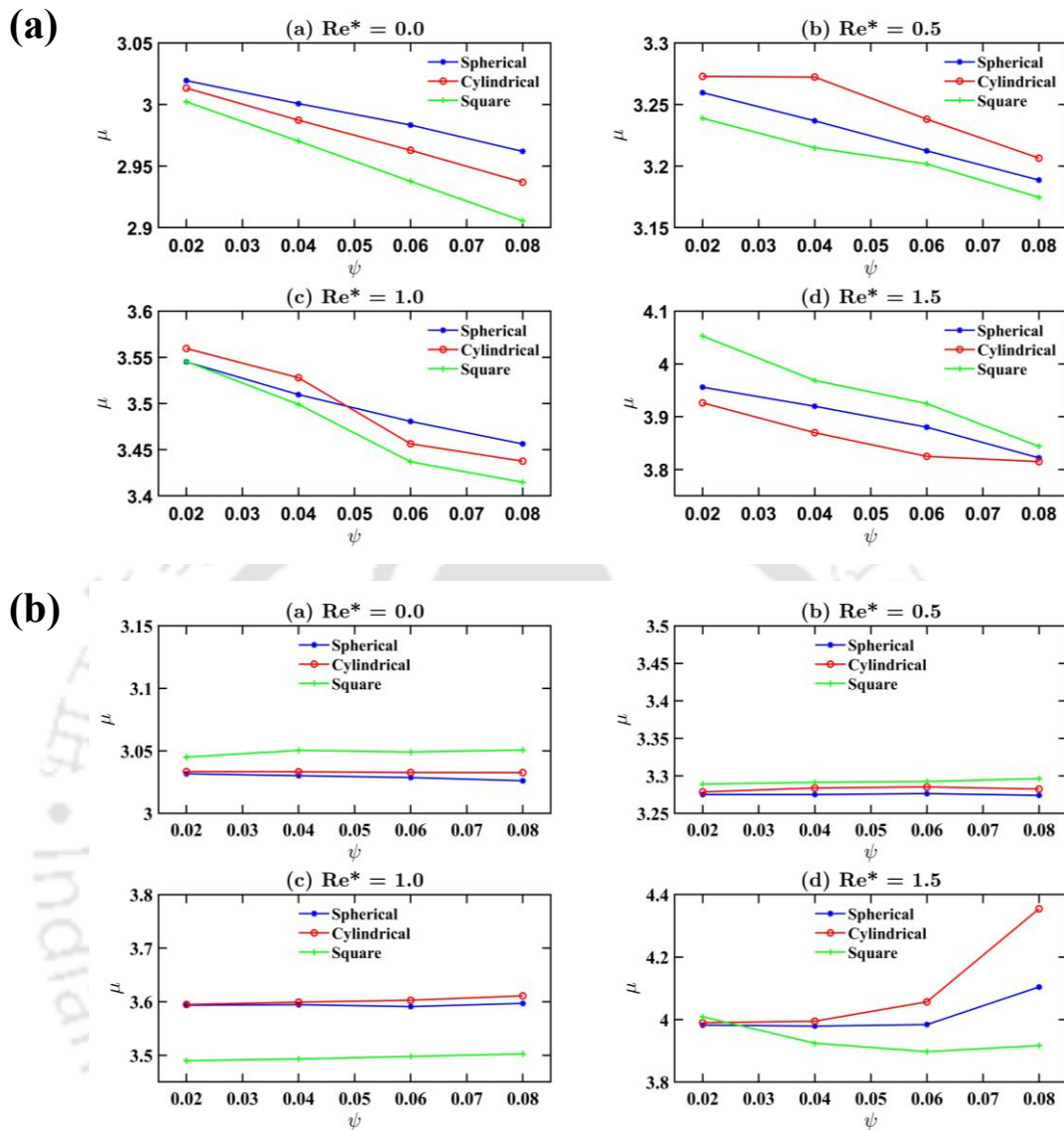


Fig. 4.12. Friction variable Vs Dimple aspect ratio for spherical, cylindrical and square texture with increasing inertia and JFO boundary conditions for (a) protrusion and (b) dimple texturing for $\varepsilon = 0.5$

Effect of Dimple Area Density

The variation of the friction variable (μ) with dimple area density (S_p) under different modified Reynolds numbers (Re^*) is presented for two texture types: protrusion and dimple texturing in Fig. 4.13 (a) and 4.13 (b) respectively. The value of eccentricity ratio has been fixed at 0.5.

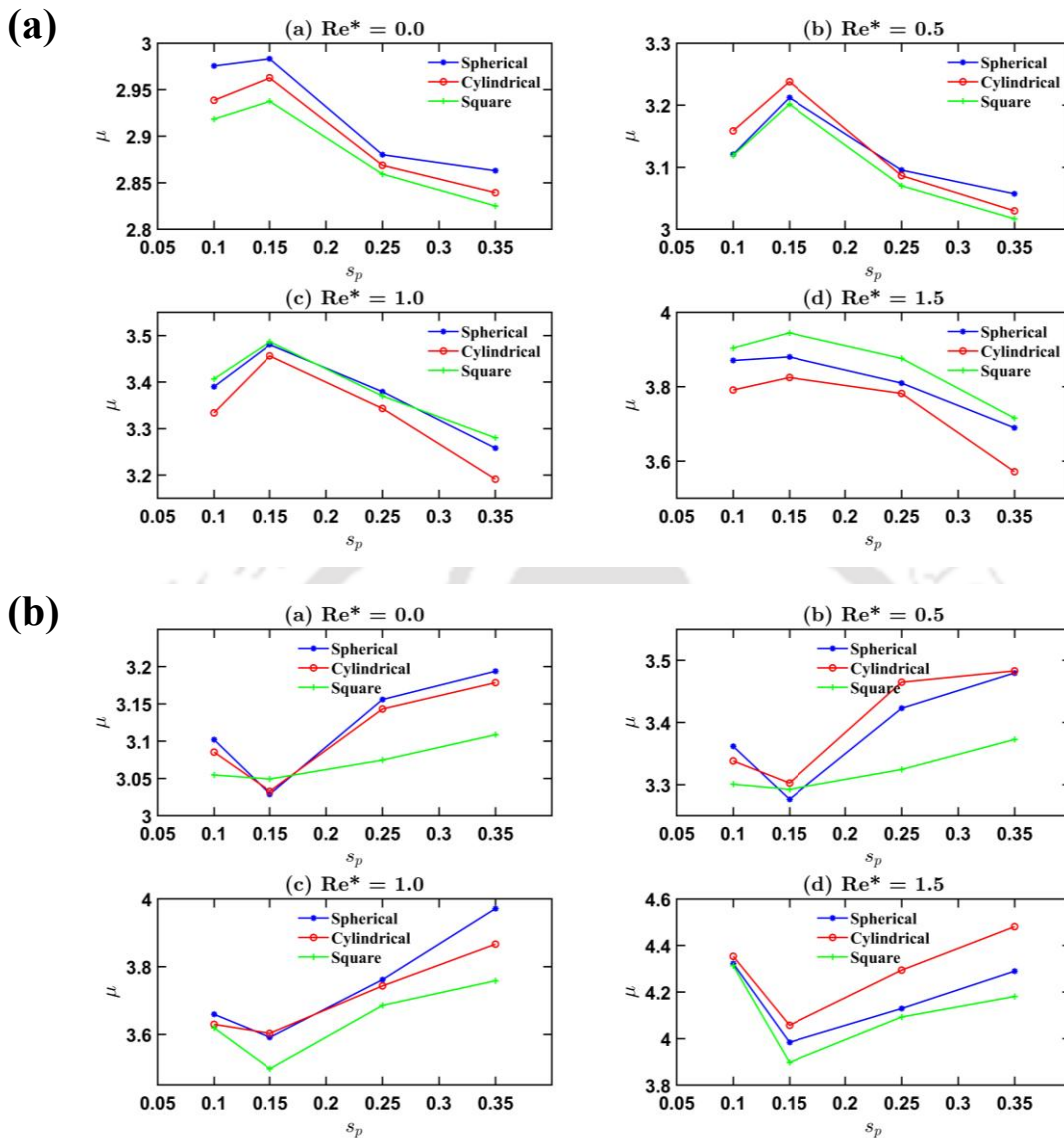


Fig. 4.13. Friction variable Vs Dimple area density for spherical, cylindrical and square texture with increasing inertia and JFO boundary conditions for (a) protrusion and (b) dimple texturing for $\varepsilon = 0.5$

The texturing geometries considered are spherical, cylindrical, and square. For protrusion texturing, friction variable initially increases with increasing dimple area density up to $S_p = 0.15$, and then decreases beyond this point for all geometries and Reynolds numbers. This may be due to the fact that at low dimple area density, protrusions behave primarily as surface roughness elements, increasing flow resistance and friction. As the dimple area density increases further, the protrusions begin to interact hydrodynamically, forming localized pressure zones and recirculation regions that contribute to load support, thereby reducing shear stress and friction variable. Cylindrical

texturing produces lesser friction variable. Conversely, for dimple textures, friction variable initially decreases with increasing dimple area density, reaching a minimum around $S_p = 0.15$, followed by a gradual increase as dimple area density increases. Further, it is observed that increasing the modified Reynolds number consistently results in increase in the friction variable for both protrusion and dimple texturing. Thus, the behaviour of the friction variable (μ) is strongly influenced by the interplay between texture geometry, the texturing parameters (ψ and S_p), and fluid inertia effect.

4.5 Summary

This chapter presents a numerical investigation into the combined influence of cavitation and lubricant inertia on the steady-state performance of textured journal bearings, considering protrusion, dimple, and plain configurations. Cavitation is incorporated using Jacobson-Floberg-Olsen (JFO) boundary conditions. A novel modified Reynolds equation is formulated, incorporating both the lubricant inertia effect and the mass-conserving (JFO) boundary conditions. The Progressive Mesh Densification (PMD) method is employed for efficient computation. The texturing geometries considered are spherical, cylindrical and square texture. Key performance parameters – non-dimensional load-carrying capacity (LCC), flow coefficient, and friction variable – are evaluated across varying eccentricity ratios and modified Reynolds numbers. Results show that JFO conditions yields higher load-carrying capacity compared to Reynolds boundary conditions, especially for eccentricity ratios above 0.4, with protrusion texturing outperforming dimple and plain configuration. Flow coefficients are generally lower under JFO boundary conditions, but inertia increases them for eccentricity ratios ≤ 0.2 . Friction variables are consistently lower under JFO boundary conditions, though inertia slightly increases the friction variable at lower eccentricity ratios. Texturing configuration has minimal influence on friction variables under the JFO boundary conditions.

The next chapter focuses on the stability analysis of textured journal bearings, incorporating the effects of lubricant inertia to assess the dynamic behaviour of the system under various operating conditions.



Chapter 5

Stability Analysis of Textured Journal Bearing Considering Lubricant Inertia Effect

Contents

Stability Analysis of Textured Journal Bearing Considering Lubricant Inertia Effect	103
5.1 Introduction	105
5.2 Methodology	105
5.3 Stability Analysis of Textured Journal Bearing Considering Lubricant Inertia Effect	106
5.3.1 Effects of non-dimensional clearance (δ) on bearing stability	109
5.3.2 Effects of dimple aspect ratio (ψ) on bearing stability	111
5.3.3 Effects of dimple area density (S_p) on bearing stability	114
5.4 Summary	118



5.1 Introduction

The effect of lubricant inertia and cavitation on the steady-state characteristics of textured journal bearings was discussed in the previous chapter, providing valuable insights into their performance under various operating conditions. Building on these findings, the current chapter shifts focus to the stability analysis of textured journal bearings. The stability of journal bearings is critical for ensuring smooth operation and longevity of rotating machinery. While lubricant inertia effects are often neglected in stability analyses, they become significant at high operating speeds and with low-viscosity lubricants. This chapter presents a nonlinear transient analysis of textured journal bearings, explicitly incorporating lubricant inertia effects. Plain bearings, spherical protrusions and spherical dimple textures are investigated, and critical mass parameters and whirl ratios are evaluated by varying the texture parameters across different eccentricity ratios. The influence of lubricant inertia is assessed by varying the modified Reynolds number. The boundary conditions applied here are the Reynolds boundary conditions. One might suggest the use of Jakobsson-Floberg-Olsen (JFO) boundary conditions to treat the cavitation occurring in the journal bearing. In this regard, it is worth mentioning that, an attempt was made to implement the JFO boundary conditions in the nonlinear transient analysis of textured journal bearings. However, the convergence issue could not be overcome with the available resources. Nevertheless, it has also been reported that the variation in the results for mass-conserving boundary conditions and non-mass-conserving boundary conditions is negligible when a dense mesh is used [89]. In view of this, it is presumed that the Reynolds boundary conditions are sufficient to treat the cavitation appropriately for stability analysis.

5.2 Methodology

As discussed in section 2.2.6 in chapter 2, the stability analysis of journal bearings is carried out by the nonlinear transient analysis method. Solving equations (2.49) and (2.50), the values of ε , ϕ , $\dot{\varepsilon}$ and $\dot{\phi}$ are estimated. For a given value of the mass parameter (\bar{M}), which is a function of rotational speed, the trajectory of the journal centre is determined by plotting the attitude angle (ϕ) against the eccentricity ratio (ε) at each time step, thereby capturing the position of the journal at various time steps. By

observing these trajectories, it is possible to determine whether the rotor is in stable, unstable or critically stable condition.

5.3 Stability Analysis of Textured Journal Bearing Considering Lubricant Inertia Effect

Based on the methodology discussed in the previous section, a MATLAB code has been developed. The trajectory of the bearing centre is traced for different mass parameters (\bar{M}), and the stability of the bearing is checked.

A bearing is considered stable if the trajectory spirals inwards and regains its equilibrium position. However, the bearing is said to be unstable if this trajectory grows continuously, tending to reach the clearance circle. If the journal centre trajectory keeps spiralling in a loop, the bearing is said to be in critically stable condition. The process is repeated for different values of mass parameters (\bar{M}) until the trajectories for critically stable conditions are obtained and the values of the corresponding critical mass parameters (\bar{M}_c) and critical whirl ratios are recorded.

Figures 5.1, 5.3 and 5.5 show the journal trajectory for stable, critically stable and unstable conditions, respectively, for a textured journal bearing for $L/D = 1.0$, $\varepsilon = 0.5$ and $Re^* = 1.0$. Whereas the corresponding horizontal and vertical displacement for Figs. 5.1, 5.3 and 5.5 are shown in Figs. 5.2, 5.4 and 5.6, respectively. The texturing parameters pertaining to the above cases are dimple area density = 0.15, dimple aspect ratio = 0.06 and non-dimensional clearance = 0.15. The critical orbit of the journal has been found when the mass-parameter value is 7.9. When the value of the mass parameter is less than 7.9, a stable orbit is obtained, whereas when the mass parameter is more than 7.9, the journal becomes unstable. The displacement plots in Figures 5.2, 5.4, and 5.6 further corroborate these findings. In Figure 5.2 (stable condition), both horizontal and vertical displacements gradually diminish over time and converge toward a steady-state position. In Figure 5.4 (critically stable condition), the displacements oscillate with constant amplitude, indicating marginal stability. Figure 5.6 (unstable condition) shows displacements that grow progressively with time, indicating that the system is unable to return to equilibrium, consistent with the outward spiral observed in the trajectory plot.

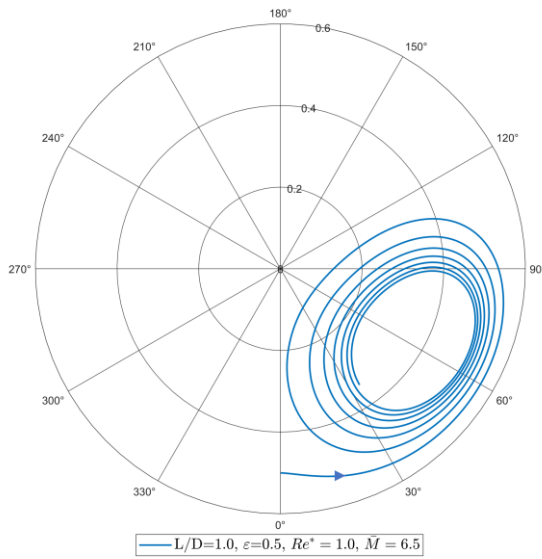


Fig. 5.1. Stable trajectory of journal centre for protrusion texturing for $\delta = 0.15, \psi = 0.06, s_p = 0.15, \bar{M} = 6.5$

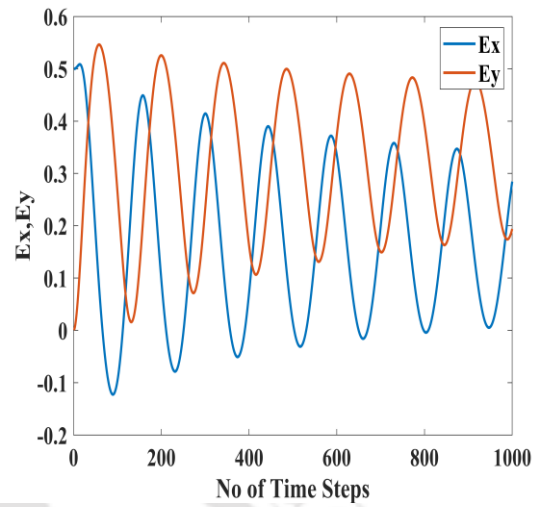


Fig. 5.2. Horizontal and Vertical displacement of journal centre Vs. time for $\delta = 0.15, \psi = 0.06, s_p = 0.15, \bar{M} = 6.5$

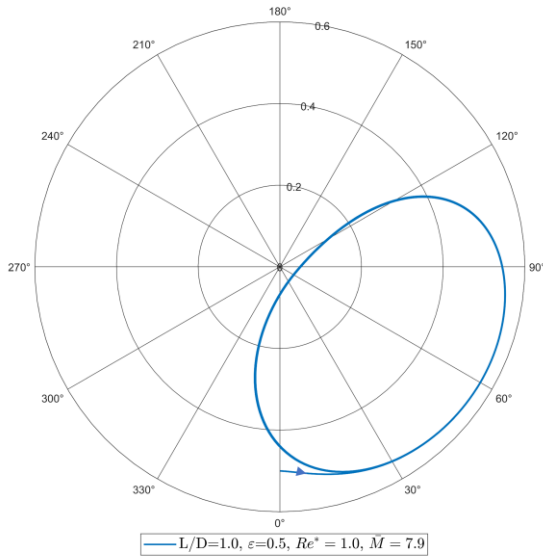


Fig. 5.3. Critically stable trajectory of journal centre for protrusion texturing for $\delta = 0.15, \psi = 0.06, s_p = 0.15, \bar{M} = 7.9$

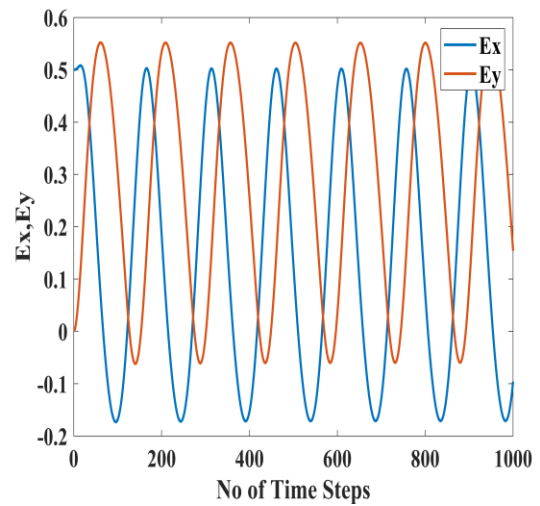


Fig. 5.4. Horizontal and Vertical displacement of journal centre Vs. time for $\delta = 0.15, \psi = 0.06, s_p = 0.15, \bar{M} = 7.9$

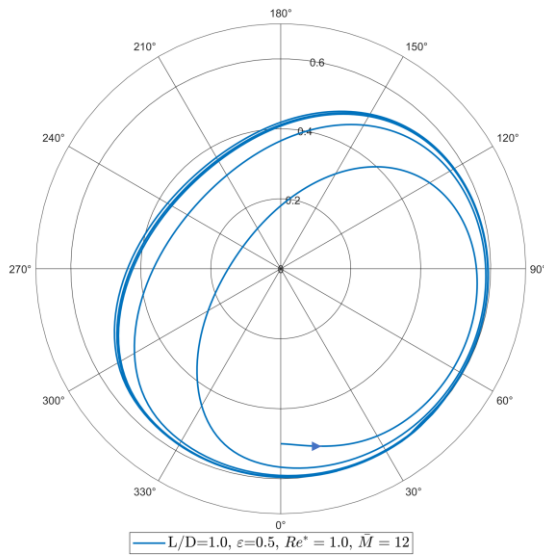


Fig. 5.5. Unstable trajectory of journal centre for protrusion texturing for $\delta = 0.15, \psi = 0.06, s_p = 0.15, \bar{M} = 12$

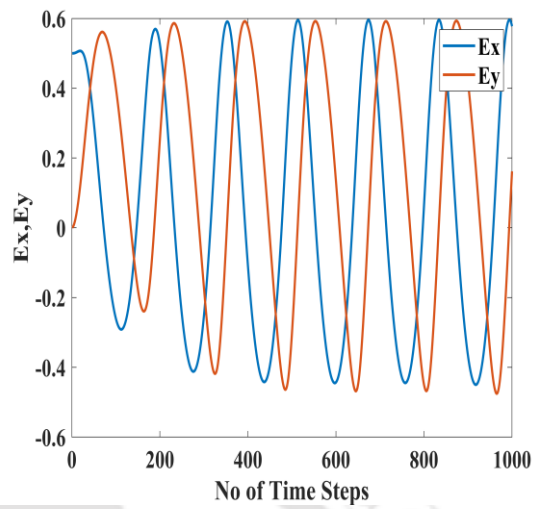


Fig. 5.6. Horizontal and Vertical displacement of journal centre Vs. time for $\delta = 0.15, \psi = 0.06, s_p = 0.15, \bar{M} = 12$

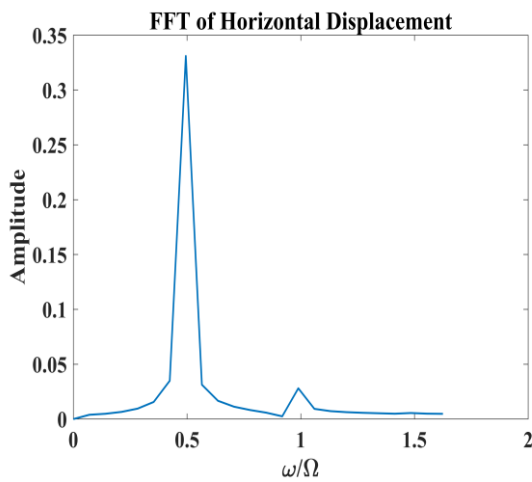


Fig. 5.7. FFT-spectrum of critical horizontal displacement for $\delta = 0.15, \psi = 0.06, s_p = 0.15, \bar{M} = 12$

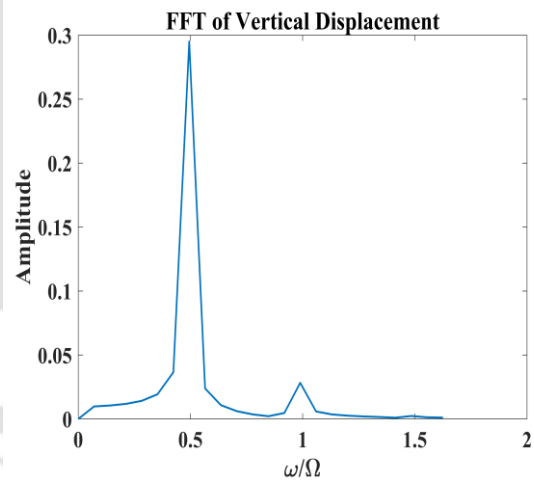


Fig. 5.8. FFT-spectrum of critical vertical displacement for $\delta = 0.15, \psi = 0.06, s_p = 0.15, \bar{M} = 12$

Figures 5.7 and 5.8 present the FFT spectrum of horizontal and vertical displacement of the rotor for the critically stable conditions of Figs. 5.3 and 5.4. It is observed that the peak is located at whirl ratio ($\bar{\omega} = \omega/\Omega$) 0.47, which is the critical value of the whirl ratio corresponding to the critical mass-parameter value of 7.9. Stability maps

for various operating conditions and texture geometries are presented in the following sections. These maps are constructed by plotting the critical mass parameters and the corresponding whirl ratios against the eccentricity ratios. It should be noted that the regions to the right and below the mass-parameter curves represent the stable operating zones, while the regions to the left and above the curves indicate instability.

5.3.1 Effects of non-dimensional clearance (δ) on bearing stability

The influence of non-dimensional clearance ($\delta = C/2r_p$) on the stability of dimple, plain and protrusion textured journal bearings is shown in Figs. 5.9, 5.10, 5.11 and 5.12 for $\delta = 0.10, 0.15, 0.25, 0.55$, respectively, for increasing eccentricity ratios and modifying Reynolds numbers 0.0, 0.5, 1.0 and 1.5. It is observed that, for all the cases, the critical mass parameter initially decreases as the eccentricity ratio increases, indicating that the system becomes less stable as the eccentricity ratio increases. The mass parameter, however, starts to increase after a certain value of the eccentricity ratio, implying a stabilization effect at higher eccentricity ratios. This is in line with the notion that stability is an issue for lightly loaded bearings.

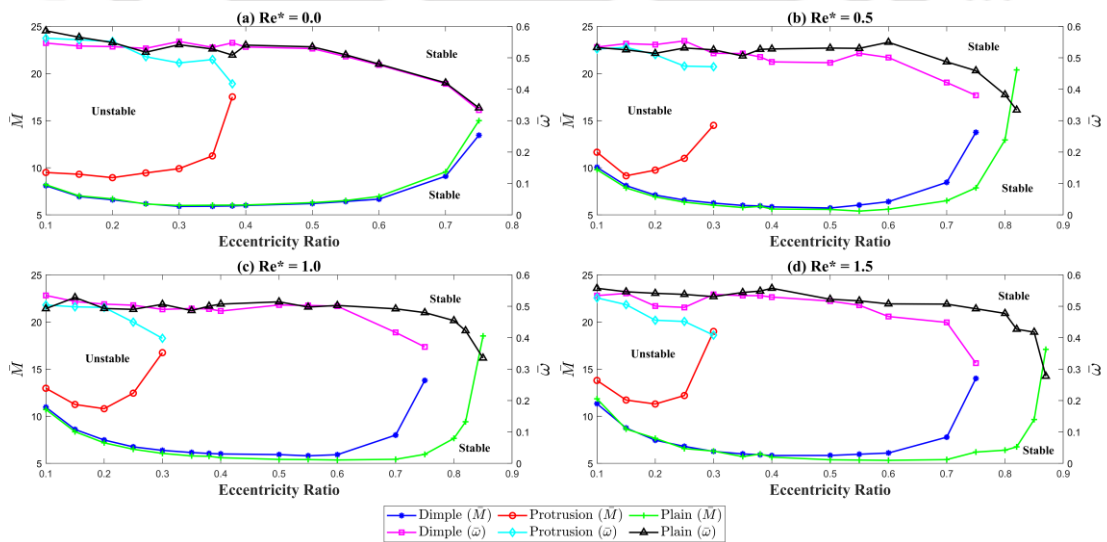


Fig. 5.9. Stability Map for $L/D = 1.0$, $\delta = 0.10$, $\psi = 0.06$, $S_p = 0.15$

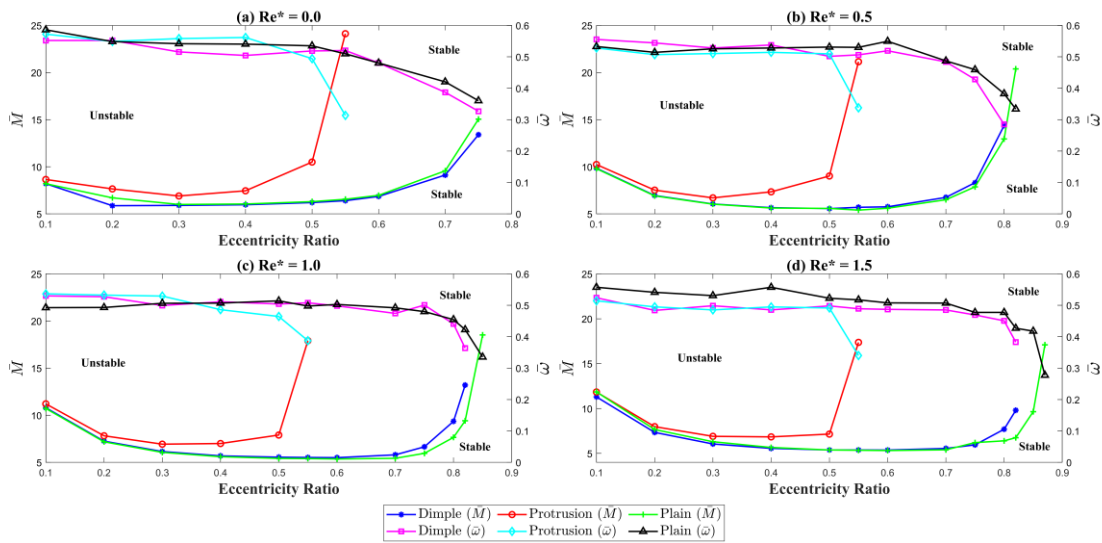


Fig. 5.10. Stability Map for $L/D = 1.0$, $\delta = 0.15$, $\psi = 0.06$, $S_p = 0.15$

From Fig. 5.9, it is observed that, when $\delta = 0.10$, the increase in modified Reynolds numbers results in the increased stability regime for dimple, plain and protrusion texturing. The same trend can be observed for $\delta = 0.15$ in Fig. 5.10. The protrusion texturing exhibits better stability than dimple and plain bearings for $\delta = 0.10$ and $\delta = 0.15$. It is likely that the protrusions introduce localized pressure build-up and increased resistance to lateral rotor displacement, which contributes to higher stiffness and damping coefficients – factors essential for suppressing instability.

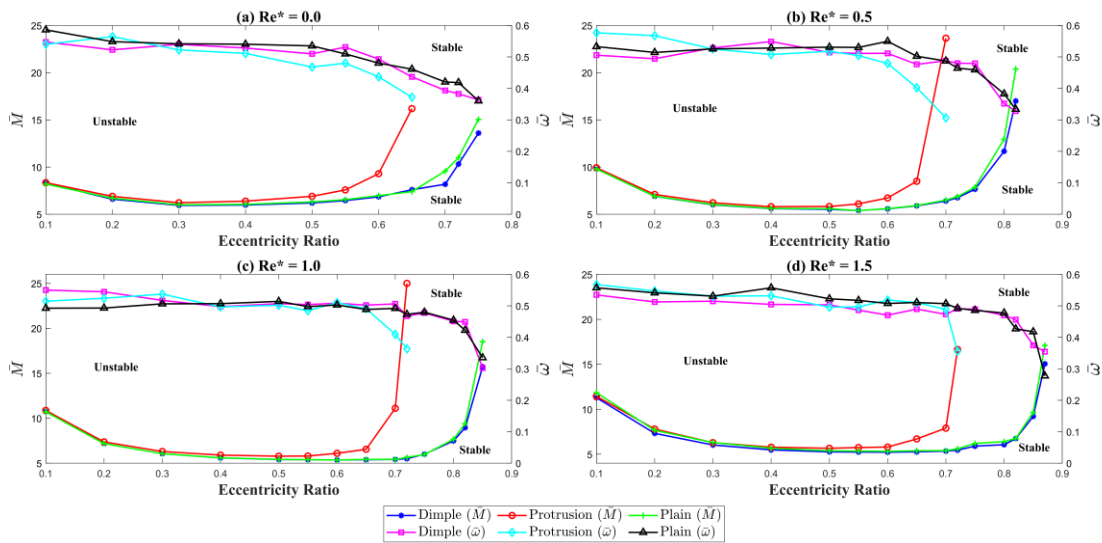


Fig. 5.11. Stability Map for $L/D = 1.0$, $\delta = 0.25$, $\psi = 0.06$, $S_p = 0.15$

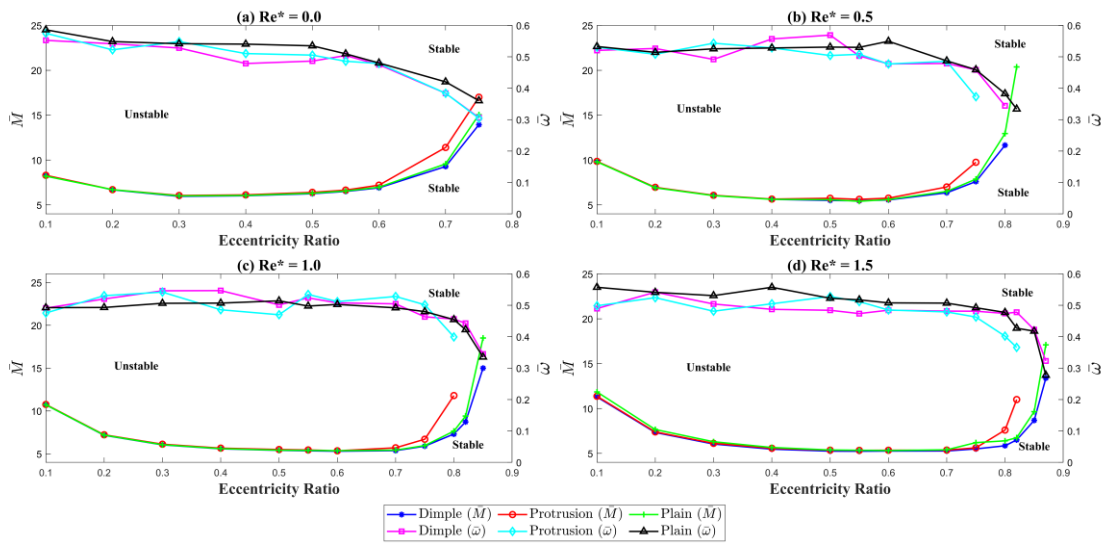


Fig. 5.12. Stability Map for $L / D = 1.0$, $\delta = 0.55$, $\psi = 0.06$, $S_p = 0.15$

When $\delta = 0.25$, the stability regime for protrusion bearing decreases than $\delta = 0.10$ and $\delta = 0.15$, as shown in Fig. 5.11. When $\delta = 0.55$, from Fig. 5.12, it is observed that the texturing configuration has little effect, as similar stability regimes have been observed for all three cases. Similar results are reported by Zhang and Xu [117] for adjustable journal bearings, where they reported improved stability of the bearings at reduced clearance. Further, the effect of lubricant inertia increases the stability for lightly loaded bearings, whereas the effect of lubricant inertia deteriorates the stability for moderately and heavily loaded bearings except at $\delta = 0.10$ and 0.15 for all the cases of texturing. Thus, it may be concluded that low non-dimensional clearance enhances the effectiveness of surface texturing – particularly for protrusion texturing, in improving the stability of journal bearings.

The whirl ratio, in all the figures, lies in the range of 0.5, which signifies the half-frequency whirl, a characteristic of hydrodynamic journal bearing. At a high eccentricity ratio, the whirl ratio falls to smaller values, indicating that the bearing is always stable at high eccentricity ratios.

5.3.2 Effects of dimple aspect ratio (ψ) on bearing stability

The influence of dimple aspect ratio ($\psi = h_p / 2r_p$) on the stability of dimple, plain and protrusion textured journal bearings is shown in Figs. 5.13, 5.14, 5.15 and 5.16 for

$\psi = 0.02, 0.04, 0.06, 0.08$, respectively, for increasing eccentricity ratios and modifying Reynolds numbers 0.0, 0.5, 1.0 and 1.5.

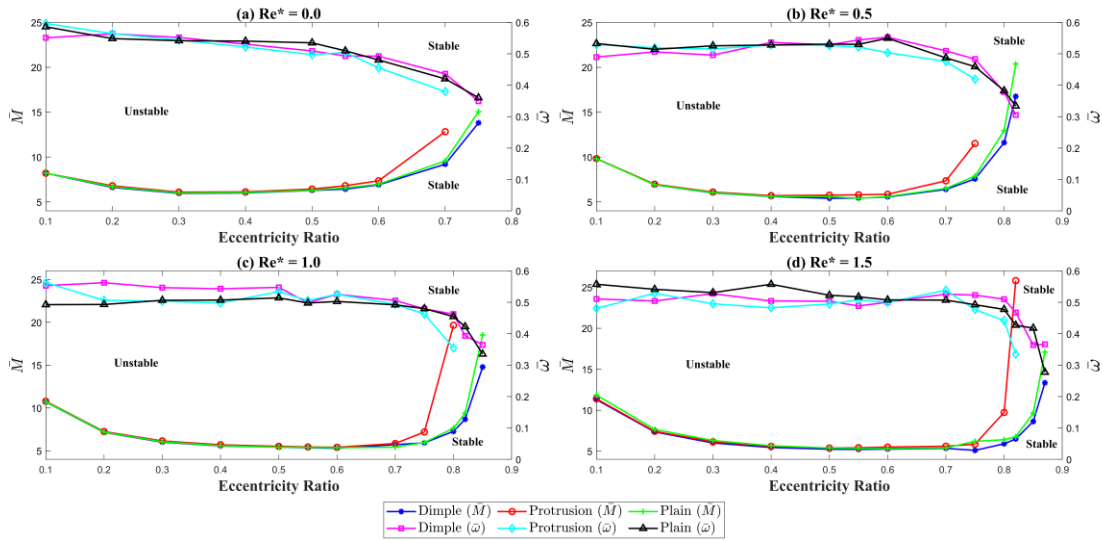


Fig. 5.13. Stability Map for $L/D = 1.0$, $\psi = 0.02$, $\delta = 0.15$, $S_p = 0.15$

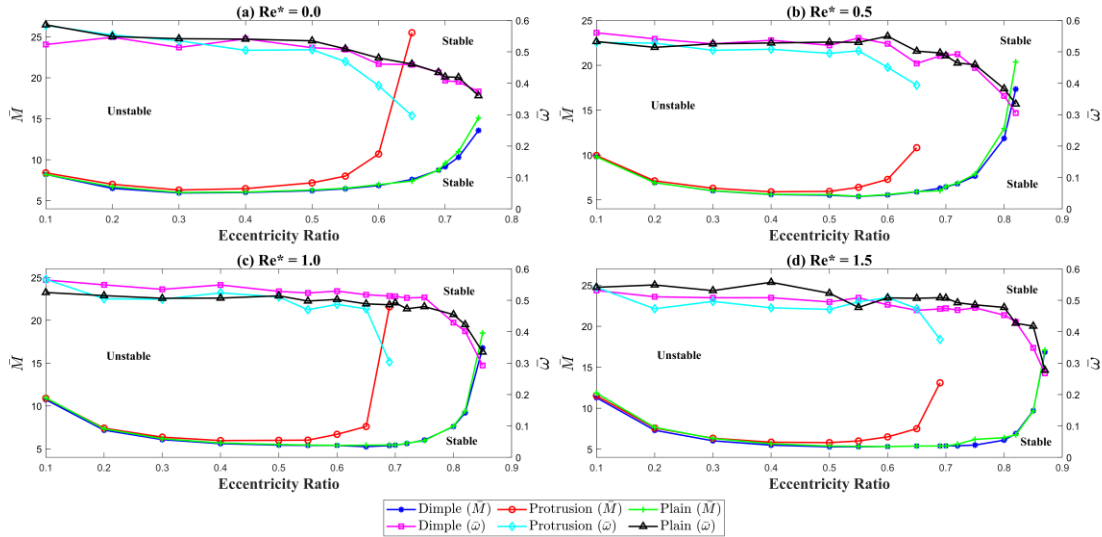


Fig. 5.14. Stability Map for $L/D = 1.0$, $\psi = 0.04$, $\delta = 0.15$, $S_p = 0.15$

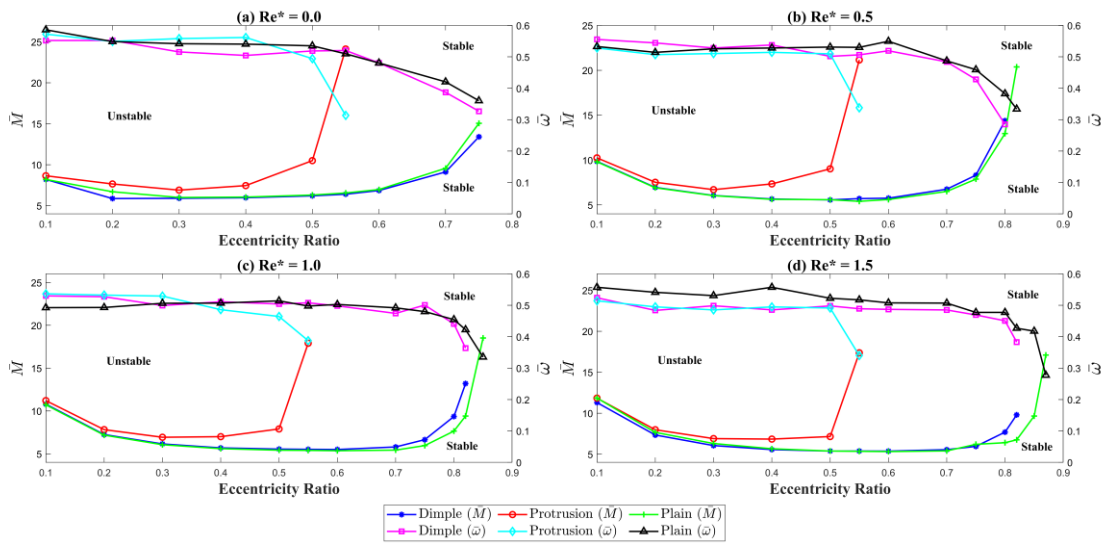


Fig. 5.15. Stability Map for $L / D = 1.0$, $\psi = 0.06$, $\delta = 0.15$, $S_p = 0.15$

From Fig. 5.13, it is observed that the dimple, protrusion and plain bearing exhibit similar stability regimes and the effect of the increase in inertia is insignificant except for heavily loaded bearings when $\psi = 0.02$. This behaviour suggests that at a low aspect ratio; the texture depth is insufficient to significantly perturb the pressure field or enhance hydrodynamic effects in a meaningful way. At high eccentricity ratios and for high modified Reynolds numbers, the protrusion texturing is found to be more stable than dimple and plain bearings. This improvement can be attributed to the geometric resistance offered by the protrusions, which act as micro-barriers, generating localized pressure zones and resisting rotor displacement more effectively than the shallow dimples or plain surfaces. The stability regime for protrusion texturing increases, whereas the stability regimes for plain and dimple texturing aren't affected for $\psi = 0.04$ and $\psi = 0.06$, as shown in Figs. 5.14 and 5.15. The increase in modified Reynolds numbers improves the stability of lightly loaded bearings, whereas the stability of heavily loaded bearings is adversely affected by the increase in lubricant inertia.

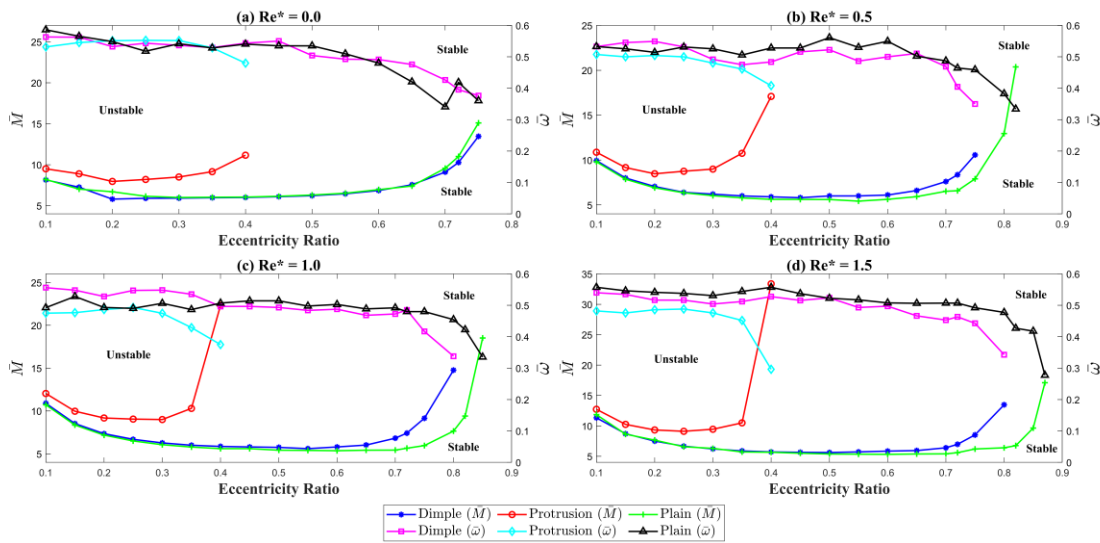


Fig. 5.16. Stability Map for $L / D = 1.0$, $\psi = 0.08$, $\delta = 0.15$, $S_p = 0.15$

With further increase in the dimple aspect ratio, $\psi = 0.08$, the stability of protrusion texturing improves for lightly loaded bearings for all values of modified Reynolds numbers. It is observed, from Fig. 5.16, that the protrusion texturing becomes more stable than plain and dimple texturing when $\varepsilon > 0.3$. Singh and Awasthi [76] also observed similar results in their analysis, of course without considering the inertia effect, for textured journal bearings, where they reported enhanced stability with increasing dimple depth, a parameter similar to dimple aspect ratio. Furthermore, contrary to the earlier cases of dimple aspect ratios, for $\psi = 0.08$, the increase in modified Reynolds number increases the stability of the bearings for protrusion texturing when $\varepsilon > 0.3$. Thus, the dimple aspect ratio (ψ) is a key parameter influencing the effectiveness of surface texturing in improving the stability of journal bearings. At lower aspect ratios, the impact of texturing on stability is minimal, offering little to no advantage over plain surfaces. However, as the dimple aspect ratio increases, protrusion textures demonstrate a significant improvement in stability compared to both plain and dimple textured bearings. Moreover, the interplay between texture geometry and lubricant inertia becomes increasingly relevant at higher aspect ratios.

5.3.3 Effects of dimple area density (S_p) on bearing stability

The influence of dimple area density ($S_p = \pi r_p^2 / 4 r_1^2$) on the stability of dimple, plain and protrusion textured journal bearings for increasing eccentricity ratios and modified

Reynolds numbers are shown in Figs. 5.17, 5.18, 5.19, 5.20 and 5.21 for $S_p = 0.10, 0.15, 0.25, 0.35, 0.50$ respectively.

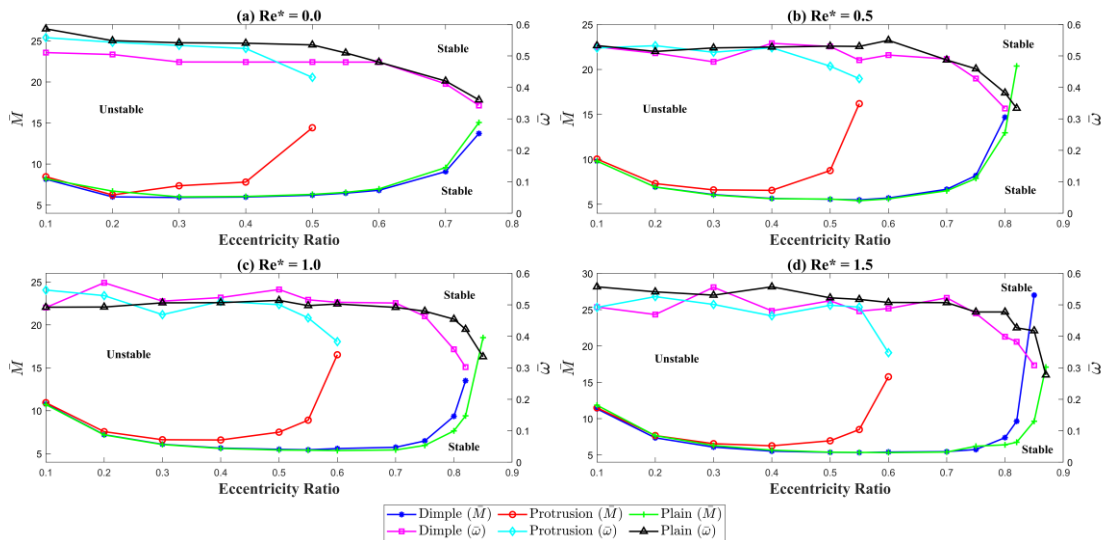


Fig. 5.17. Stability Map for $L / D = 1.0$, $S_p = 0.10$, $\delta = 0.15$, $\psi = 0.06$

From Fig. 5.17, it is observed that, for $S_p = 0.10$, a general trend is observed across all bearing types: the stability initially deteriorates as the eccentricity ratio increases, followed by a subsequent improvement at higher eccentricities. The protrusion texturing exhibits better stability compared to dimple textured and plain bearings, whereas the dimple and plain bearings exhibit similar stability regimes. The increase in modified Reynolds numbers results in better stability for $\varepsilon < 0.3$, whereas for $\varepsilon > 0.3$, the increase in inertia deteriorates the stability. A similar trend in the stability regime is observed for $S_p = 0.15$ and $S_p = 0.25$, as illustrated in Figs. 5.18 and 5.19, respectively. In these cases, protrusion textured bearings continue to demonstrate the highest stability margins, affirming the role of texture geometry in enhancing dynamic performance. The dimple textured and plain bearings again show comparable results, although slight improvements begin to appear in the case of dimple textured bearings, particularly under light to moderate loads.

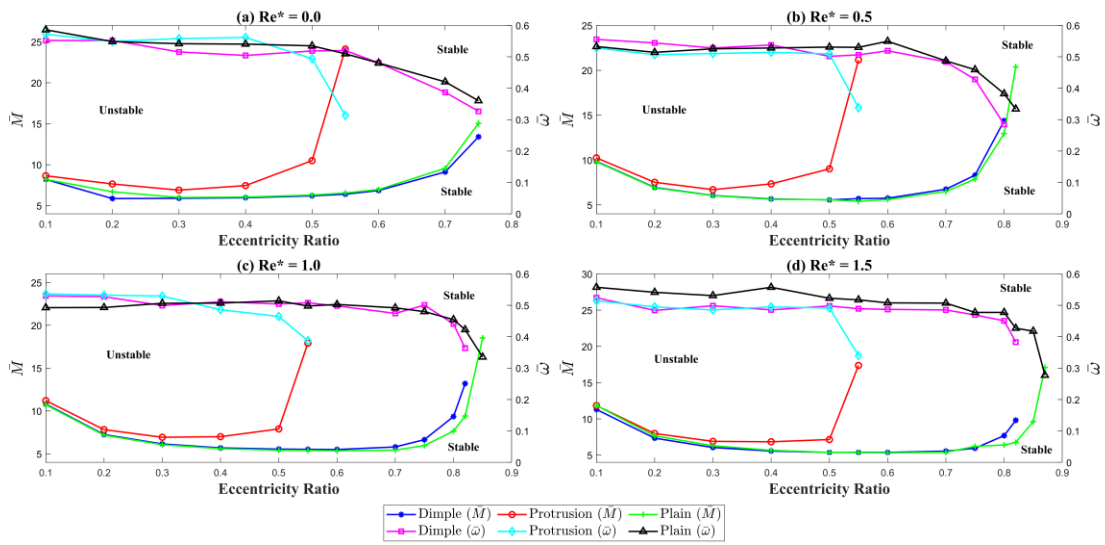


Fig. 5.18. Stability Map for $L/D = 1.0$, $S_p = 0.15$, $\delta = 0.15$, $\psi = 0.06$

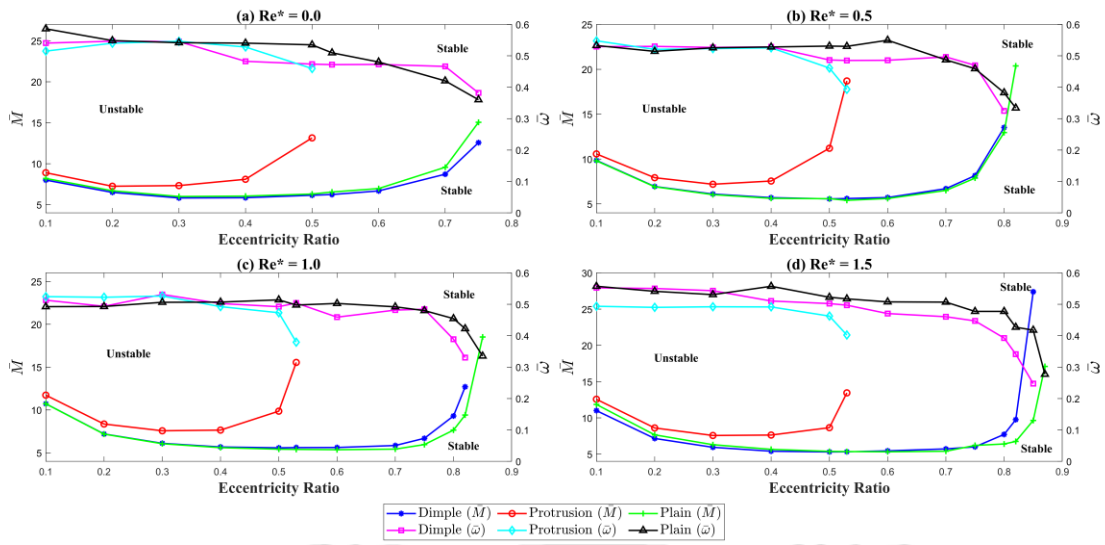


Fig. 5.19. Stability Map for $L/D = 1.0$, $S_p = 0.25$, $\delta = 0.15$, $\psi = 0.06$

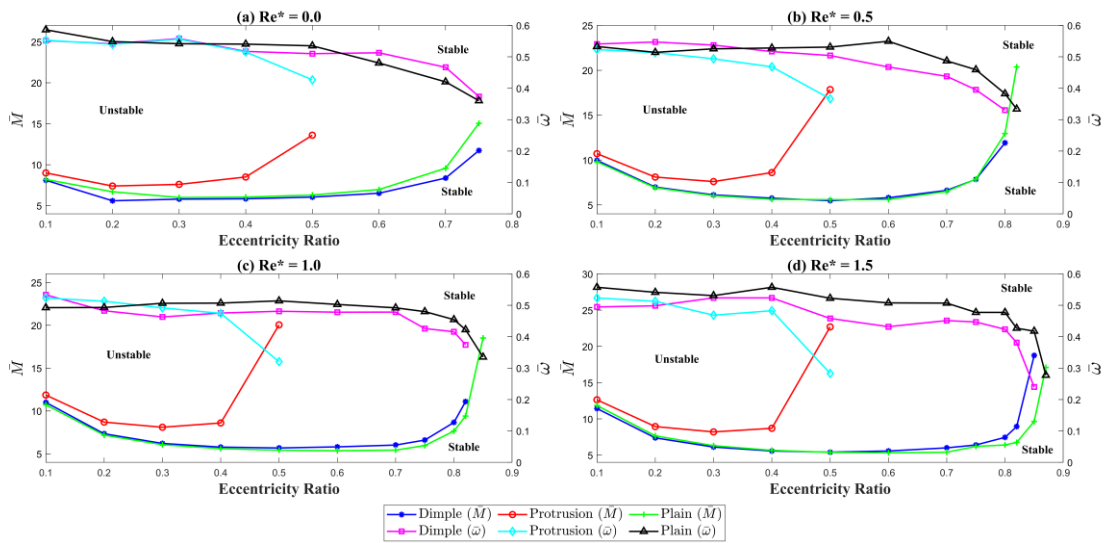


Fig. 5.20. Stability Map for $L/D = 1.0$, $S_p = 0.35$, $\delta = 0.15$, $\psi = 0.06$

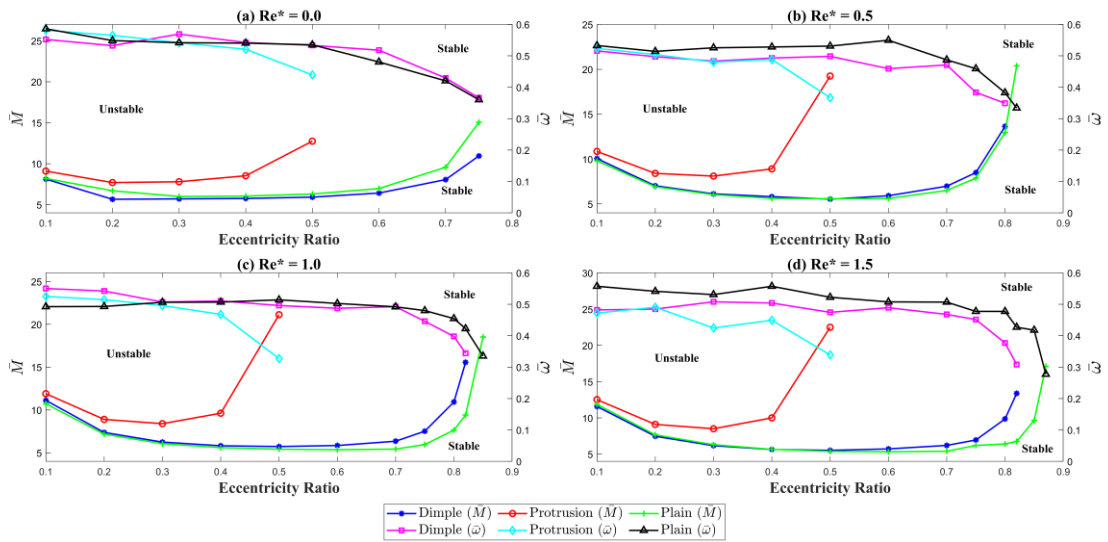


Fig. 5.21. Stability Map for $L/D = 1.0$, $S_p = 0.50$, $\delta = 0.15$, $\psi = 0.06$

Further, it is observed that the increase in inertia improves the stability of the protrusion and dimple textured bearings when dimple area density is increased to 0.35 and 0.50, as shown in Figs. 5.20 and 5.21, respectively. Notably, the protrusion-textured bearings continue to outperform both plain and dimpled bearings across all operating conditions. Further, dimple and plain bearings exhibit similar stability regimes at low modified Reynolds numbers, whereas at high modified Reynolds numbers and high eccentricity ratios, dimple texturing is found to be more stable than plain bearing. In

conclusion, the dimple area density (S_p) plays a vital role in shaping the dynamic stability characteristics of textured journal bearings. It is observed that the protrusion textures consistently deliver superior stability performance across a wide range of operating parameters. Thus, a careful selection of texturing configuration with appropriate dimple area density may improve the operational reliability of journal bearings.

5.4 Summary

This chapter presents a stability analysis of plain and textured journal bearings under the influence of lubricant inertia and employing Reynolds boundary conditions. Considering spherical protrusion and dimple textures, the various texturing parameters, viz. dimple aspect ratio, non-dimensional clearance and dimple aspect ratio, are varied and stability is assessed by estimating the critical mass parameters (a function of speed). This study confirms that protrusion texturing provides superior stability compared to dimple textured and plain journal bearings. Stability tends to decrease with increasing non-dimensional clearance. Although lubricant inertia enhances stability under lightly loaded conditions, it has an adverse effect under heavily loaded conditions, leading to reduced stability. Higher dimple aspect ratios and dimple area densities enhance stability, particularly for protrusion textures, with lubricant inertia playing a positive role when the eccentricity ratio is less than 0.3. These findings highlight the critical role of lubricant inertia in accurately predicting stability regimes and are especially relevant for optimizing high-speed machinery operating with low-viscosity oils. Future work may consider mass-conserving boundary conditions to further refine stability predictions.

The insights gained from the stability analysis, along with the findings from the preceding chapters, provide a foundation for the final conclusions. The next chapter consolidates these outcomes and presents the key inferences and comprehensive conclusions drawn from the overall work carried out in this thesis.

Chapter 6

Concluding Remarks

Contents

Concluding Remarks	119
6.1 Introduction	121
6.2 Inferences	122
6.3 Conclusions	125
6.4 Scope for Future Works	127





6.1 Introduction

This thesis deals with the analysis of textured journal bearing while considering the lubricant inertia effect and cavitation. It is noteworthy that although the effects of surface texturing and lubricant inertia have been extensively studied individually, their combined impact on the steady-state performance and stability of journal bearings remains largely unexplored. With the growing demand for high-speed machinery and the increasing use of unconventional lubricants such as water and liquid metals, it is essential to understand how these factors interact. Based on the literature review presented in chapter 1, the scope of the thesis has been drawn. The stability of journal bearings is influenced by the rotational speed. Estimation of critical mass parameter, which is a function of rotational speed, and corresponding whirl ratio provide a clear picture of stability of the bearing. However, these parameters have not been systematically analyzed for different texturing parameters under the influence of lubricant inertia. In view of this, a modified Reynolds equation has been derived incorporating the influence of lubricant inertia and texture parameters followed by the derivation of another novel modified Reynolds equation implementing the JFO boundary conditions. These formulations are presented in Chapter 2, along with the mathematical modelling of various texture geometries and the development of the numerical framework for stability analysis. The texturing configurations considered are protrusion and dimple texturing. The different texturing geometries considered here are spherical, cylindrical and square texture. Chapter 3 presents the steady-state performance characteristics of textured journal bearings under lubricant inertia effects using Reynolds boundary conditions. Chapter 4 extends this analysis by incorporating JFO boundary conditions. Finally, Chapter 5 presents the stability analysis of textured journal bearings, considering lubricant inertia and applying Reynolds boundary conditions.

6.2 Inferences

The inferences that are drawn from the results presented in this thesis are as follows:

- The progressive mesh densification method (PMD) is more efficient than fixed mesh method for evaluating the performance characteristics in the case of textured journal bearings. This aligns with the findings reported in earlier studies [72,73].
- The non-dimensional load-carrying capacity increases with increasing eccentricity ratio for both protrusion and dimple texturing. This trend is consistent for both Reynolds and JFO boundary conditions.
- Protrusion texturing yields higher load-carrying capacity compared to plain bearings, whereas dimple texturing yields lesser load-carrying capacity than plain bearing when Reynolds boundary conditions are considered. This trend is consistent with all the three texturing geometries, viz. spherical, cylindrical and square texture.
- When lubricant inertia effect is considered, in the case of Reynolds boundary conditions, the load-carrying capacity increases, for all the three texturing geometries, particularly at high eccentricity ratios and high modified Reynolds numbers.
- Among the texturing geometries, cylindrical protrusion texture shows significant improvement in load-carrying capacity at high modified Reynolds numbers, followed by spherical and square texture.
- The non-dimensional load-carrying capacity predicted using the JFO boundary conditions are consistently higher than those obtained using Reynolds boundary conditions across different bearing types.
- The combined influence of cavitation and inertia leads to a reduction in load-carrying capacity with increasing modified Reynolds numbers for all the cases of texturing, with protrusion texturing showing higher values of load-carrying capacity than dimple textured and plain bearings.
- Square protrusion texturing gives higher values of load-carrying capacity, followed by cylindrical and spherical texture, when JFO boundary conditions are used.

- The load-carrying capacity increases with increasing dimple aspect ratio in the case of protrusion texturing, whereas it decreases in the case of dimple texturing.
- Load-carrying capacity (LCC) initially decreases and then increases with increasing dimple area density for protrusion texturing, whereas for dimple texturing, the load-carrying capacity initially increases and then decreases with increasing dimple area density. The minimum LCC for protrusion and maximum LCC for dimple texturing are observed at dimple area density = 0.15.
- The non-dimensional flow coefficient increases with increasing eccentricity ratio for both protrusion and dimple texturing – a trend consistent with both Reynolds and JFO boundary conditions.
- Protruded texturing produces relatively better flow coefficient than dimple texturing; however, it is observed that both protruded and dimple texturing result in the reduction of flow coefficients compared to plain journal bearings for all eccentricity ratios and for all texture geometries.
- The flow coefficient increases with the increase in lubricant inertia effect particularly at high eccentricity ratios, irrespective of the texturing configuration and geometry.
- Among the texturing geometries, cylindrical protrusion texture shows maximum increment in flow coefficient at high modified Reynolds numbers, followed by spherical and square texture.
- The flow coefficients predicted using JFO boundary conditions are consistently lower than those estimated with Reynolds boundary conditions, with the exception of $\varepsilon = 0.1$.
- As lubricant inertia increases, the combined influence of inertial forces and cavitation results in a decreased flow coefficient for both protrusion and dimple texturing except $\varepsilon < 0.2$.
- Under JFO boundary conditions, square protrusions and square dimples yield the highest flow coefficients at low eccentricity ratios, whereas spherical protrusion and cylindrical dimple texturing yield higher flow coefficient at higher eccentricity ratios.
- The flow coefficient increases with increasing dimple aspect ratio in the case of protrusion texturing, whereas it decreases in the case of dimple texturing.

Concluding Remarks

- The flow coefficient initially increases and then decreases with increasing dimple area density for protrusion texturing, whereas for dimple texturing, the flow coefficient initially decreases and then increases with increasing dimple area density. The minimum and maximum flow coefficient for protrusion and dimple texturing are observed at dimple area density = 0.25 respectively.
- The friction variable exhibits a decreasing trend with increasing eccentricity ratio for both protrusion- and dimple-textured bearings, consistent under the application of both Reynolds and Jakobsson–Floberg–Olsson (JFO) boundary conditions.
- Under Reynolds boundary conditions, protrusion texturing results in a lower friction variable compared to both dimple-textured and plain bearings. This trend remains consistent across all three texture geometries—spherical, cylindrical, and square.
- The inclusion of lubricant inertia under Reynolds boundary conditions leads to a reduction in the friction variable for all three texturing geometries. This reduction becomes more significant at higher eccentricity ratios and increased modified Reynolds numbers.
- Among the various texturing geometries, the cylindrical protrusion texture demonstrates the most significant reduction in the friction variable at high modified Reynolds numbers, followed by spherical and square textures.
- In the absence of lubricant inertia, JFO boundary conditions consistently yield lower friction variables compared to Reynolds boundary conditions, regardless of the texturing configuration.
- The friction variable increases slightly for eccentricity ratios below 0.6. However, for $\varepsilon > 0.6$, plain, dimple-textured, and protrusion-textured bearings exhibit comparable frictional performance across all values of the modified Reynolds number. Consequently, under JFO boundary conditions, the influence of texturing configuration on the friction variable becomes negligible at higher eccentricity ratios.
- The friction variable decreases with increasing dimple aspect ratio for protrusion texturing. For dimple texturing, friction remains nearly constant at low modified Reynolds numbers, with spherical and cylindrical dimples performing better than

square ones. However, at higher Reynolds numbers, particularly at $Re^* = 1.5$, friction variable increases significantly, especially for cylindrical textures with higher dimple aspect ratio.

- For protrusion texturing, the friction variable initially increases and then decreases with increasing dimple area density, while for dimple texturing, it initially decreases and then increases. The maximum and minimum friction variable for protrusion and dimple texturing, respectively, occur at a dimple area density of 0.15.
- Protrusion texturing is found to be more stable than dimple texturing and plain bearings.
- Stability of textured and plain journal bearings deteriorates with the increase in non-dimensional clearance. The stability for lightly loaded bearings increases when the inertia effect of the lubricant is increased, whereas stability is adversely affected for moderately and heavily loaded bearings.
- Stability of protrusion textured journal bearings increases with the increase in the dimple aspect ratio. Lubricant inertia effect further enhances the stability when eccentricity ratio is less than or equal to 0.3.
- Stability is improved with increasing lubricant inertia at higher values of dimple area density, whereas increasing inertia deteriorates the stability at lower values of dimple area density for $\varepsilon > 0.3$.

6.3 Conclusions

The conclusions that are drawn from the results presented in this thesis are:

- Progressive mesh densification significantly enhances computational efficiency and therefore, should be adopted while estimating the performance characteristics of textured journal bearings.

Concluding Remarks

- JFO boundary conditions are recommended over Reynolds boundary conditions for more accurate predictions of steady state characteristics of textured journal bearings, as Reynolds conditions tend to underestimate load-carrying capacity and overestimate flow coefficient and friction variable.
- Protrusion texturing is recommended over dimple texturing and plain bearings, for enhancing journal bearing performance, with cylindrical protrusions offering better results under Reynolds boundary conditions and square protrusions performing the most effectively under JFO boundary conditions.
- It is essential to consider the lubricant inertia effect, especially in high-speed and low-viscosity lubricant applications, as it significantly enhances load-carrying capacity and flow coefficient while reducing the friction variable in heavily loaded bearings. The combined effect of lubricant inertia and cavitation, however, adversely affects the performance characteristics.
- The dynamic stability of journal bearing can be improved by the use of protrusion texturing. Bearing designers also can use appropriate dimple aspect ratio, dimple area density and non-dimensional clearance to improve stability of bearings. When higher dimple aspect ratio and higher area density improves the stability, on the contrary, higher non-dimensional clearance reduces the stability.
- One cannot ignore fluid inertia effect particularly for low viscosity and high-speed applications as lubricant inertia enhances the stability of lightly loaded bearings and the stability deteriorates for highly loaded bearings.

In summary, the improvement in the performance characteristics of the textured journal bearings, as observed in the present analysis, can be attributed to the combined hydrodynamic and tribological effects induced by the surface textures. The micro-textures, such as dimples and protrusions, act as localized pressure generation zones that enhance lubricant entrainment and storage within the textured zones. This leads to localized pressure build-up and contributes to an overall increase in the load-carrying capacity of the bearing.

Moreover, the presence of textures may facilitate film reformation in the cavitated regions, thereby ensuring a smoother pressure transition and reducing frictional losses. The modified pressure distribution due to texturing also improves the dynamic stiffness

and damping characteristics of the lubricant film, resulting in enhanced stability of the bearing system and suppression of fluid-film instabilities such as oil whirl.

6.4 Scope for Future Works

The outcomes of this study establish a foundation for further exploration in several key areas of textured journal bearing research, as outlined below.

- Though attempted, Non-linear transient analysis of textured journal bearings, incorporating lubricant inertia effects under JFO boundary conditions could not produce any result due to convergence issues. This issue may be taken up, on priority, in future work to better understand transient cavitation behaviour under varying operational conditions. Detailed study of the half-whirl frequency can also be taken up as a future work.
- Incorporate thermal effects and temperature-dependent viscosity into the current isothermal model to provide a more accurate evaluation of bearing performance under realistic thermal loading conditions.
- Future studies can focus on incorporating bionic surface textures inspired by natural structures, such as the ribbed patterns of shark skin or the microstructures on lotus leaves, to improve journal bearing performance. These biologically inspired textures hold potential for enhancing load support, reducing friction, and stabilizing lubricant film behaviour under a wide range of operating conditions.
- The present study has considered textures arranged in regular, aligned patterns. Future investigations may focus on the effect of zig-zag arrangement of textures, which have been reported in the literature to provide improved hydrodynamic performance and enhanced load-carrying capacity.
- Future work may focus on integrating turbulence and slip flow models into the study of textured journal bearings with lubricant inertia effects, under JFO cavitation theory, to more accurately predict the complex flow phenomena occurring in high-speed applications.
- Future work may focus on the experimental validation of the numerical results to confirm the accuracy and reliability of the simulation outcomes under real-world conditions.



References

- [1] Kakoty, S. K. (1999). Effect of Fluid Inertia on Stability of Fluid Film Bearings (Doctoral dissertation, IIT, Kharagpur).
- [2] Vishnoi, M., Kumar, P. and Murtaza, Q., 2021. Surface texturing techniques to enhance tribological performance: A review. *Surfaces and Interfaces*, 27, p.101463.
- [3] Bulut, D., Bader, N. and Poll, G., 2021. Cavitation and film formation in hydrodynamically lubricated parallel sliders. *Tribology International*, 162, p.107113.
- [4] Xu, W., Zhao, S., Xu, Y. and Li, K., 2021. Reynolds model versus JFO theory in steadily loaded journal bearings. *Lubricants*, 9(11), p.111.
- [5] Elrod, H.G., 1981. A cavitation algorithm. *Journal of lubrication Technology*, 103(3), pp.350-354.
- [6] Mitchell, J.S. and Saunders, H., 1982. An introduction to machinery analysis and monitoring.
- [7] Beauchamp, T., 1883. First report on friction experiments. *Proc. Inst. Mech. Engrs*, 34(1), pp.632-659.
- [8] Reynolds, O., 1885. On the theory of lubrication and its application to Mr. Beauchamp Tower's experiments, including an experimental determination of the viscosity of olive oil. *Phil. Trans. Roy. Soc.*, 1, p.157.
- [9] Kingsbury, A., 1931. On problems in the theory of fluid-film lubrication, with an experimental method of solution. *Transactions of the American Society of Mechanical Engineers*, 53(2), pp.59-70.
- [10] Muskat, M.F.M.W., Morgan, F. and Meres, M.W., 1940. Studies in lubrication. VII. The lubrication of plane sliders of finite width. *Journal of Applied Physics*, 11(3), pp.208-219.

- [11] Christopherson, D.G., 1941. A new mathematical method for the solution of film lubrication problems. Proceedings of the Institution of Mechanical Engineers, 146(1), pp.126-135.
- [12] Swift, H.W., 1932, January. The stability of lubricating films in journal bearings (includes appendix). In Minutes of the Proceedings of the Institution of Civil Engineers (Vol. 233, No. 1932, pp. 267-288). Thomas Telford-ICE Virtual Library.
- [13] Stieber, W. and Schwimmlager, D., 1933. Verein Deutscher Ingenieure.
- [14] DuBois, G.B. and Ocvirk, F.W., 1953. Analytical derivation and experimental evaluation of short-bearing approximation for full journal bearing (No. NACA-TR-1157).
- [15] Ocvirk, F.W., 1952. Short-bearing approximation for full journal bearings (No. NACA-TN-2808).
- [16] Raimondi, A.A. and Boyd, J., 1958. A solution for the finite journal bearing and its application to analysis and design: I. ASLE Transactions, 1(1), pp.159-174.
- [17] Raimondi, A.A. and Boyd, J., 1958. A solution for the finite journal bearing and its application to analysis and design: II. ASLE Transactions, 1(1), pp.175-193.
- [18] Raimondi, A.A. and Boyd, J., 1958. A solution for the finite journal bearing and its application to analysis and design: III. ASLE Transactions, 1(1), pp.194-209.
- [19] Pinkus, O. and Bupara, S.S., 1979. Analysis of misaligned grooved journal bearings. Journal of Lubrication Technology, 101(4), pp.503-509.
- [20] El-Gamal, H.A., 1995. Analysis of the steady state performance of a wedge-shaped hydrodynamic journal bearing. Wear, 184(2), pp.111-117.
- [21] Chatterton, S., Dang, P.V., Pennacchi, P., De Luca, A. and Flumian, F., 2017. Experimental evidence of a two-axial groove hydrodynamic journal bearing under severe operation conditions. Tribology International, 109, pp.416-427.

- [22] Zhang, X., Yin, Z., Gao, G. and Li, Z., 2015. Determination of stiffness coefficients of hydrodynamic water-lubricated plain journal bearings. *Tribology International*, 85, pp.37-47.
- [23] Cui, S., Zhang, C., Fillon, M. and Gu, L., 2020. Optimization performance of plain journal bearings with partial wall slip. *Tribology International*, 145, p.106137.
- [24] Chowdhury, M.A., Mia, M.S., Kchaou, M., Shuvho, M.B.A. and Debanath, U.K., 2020. Friction coefficient and performance evaluation of plain journal bearing using SAE 5W-30 engine oil. *Proceedings of the Institution of Mechanical Engineers, Part J: Journal of Engineering Tribology*, 234(8), pp.1222-1232.
- [25] Milčić, D., Alsammaraie, A., Madić, M., Krstić, V. and Milčić, M., 2021. Predictions of friction coefficient in hydrodynamic journal bearing using artificial neural networks. *Strojniški vestnik-Journal of Mechanical Engineering*, 67(9), pp.411-420.
- [26] Shaltout, M.L. and Hegazi, H.A., 2021. Multi-objective design optimization of hydrodynamic journal bearings using a hybrid approach. *Industrial Lubrication and Tribology*, 73(7), pp.1052-1060.
- [27] Li, J., Chen, R., Cao, H. and Tian, Z., 2020. Numerical study of nonlinear stability boundaries for orifice-compensated hole-entry hybrid journal bearings. *Proceedings of the Institution of Mechanical Engineers, Part J: Journal of Engineering Tribology*, 234(12), pp.1867-1880.
- [28] Navthar, R.R. and Halegowda, N.V., 2010. Stability analysis of hydrodynamic journal bearing using stiffness coefficients. *International Journal of Engineering Science and Technology*, 2(2), pp.87-93.
- [29] Raghunandana, K. and Majumdar, B.C., 1999. Stability of journal bearing systems using non-Newtonian lubricants: A non-linear transient analysis. *Tribology international*, 32(4), pp.179-184.

- [30] Das, S., Guha, S.K. and Chattopadhyay, A.K., 2005. Linear stability analysis of hydrodynamic journal bearings under micropolar lubrication. *Tribology International*, 38(5), pp.500-507.
- [31] Papadopoulos, C.A., Nikolakopoulos, P.G. and Gounaris, G.D., 2008. Identification of clearances and stability analysis for a rotor-journal bearing system. *Mechanism and Machine Theory*, 43(4), pp.411-426.
- [32] Jang, G.H. and Yoon, J.W., 2003. Stability analysis of a hydrodynamic journal bearing with rotating herringbone grooves. *J. Trib.*, 125(2), pp.291-300.
- [33] Dinakaran, S. and Ramesh, S., 2015. Stability analysis of journal bearing: Dynamic characteristics. *Research Journal of Applied Sciences, Engineering and Technology*, 9(1), pp.47-52.
- [34] Constantinescu, V.N., 1970. On the influence of inertia forces in turbulent and laminar self-acting films. *Journal of Lubrication Technology*, 92(3), pp.473-480.
- [35] Reinhardt, E. and Lund, J.W., 1975. The influence of fluid inertia on the dynamic properties of journal bearings. *Journal of Lubrication Technology*, 104(2), pp.159-165.
- [36] Constantinescu, V.N. and Galetuse, S., 1982. Operating characteristics of journal bearings in turbulent inertial flow. *Journal of Lubrication Technology*, 104(2), pp.173-179.
- [37] Malvano, R. and Vatta, F., 1983. The influence of fluid inertia in steady laminar lubrication. *Journal of Lubrication Technology*, 105(1), pp.77-83.
- [38] Chen, C.H., Cha, O. and Chen, K., 1989. The influence of fluid inertia on the operating characteristics of finite journal bearings. *Wear*, 131(2), pp.229-240.
- [39] Nataraj, C., Ashrafiun, H. and Arakere, N.K., 1994. Effect of fluid inertia on journal bearing parameters. *Tribology transactions*, 37(4), pp.784-792.

- [40] Kakoty, S.K. and Majumdar, B.C., 1999. Effect of fluid inertia on stability of flexibly supported oil journal bearings: linear perturbation analysis. *Tribology International*, 32(4), pp.217-228.
- [41] Kakoty, S.K. and Majumdar, B.C., 2002. Effect of fluid film inertia on stability of flexibly supported oil journal bearings: a non-linear transient analysis. *Tribology transactions*, 45(2), pp.253-257.
- [42] Kakoty, S.K. and Majumdar, B.C., 2000. Effect of fluid inertia on stability of oil journal bearings. *Journal of Tribology*, 122(4), pp.741-745.
- [43] Kakoty, S.K. and Majumdar, B.C., 2000. Effect of fluid inertia on the dynamic coefficients and stability of journal bearings. *Proceedings of the Institution of Mechanical Engineers, Part J: Journal of Engineering Tribology*, 214(3), pp.229-240.
- [44] Nassab, G.S., 2005. Inertia effect on the thermohydrodynamic characteristics of journal bearings. *Proceedings of the Institution of Mechanical Engineers, Part J: Journal of Engineering Tribology*, 219(6), pp.459-467.
- [45] Javorova, J.G., Alexandrov, V., Stanulov, K. and Tzvetkof, T., 2005, January. *Journal Bearings Stability With Consideration of Fluid Inertia*. In *World Tribology Congress (Vol. 42010, pp. 583-584)*.
- [46] Lin, J.R., Chu, L.M., Liang, L.J. and Hung, C.R., 2008. Combined effects of fluid inertia and non-Newtonian couple stresses on the squeeze film characteristics of a long partial journal bearing. *Proceedings of the Institution of Mechanical Engineers, Part J: Journal of Engineering Tribology*, 222(7), pp.985-993.
- [47] Dousti, S., Allaire, P., Dimond, T. and Cao, J., 2016. An extended Reynold equation applicable to high reduced Reynolds number operation of journal bearings. *Tribology International*, 102, pp.182-197.
- [48] Javorova, J. and Alexandrov, V., 2017, February. Effects of fluid inertia and bearing flexibility on the performance of finite length journal bearing. In *IOP Conference Series: Materials Science and Engineering (Vol. 174, No. 1, p. 012039)*. IOP Publishing.

- [49] JAVOROVA, J., 2021. Review on hydrodynamic lubrication of journal bearings with fluid inertia effects. *Journal of the Balkan Tribological Association*, 27(6).
- [50] Ghosh, K.C., Mazumder, S.K. and Majumdar, M.C., 2017. Steady state performance characteristics of isoviscous finite flexible oil journal bearings including fluid inertia effect. *continuity*, 15(1), p.12.
- [51] Xu, B., Guo, H., Wu, X., He, Y., Wang, X. and Bai, J., 2022. Static and dynamic characteristics and stability analysis of high-speed water-lubricated hydrodynamic journal bearings. *Proceedings of the Institution of Mechanical Engineers, Part J: Journal of Engineering Tribology*, 236(4), pp.701-720.
- [52] Ozen, S. and Azeloglu, C.O., 2025. An Inertia Correction Scheme for Hydrodynamic Lubrication Problems. *International Journal for Numerical Methods in Fluids*, 97(5), pp.830-839.
- [53] Chen, X., Gan, X. and Ren, G., 2022. Effects of journal static eccentricity on dynamic responses of a rotor system under base motions using FDM inertia model. *Journal of Sound and Vibration*, 519, p.116591.
- [54] Kushare, P.B. and Sharma, S.C., 2014. Nonlinear transient stability study of two lobe symmetric hole entry worn hybrid journal bearing operating with non-Newtonian lubricant. *Tribology International*, 69, pp.84-101.
- [55] Fan, L., Inoue, T., Heya, A. and Watanabe, Y., 2024. Predicting stability of synchronous nonlinear vibration in vertical rotating shaft system with journal bearing. *Journal of Sound and Vibration*, 572, p.118191.
- [56] Hamilton, D.B., Walowit, J.A. and Allen, C.M., 1966. A theory of lubrication by microirregularities. *Journal of basic engineering*, 88(1), pp.177-185.
- [57] Zhang, J. and Meng, Y., 2012. Direct observation of cavitation phenomenon and hydrodynamic lubrication analysis of textured surfaces. *Tribology Letters*, 46(2), pp.147-158.
- [58] Jeng, Y.R., 1990. Experimental study of the effects of surface roughness on friction. *Tribology Transactions*, 33(3), pp.402-410.

- [59] Hargreaver, D., 1991. Surface waviness effects on the load carrying capacity of rectangular slide bearings. *Wear*, 145(1), pp.137-151.
- [60] Wakuda, M., Yamauchi, Y., Kanzaki, S. and Yasuda, Y., 2003. Effect of surface texturing on friction reduction between ceramic and steel materials under lubricated sliding contact. *Wear*, 254(3-4), pp.356-363.
- [61] Tala-Ighil, N., Maspeyrot, P., Fillon, M. and Bounif, A., 2007. Effects of surface texture on journal-bearing characteristics under steady-state operating conditions. *Proceedings of the Institution of Mechanical Engineers, Part J: Journal of Engineering Tribology*, 221(6), pp.623-633.
- [62] Siripuram, R.B. and Stephens, L.S., 2004. Effect of deterministic asperity geometry on hydrodynamic lubrication. *Journal of Tribology*, 126(3), pp.527-534.
- [63] Rahmani, R., Shirvani, A. and Shirvani, H., 2007. Optimization of partially textured parallel thrust bearings with square-shaped micro-dimples. *Tribology transactions*, 50(3), pp.401-406.
- [64] Rajoub, M.B., El-Gamal, H.A. and Attia, E.M., 2020. The performance of a plain journal textured bearing. *Int. J. Eng. Res. Technol.(IJERT)*, 12, pp.657-662.
- [65] Tala-Ighil, N., Fillon, M. and Maspeyrot, P., 2011. Effect of textured area on the performances of a hydrodynamic journal bearing. *Tribology international*, 44(3), pp.211-219.
- [66] Sharma, S., Jamwal, G. and Awasthi, R.K., 2019. Numerical study on steady state performance enhancement of partial textured hydrodynamic journal bearing. *Industrial Lubrication and Tribology*, 71(9), pp.1055-1063.
- [67] Brizmer, V. and Kligerman, Y., 2012. A laser surface textured journal bearing. *Journal of Tribology*, 134(3), pp.031702.
- [68] Rao, T.V.V.L.N., Rani, A.M.A., Nagarajan, T. and Hashim, F.M., 2012. Analysis of slider and journal bearing using partially textured slip surface. *Tribology International*, 56, pp.121-128.

- [69] Gupta, K.K., Kumar, R., Kumar, H. and Sharma, M., 2013. Study on effect of surface texture on the performance of hydrodynamic journal bearing. *International Journal of Engineering and Advanced Technology*, 3(1), pp.49-54.
- [70] Li, J. and Wang, X., 2013. Numerical simulation of the influence of the bulges around laser surface textures on the tribological performance. *Tribology Transactions*, 56(6), pp.1011-1018.
- [71] Filgueira Filho, I.C.M., Bottene, A.C., Silva, E.J.D. and Nicoletti, R., 2021. Static behavior of plain journal bearings with textured journal-experimental analysis. *Tribology International*, 159, p.106970.
- [72] Syed, N.R. and Kakoty, S.K., 2022. Computational efficiency improvement of dimple textured hydrodynamic journal bearing using progressive mesh densification method. *Journal of Tribology*, 144(3), p.031801.
- [73] Syed, N.R. and Kakoty, S.K., 2025. Texture Parameters' Impact on Computational Efficiencies of Multigrid and Progressive Mesh Densification Methods for Solving Textured Journal Bearing Problems. *Journal of Tribology*, 147(8).
- [74] Syed, I. and Sarangi, M., 2014. Hydrodynamic lubrication with deterministic micro textures considering fluid inertia effect. *Tribology International*, 69, pp.30-38.
- [75] Syed, I. and Sarangi, M., 2020. Influence of surface textures on the hydrodynamic performance of parallel sliding contacts in turbulent regime. *Journal of the Brazilian Society of Mechanical Sciences and Engineering*, 42(1), p.21.
- [76] Singh, N. and Awasthi, R.K., 2021. Influence of texture geometries on the performance parameters of hydrodynamic journal bearing. *Proceedings of the Institution of Mechanical Engineers, Part J: Journal of Engineering Tribology*, 235(10), pp.2056-2072.
- [77] Panigrahi, D.K. and Sarangi, M., 2020. Tribological performance of positive deterministic textured surfaces in parallel sliding lubricated contacts: effect

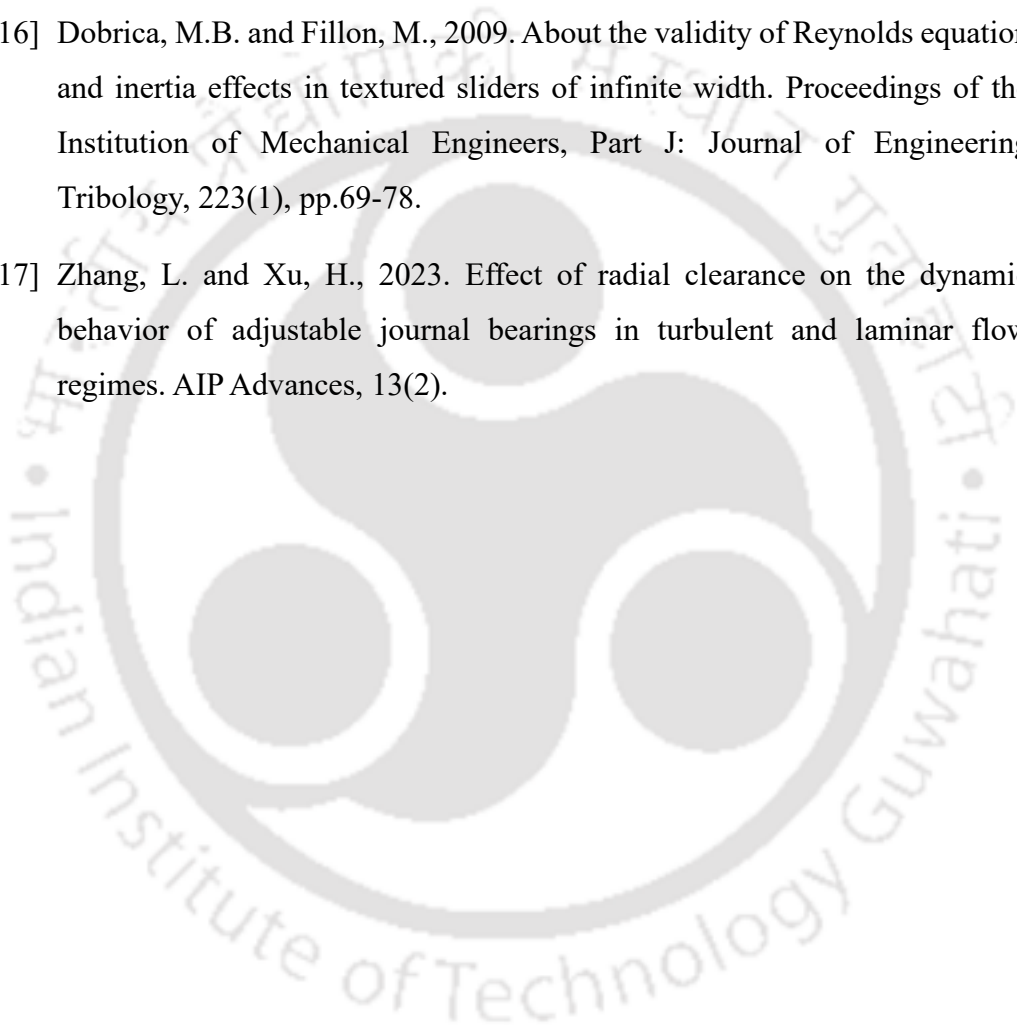
- of texture size and height. Proceedings of the Institution of Mechanical Engineers, Part J: Journal of Engineering Tribology, 234(12), pp.1908-1925.
- [78] Syed, I., Veeraraju, V., and Sarangi, M., 2012. Experimental study on micro-textured thrust pad bearing. *Machines and Mechanisms*, pp. 171–179.
- [79] Tala-Ighil, N., Maspeyrot, P., Fillon, M. and Bounif, A., 2007, November. Hydrodynamic effects of texture geometries on journal bearing surfaces. In *International Conference on Tribology*, Bucharest, Romania, Nov (pp. 8-10).
- [80] Ismail, S. and Sarangi, M., 2013, December. Influence of texture orientation on the hydrodynamic lubrication. In *1st International and 16th national conference on machines and mechanisms IIT Roorkee, India*, Dec (pp. 18-20).
- [81] Syed, I. and Sarangi, M., 2018. Combined effects of fluid–solid interfacial slip and fluid inertia on the hydrodynamic performance of square shape textured parallel sliding contacts. *Journal of the Brazilian Society of Mechanical Sciences and Engineering*, 40(6), p.314.
- [82] Cupillard, S., Glavatskih, S. and Cervantes, M.J., 2008. Computational fluid dynamics analysis of a journal bearing with surface texturing. *Proceedings of the Institution of Mechanical Engineers, Part J: Journal of Engineering Tribology*, 222(2), pp.97-107.
- [83] Cupillard, S., Glavatskih, S. and Cervantes, M.J., 2010. Inertia effects in textured hydrodynamic contacts. *Proceedings of the Institution of Mechanical Engineers, Part J: Journal of Engineering Tribology*, 224(8), pp.751-756.
- [84] Sinanoğlu, C., Nair, F. and Karamış, M.B., 2005. Effects of shaft surface texture on journal bearing pressure distribution. *Journal of materials processing technology*, 168(2), pp.344-353.
- [85] Yamada, H., Kaneko, S. and Taura, H., 2015, May. Effect of square-dimple size on dynamic characteristics of textured journal bearings. In *Proceedings of the 9th IFToMM International Conference on Rotor Dynamics* (pp. 883-893). Cham: Springer International Publishing.

- [86] Yamada, H., Taura, H. and Kaneko, S., 2018. Numerical and experimental analyses of the dynamic characteristics of journal bearings with square dimples. *Journal of Tribology*, 140(1), p.011703.
- [87] Taura, H., 2018, August. Effect of texture region on the static and dynamic characteristic of partially textured journal bearings. In *International Conference on Rotor Dynamics* (pp. 422-436). Cham: Springer International Publishing.
- [88] Ganji, T.S., Kakoty, S.K. and Pandey, R.K., 2014. Dynamic characteristic and stability of cylindrical textured journal bearing. *International Journal of Recent Advances in Mechanical Engineering*, 3(2), pp.1-14.
- [89] Smolík, L., Rendl, J., Omasta, M., Byrtus, M., Šperka, P., Polach, P., Hartl, M. and Hajžman, M., 2023. Comprehensive analysis of fluid-film instability in journal bearings with mechanically indented textures. *Journal of Sound and Vibration*, 546, p.117454.
- [90] Jang, J.Y., Khonsari, M.M., Soto, C. and Livingstone, G., 2024. Effect of varnish on the performance and stability of journal bearings. *Tribology International*, 198, p.109897.
- [91] Wang, K., Ji, X., Wang, X., Liu, Y., Zhu, K., Huang, H., Pang, L. and Yang, L., 2024. Vibration suppression and transient tribo-dynamic stability for adjustable offset-elliptical journal bearings under time-varying load and bi-directional misalignment. *Tribology International*, 200, p.110105.
- [92] Gropper, D., Wang, L. and Harvey, T.J., 2016. Hydrodynamic lubrication of textured surfaces: A review of modeling techniques and key findings. *Tribology international*, 94, pp.509-529.
- [93] Sharma, S., Jamwal, G. and Awasthi, R.K., 2020. Dynamic and stability performance improvement of the hydrodynamic bearing by using triangular-shaped textures. *Proceedings of the Institution of Mechanical Engineers, Part J: Journal of Engineering Tribology*, 234(9), pp.1436-1451.

- [94] Byotra, D. and Sharma, S., 2024. Dynamic and stability analysis of crescent geometry-possessing textured journal bearing using nanolubricant. *Industrial Lubrication and Tribology*, 76(6), pp.788-803.
- [95] Byotra, D. and Sharma, S., 2022. Performance analysis of textured journal bearing operating with and without nanoparticles in the lubricant. *Industrial Lubrication and Tribology*, 74(9), pp.1028-1039.
- [96] Jamwal, G., Sharma, S. and Awasthi, R.K., 2020. The dynamic performance analysis of chevron shape textured hydrodynamic bearings. *Industrial Lubrication and Tribology*, 72(1), pp.1-8.
- [97] Fesanghary, M. and Khonsari, M.M., 2011. A modification of the switch function in the Elrod cavitation algorithm. *Journal of Tribology*, 133(2), pp.024501.
- [98] Vijayaraghavan, D. and Keith Jr, T.G., 1989. Development and evaluation of a cavitation algorithm. *Tribology Transactions*, 32(2), pp.225-233.
- [99] Qiu, Y. and Khonsari, M.M., 2009. On the prediction of cavitation in dimples using a mass-conservative algorithm. *Journal of Tribology*, 131(4), p.1.
- [100] Manser, B., Belaidi, I., Hamrani, A., Khelladi, S. and Bakir, F., 2020. Texture shape effects on hydrodynamic journal bearing performances using mass-conserving numerical approach. *Tribology-Materials, Surfaces & Interfaces*, 14(1), pp.33-50.
- [101] Pattnayak, M.R., Pandey, R.K. and Dutt, J.K., 2022. Performance improvement of an oil-lubricated journal bearing using bionic-textures fused micro-pockets. *Journal of Tribology*, 144(4), p.041804.
- [102] Syed, N.R. and Kakoty, S.K., 2022. Influence of spherical protruded and dimple texture on the journal bearing performance: A comparative theoretical analysis implementing JFO boundary conditions. *Industrial Lubrication and Tribology*, 74(7), pp.788-795.
- [103] Ausas, R., Ragot, P., Leiva, J., Jai, M., Bayada, G. and Buscaglia, G.C., 2007. The impact of the cavitation model in the analysis of microtextured lubricated journal bearings. *Journal of Tribology*, 129(4), pp.868-875.

- [104] Usman, A. and Park, C.W., 2018. Numerical optimization of surface texture for improved tribological performance of journal bearing at varying operating conditions. *Industrial Lubrication and Tribology*, 70(9), pp.1608-1618.
- [105] Jamari, J., Muchammad, M., Hilmy, F. and Tauviqirrahman, M., 2019. Effect of inertia on the cavitation phenomena of hydrodynamic textured bearings considering slip. *Journal of the Brazilian Society of Mechanical Sciences and Engineering*, 41(9), p.387.
- [106] Tauviqirrahman M., Jamari M., J., and Yohana E., 2020. Inertia Effect on the Cavitation Phenomena of Textured Bearing. Scitepress, pp.29-35.
- [107] Panigrahi, D.K. and Sarangi, M., 2015. Effect of cavitation in lubricated sliding textured surfaces. In 2nd International and 17th National Conference on Machines and Mechanisms (Vol. 30).
- [108] Sawicki, J.T. and Rao, T.V.V.L.N., 2004. Cavitation effects on the stability of a submerged journal bearing. *International Journal of Rotating Machinery*, 10(3), pp.227-232.
- [109] Guo, B., 2017. Optimal surface texture design of journal bearing with axial grooves. *International Journal of Heat and Technology*, 35(2), pp.267-272.
- [110] Dobrica, M.B., Fillon, M., Pascovici, M.D. and Cicone, T., 2010. Optimizing surface texture for hydrodynamic lubricated contacts using a mass-conserving numerical approach. *Proceedings of the Institution of Mechanical Engineers, Part J: Journal of Engineering Tribology*, 224(8), pp.737-750.
- [111] Pu, W., Wang, J. and Zhu, D., 2016. Progressive mesh densification method for numerical solution of mixed elastohydrodynamic lubrication. *Journal of Tribology*, 138(2), p.021502.
- [112] Majumdar, B.C., 2008. *Introduction to tribology of bearings*. S. Chand Publishing.
- [113] Kumar, R., Azam, M.S., Ghosh, S.K. and Khan, H., 2019. Thermo-elastohydrodynamic lubrication simulation of the Rayleigh step bearing

- using the progressive mesh densification method. *Simulation*, 95(5), pp.395-410.
- [114] Yamada, H., Taura, H. and Kaneko, S., 2017. Static characteristics of journal bearings with square dimples. *Journal of Tribology*, 139(5), p.051703.
- [115] Etsion I., 2005. State of the art in laser surface texturing. *Journal of Tribology*, 127, pp.248-53.
- [116] Dobrica, M.B. and Fillon, M., 2009. About the validity of Reynolds equation and inertia effects in textured sliders of infinite width. *Proceedings of the Institution of Mechanical Engineers, Part J: Journal of Engineering Tribology*, 223(1), pp.69-78.
- [117] Zhang, L. and Xu, H., 2023. Effect of radial clearance on the dynamic behavior of adjustable journal bearings in turbulent and laminar flow regimes. *AIP Advances*, 13(2).





List of Publications

International Journals

1. Das D, Kakoty SK. Effect of lubricant inertia on steady-state characteristics of textured hydrodynamic journal bearing. *Ind Lubr Tribol* 2023; 75:333–42. <https://doi.org/10.1108/ILT-09-2022-0289>.
2. Das D, Kakoty SK. Effect of lubricant inertia on textured journal bearing implementing mass conserving (JFO) boundary conditions. *Ind Lubr Tribol* 2024; 76:1186–96. <https://doi.org/10.1108/ILT-07-2024-0276>.
3. Das D, Kakoty SK. Effect of fluid inertia and texturing parameters on the stability of textured journal bearings: A nonlinear time transient analysis. *Physics of Fluid* 2025; 37:087174. <https://doi.org/10.1063/5.0284474>.

International Conferences

1. Das D, Kakoty SK. Influence of Texture Geometry in the Steady-State Performance of Dimple-Textured Journal Bearings Under the Effect of Lubricant Inertia. 6th International and 21st National Conference on Machines and Mechanisms, 9-11 December, 2023, NIT Raipur. https://doi.org/10.1007/978-981-97-5423-6_29.
2. Das D, Kakoty SK. Influence of Texture Geometry in the Steady State Performance of Protrusion Textured Journal Bearings under the Effect of Lubricant Inertia. VETOMAC XVIII, 18-20 December, 2023, IIT Roorkee.
3. Das D, Kakoty SK. Influence of Texture Geometry on the Performance of Textured Journal Bearing Considering Fluid Inertia Effect and Cavitation. Research and Industrial Conclave, 9-11 August, 2024, IIT Guwahati.
4. Das D, Kakoty SK. Effect of Texturing Parameter and Fluid Inertia on the Steady-State Performance of Journal Bearing Considering Mass-Conserving Boundary Conditions. 11th International Conference on Mechanical, Automotive and Materials Engineering, 18-20 December, 2024, Thailand.



Curriculum vitae

Born and brought up in Guwahati, a city in Assam, in the North-Eastern part of India, Mr. Debajit Das is the eldest of two children of Mr. Jitendra Nath Das and Mrs. Urmila Das. After schooling in Guwahati, he graduated in Mechanical Engineering from Girijananda Chowdhury Institute of Management and Technology (then affiliated to Gauhati University), Guwahati, in 2014. He worked as a Sr. Customer service associate in Amazon Development centre, Hyderabad for more than a year. He completed his Master of Engineering degree from Assam Engineering College, Guwahati in 2019. Later, he joined the Department of Mechanical Engineering of the Indian Institute of Technology Guwahati as a Research Scholar in January, 2020 and worked under the supervision of Prof. Sashindra Kr. Kakoty. His research interests are hydrodynamic lubrication, static and dynamic analysis of textured journal bearing, cavitation in journal bearing, and inertia effect of lubricant.